Ultrafast Dynamics of Condensed Matter
University of Potsdam

Master Thesis

Grüneisen model of ultrafast Stress in magnetic Materials: Evidence from ultrafast X-ray diffraction experiment

First Assessor:
Prof. Dr. Matias Bargheer
University of Potsdam

Author:
Maximilian Mattern

Second Assessor:
Prof. Dr. Markus Gühr
University of Potsdam

Faculty of Mathematics and Science
Institute of Physics and Astronomy
November 5, 2020

Abstract

In this thesis I present the strain response of laser-excited strontium ruthenate and dysprosium measured by ultrafast X-ray diffraction as function of the magnetic order. Below the magnetic order temperature, the excitation of the magnetic degrees of freedom provides an additional contractive stress in both materials that reduces the ultrafast expansion and leads to unconventional strain pulses in dysprosium. The modelling of the picosecond strain response reveals the spatio-temporal stress as superposition of contributions from phonons and magnetic excitations. I apply the thermodynamic concept of a macroscopic Grüneisen parameter to individually describe the stress contributions of the subsystems. The subsystem-specific Grüneisen constants linearly relate the deposited energy density to a stress contribution that inherits its time-dependence from the excitation of the subsystem via its coupling to the other subsystems.

The most prominent property of the magnetic stress next to its contractive nature is its saturability due to a finite integral of the magnetic heat capacity that corresponds to a full demagnetisation of the material. The temperature- and fluence-dependent saturation of the magnetic stress results in a temperature- and fluence-dependent total stress that drives the strain response of the sample structure. The total laser-induced stress in strontium ruthenate exemplifies the changing temperature and fluence dependence due to the saturation of the magnetic stress, for the case of ultrafast equilibration between electronic, phononic and magnetic degrees of freedom. In the high fluence regime the magnetic stress depends on the temperature-dependent integral of the remaining, total magnetic heat capacity, whereas the magnetic stress is proportional to the magnetic heat capacity in the low fluence regime.

In the inhomogeneously excited dysprosium layer the saturation of the magnetic stress results in a spatially-dependent sign of the total stress that changes with time due to the long-lasting non-equilibrium between phonons and magnetic excitations. At the fully demagnetised top side of the layer the tensile phonon stress dominates and drives a bipolar strain wave. At the bottom of the magnetic layer the non-saturated magnetic stress dominates and the contraction drives an expansion wave into the substrate. These two contributions superimpose to the unconventional strain wave shape that is an asymmetric bipolar strain wave preceded by an expansion detected in a buried non-excited detection layer. The spatial extension of the fully demagnetised part of the transducer is fluence-dependent. A double-pulse excitation scheme with a varying fluence of the first excitation but a constant fluence of the second pulse probes this dependence by the response to the second pulse. With increasing fluence the strain response to the second pulse changes from purely contractive to purely expansive indicating the saturation of the magnetic stress. These findings demonstrate the capability to study spatio-temporal magnetic excitations by ultrafast X-ray diffraction using the Grüneisen model to describe the subsystem-separated ultrafast stress.

Kurzfassung

In dieser Arbeit präsentiere ich die mit ultraschneller Röntgenbeugung gemessene zeitaufgelöste Dehnung in Strontium Ruthenat und Dysprosium als Funktion der magnetischen Ordnung. Unterhalb der magnetischen Ordnungstemperatur führt die Anregung der magnetischen Freiheitsgrade zu einer zusätzlichen kontraktiven Spannung in beiden Metallen, die die ultraschnelle Ausdehnung reduziert und unkonventionelle Dehnungswellen in Dysprosium erzeugt. Die Modellierung der zeitaufgelösten Dehnung offenbart die raum-zeitliche Spannung, die sich als Superposition der Beiträge von Phononen und magnetischen Anregungen ergibt. Um diese Beiträge der Subsysteme individuell zu beschreiben, verwende ich das thermodynamische Konzept von Grüneisen Parametern. Die verwendeten subsystemspezifischen Grüneisen Konstanten beschreiben die lineare Beziehung zwischen einer deponierten Energiedichte und einem Spannungsbeitrag, der die Zeitabhängigkeit der Anregung des Subsystems durch die Kopplung zu den anderen Subsystemen erbt.
Eine besondere Eigenschaft der magnetischen Spannung, neben ihrer kontraktiven Natur, ist ihre maximale Amplitude, die aus einem endlichen Integral der magnetischen Wärmekapazität resultiert und mit einer vollständigen Demagnetisierung assoziiert ist. Die temperatur- und fluenzabhängige Sättigung der magnetischen Spannung bedingt eine temperatur- und fluenzabhängige Gesamtspannung, die die induzierte Dehnung innerhalb der Probe beeinflusst. Die laserinduzierte Gesamtspannung in Strontium Ruthenat verdeutlicht die sich ändernde Temperaturabhängigkeit aufgrund einer fluenzbedingten Sättigung des magnetischen Spannungsbeitrags für den Fall einer ultraschnellen Equilibrierung der Subsysteme. Für hohe Fluenzen wird die magnetische Spannung durch das temperaturabhängige Integral der verbleibenden magnetischen Wärmekapazität bestimmt. Im Gegensatz dazu hängt die magnetische Spannung für kleine Fluenzen von der temperaturabhängigen magnetischen Wärmekapazität ab.
Für die inhomogen angeregte Dysprosiumschicht führt die Sättigung der magnetischen Spannung zu einem tiefenabhängigen Vorzeichen der Gesamtspannung, das sich zeitlich aufgrund des langlebigen Nichtgleichgewichts der Phononen und der magnetischen Anregungen ändert. Im vollständig demagnetisierten vorderen Teil der Schicht dominiert die expansive Phonon Spannung und induziert eine bipolare Schallwelle. Im Gegensatz dazu dominiert im hinteren Teil der Schicht die nicht gesättigte, kontraktive, magnetische Spannung und treibt eine expansive Schallwelle in das Substrat. Diese beiden Beiträge überlagern sich und bestimmen die unkonventionellen Dehnungspulse, die aus einer asymmetrischen bipolaren Schallwelle und einer voranlaufenden Expansion bestehen und in einer vergrabenen Detektionsschicht beobachtet werden. Die räumliche Ausdehnung des vollständig demagnetisierten Teils des Films ist fluenzabhängig. Diese Abhängigkeit wird experimentell mit Hilfe eines Doppelpulsexperiments überprüft. Dabei wird die Fluenz des zweiten Anregungspulses konstant gehalten, während die der ersten Anregung systematisch erhöht wird. Mit zunehmender Fluenz ändert sich die Dehnungsantwort zur zweiten Anregung von ausschließlich kontraktiv zu ausschließlich expansiv, was die Sättigung der magnetischen Spannung durch den ersten Puls indiziert. Diese Ergebnisse demonstrieren das Potential von ultraschneller Röntgenbeugung die räumlichen und zeitlichen magnetischen Anregungen zu untersuchen, indem ein Grüneisen Model für die Beschreibung der subsystemspezifischen Spannungsbeiträge verwendet wird.

Acknowledgements

I would like to take this opportunity to thank the UDKM team as a whole which provides a positive, helpful and pleasant working atmosphere. I hope we can preserve the interest in each other's work and the many discussions that result in a broad learning from each other.

Firstly, the enthusiasm and the many critical questions from Prof. Dr. Matias Bargheer were very enriching and pleasant experiences. I am very grateful for the many discussions that have always led to new perspectives in the interpretation of the measurements or in the understanding of the underlying physical processes. I look forward to further cooperation in the framework of my PhD studies.

In particular, I would like to thank Alexander von Reppert for his intensive supervision of the dysprosium project and the discussions about the basic principles of picosecond ultrasonics. I have profited a lot from his experience in scientific work and from his versatile literature references. Furthermore, I am grateful for his advices on my master thesis and for supervising the measurement when I had to sleep.

Special thanks goes to Jan Pudell who introduced me to the complicated setup of the plasma X-ray source in numerous hours and helped me to set up and carry out the first ultrafast diffraction experiments. I enjoyed the detailed explanations and the joint reconstructions and long measurement nights and I am very grateful for the technical and experimental support also on the weekend.

I thank Dr. Marc Herzog for his comments on this work, which have improved its structure and comprehensibility. I really enjoyed our talks about physics and sailing.

My dearest Valentina with you at my side I can overcome all problems and setbacks, since you are my home full of peace and happiness. Words can never express my gratitude for your support and your faith in me.

A last special mention goes to my parents, my sister and all my friends, who have always supported me.

CONTENTS

Chapter One

Introduction

The atomic arrangement and spacing in a solid corresponds to a minimum in the Helmholtz free energy and determines the mechanical, electrical, optical and magnetic properties of the material in equilibrium. One way to study the fundamental contributions to the Helmholtz free energy and the associated attractive and repulsive forces between the atoms is to investigate the effect of their excitation on the interatomic distances. Studying the rising of these interatomic forces on their intrinsic time- and length-scales requires an experiment with sub-picosecond time and sub-nanometer spatial resolution on a nanometric thin film.

The field of picosecond ultrasonics subsumes time-resolved experiments that probe the lattice constant change as response to the optical excitation of an opto-mechanical transducer material [1–3]. Historically, this kind of experiment is conducted on non-magnetic metals and yields insight into the fundamental processes such as electron-phonon coupling [4–6] and hot electron propagation [7, 8]. The experimental approach is based on the deterministic relation between the strain response and a laser-induced stress, which inherits the time- and length-scales of the energy transfer processes in the transducer material. In metals the energy transfer from the laser-excited electrons to phonons is the dominant process determining the spatio-temporal stress. In recent years, the thermodynamic concept of a Grüneisen parameter has been used to describe the electron-phonon stress in non-magnetic materials even on ultrafast timescales [6, 9–14]. The Grüneisen approach linearly relates the energy density deposited in both the electrons and the phonons to a stress contribution via a subsystem-specific Grüneisen constant [15, 16]. Historically, the Grüneisen constant was introduced to describe the simultaneous contribution of the quantum excitations in phonon modes to the heat capacity and the volumetric thermal expansion [17]. This was further generalised to electronic excitations [18, 19]. The material-specific electronic and phononic Grüneisen constants are frequently used to analyse the laser-induced strain pulses in metals [6, 9–11] and to provide insight into the nanoscopic heat transport in metallic heterostructures exhibiting different electron-phonon coupling strength [12, 13].

In magnetic metals the magnetic order represents an additional energy reservoir and the magnetic excitations provide an additional stress contribution. The demagnetisation-induced stress results in a spontaneous magnetostriction both in equilibrium [20–25] and on ultrafast timescales [26–32]. The analysis of the picosecond strain response enables the investigation of spin-lattice interactions in the time-domain. Despite the absence of a unified, microscopic theory of magnetostriction, the thermodynamic approach of a magnetic Grüneisen constant [18, 19, 33, 34] is rarely used to describe the underlying ultrafast magnetic stress contribution [27–29, 35, 36]. This magnetic stress contribution and its influence on the strain response have been little studied so far. A recent publication [32] uses a double-pulse excitation scheme to extract the magnetic stress contribution in iron-platinum as function of the transient demagnetisation induced by the first pulse. The experimental results linearly relate the magnetic stress contribution to the energy density storable to the magnetic subsystem given by the integral of the remaining heat capacity. These findings indicate a saturation of the magnetic stress that relates to a full demagnetisation of the material.

In general, the strain response depends on the temperature- and fluence-dependent excitation of the magnetic subsystem and provides the possibility to manipulate strain pulses by the temperature and the fluence [27–29]. This raises the questions "How can the phononic and magnetic stress be separated on picosecond timescale?" and "How does the saturability of the magnetic stress influence the ultrafast expansion and strain waves?". The manipulation of picosecond strain pulses by magnetic excitations in a transducer may be useful for scenarios of strain assisted magnetisation manipulation [37, 38] that could possibly extend the recently presented heat assisted magnetic recording (HAMR) scheme [39, 40]. Here, the traversing strain pulses modify the crystal field anisotropy, which deterministically [41, 42] results in magnetisation dynamics [38, 43, 44]. Other application scenarios involve the study of materials with pressure-dependent phase transitions that could be subjected to a picosecond strain pulse and the search for an ultrafast invar-material that could be used for a local heat source that does not generate picosecond strain pulses.

In this thesis I investigate the effect of the laser-induced demagnetisation on the picosecond strain response. I apply the thermodynamic Grüneisen concept to separate the total ultrafast stress into the contributions of the phonons and the magnetic excitations. The subsystem-separated total stress exemplifies the relation between the spatio-temporal magnetic excitations and the ultrafast expansion given by a linear-chain model of masses and springs.

In the second chapter I introduce the central terms stress and strain as tensor quantities and identify the stress as driving force for strain both in thermal equilibrium and on ultrafast timescales. The picosecond strain response in a continuous film is described by a one-dimensional inhomogeneous wave equation. The comparison to the expansion in thermal equilibrium highlights the absence of a Poisson stress on ultrashort timescales due to the suppressed in-plane lattice motion. In the following chapter I present the thermodynamic Grüneisen concept for electrons, phonons and magnetic excitations, that linearly relates a deposited energy density to a stress via subsystem-specific Grüneisen constants. The application of this approach to the non-equilibrium after laser excitation results in a general equation for the ultrafast stress. A linear-chain model of masses and springs relates this stress to a strain response. Its comparison to the measurements verifies the stress model. In chapter four I describe the basic principles of X-ray diffraction and the generation of sub-picosecond X-ray pulses by a laser-based table-top plasma X-ray source, which I use to probe the transient strain response of the sample structures.

In the fifth and sixth chapter of the thesis I present the temperature- and fluence-dependent strain response induced by the optical excitation of strontium ruthenate and dysprosium. For both materials I determine the Grüneisen constants of phonons and magnetic excitations using the heat capacity and the thermal expansion in equilibrium. The time-resolved investigation of the two materials demonstrates the capability of the Grüneisen model to describe the strain response and the subsystem-specific stress both for an ultrafast subsystem equilibration in the homogeneously excited strontium ruthenate film and for a long lasting non-equilibrium of phonons and magnetic excitations in the inhomogeneously excited dysprosium film. The Grüneisen model enables the separation of the phononic and magnetic stress and reveals the influence of the magnetic stress on the strain pulses in both complementary scenarios. In both materials the saturation of the magnetic stress provides a temperature- and fluence-dependent ultrafast expansion that affects the laser-generated strain pulses. This saturation can be probed experimentally by observing the strain response to a second, delayed excitation pulse. The results indicate the capability of UXRD to probe the saturation of the energy transfer to magnetic excitations independently of the magnetic order and the versatility of the Grüneisen model for the analysis of the driving stress.

CHAPTER TWO

STRAIN WAVES IN AN ELASTIC SOLID

Strain and especially strain waves driven by a laser-induced stress are the core of this work. This chapter is designed to introduce the fundamental definitions and relations of stress and strain that are subsequently used in the description of thermal expansion and strain waves in thermal equilibrium and on ultrafast timescales respectively.
The quantity strain η denotes the deformation of the unit cell of a crystalline solid. This deformation is driven by a force per unit area denoted as stress σ. Measuring the strain response therefore provides insight into the microscopic stress mechanisms both in equilibrium and on ultrafast timescales. In case of anisotropic three dimensional solids the quantities stress σ and strain η are tensors. The first section associates their linear relation in the regime of small strains with a generalised anisotropic three-dimensional Hooke's law provided by the elastic tensor c that depends on the interatomic potentials. Subsequently, I identify the Poisson and external stress contribution to the anisotropic expansion in thermal equilibrium. In the second section I extend the discussion to time-dependent strain dynamics that are described by the wave equation. The solution of the inhomogeneous wave equation including time-dependent laser-induced stress is discussed and indicates clearly the deterministic character of the strain response.

2.1 Elastic tensor and equilibrium expansion

Before turning to the time-dependent phenomena this section provides the used nomenclature and the basic relations of the elastic properties of a solid to discuss quasi-static strain. The expansion or contraction of solids with changing temperature is part of the daily experience and a general macroscopic property of solids. This potentially anisotropic thermal strain η is caused by the stress σ representing a generalised anisotropic pressure. The elastic tensor c couples stress and strain linearly in the regime of small strain amplitudes ($\eta < 1\,\%$). This generalised form of Hooke's law determines the anisotropic deformation of the solid in quasi-equilibrium, where the relaxation of all degrees of freedom provides a Poisson stress. In this section I present the influence of cubic and hexagonal crystal symmetries on the elastic tensor and the equilibrium expansion.

2.1.1 Stress and strain as tensor quantities

The following paragraphs introduce the tensor notation of stress and strain that is used to describe the anisotropic lattice deformation and the underlying anisotropic stress. In crystalline solids the internal forces are not described by an isotropic pressure p but by an anisotropic stress σ as a generalised pressure accounting for the crystal symmetry. The force $\vec{F}$ on an area A is composed of one normal and two tangential components as depicted in figure 2.1(a). The application of this separation to the surface of an infinitesimal volume element (b) defines the stress tensor σ_{ij}, where the first index denotes the direction of the force acting on the surface and the second index indicates the direction of the surface normal. Due to the internal character of the stress,

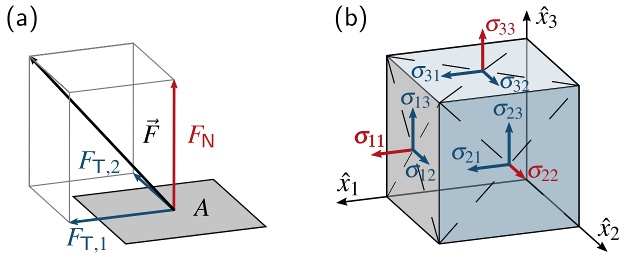

Figure 2.1: Definition of an anisotropic stress σ_{ij} as force $\vec{F}$ acting on an area A separated into one normal and two tangential components (a) that acts on surfaces of an infinitesimal volume corresponding to the stress tensor elements (b).

translational and rotational forces should vanish. This condition is fulfilled in case of a symmetric stress tensor ($\sigma_{ij} = \sigma_{ji}$) leading to a compensation of the stress within the coordinate planes of the volume element [45, p. 147]. The symmetric stress tensor with six independent coefficients is

$$\sigma_{ij} = \begin{bmatrix} \sigma_{11} & \sigma_{12} & \sigma_{13} \\ \sigma_{12} & \sigma_{22} & \sigma_{23} \\ \sigma_{13} & \sigma_{23} & \sigma_{33} \end{bmatrix} \tag{2.1}$$

where the off-diagonal elements denote shear stress corresponding to a force acting parallel on an area. The elastic solid described by three orthogonal unit vectors $\hat{x}_1$, $\hat{x}_2$ and $\hat{x}_3$ responds with a reversible deformation η_{ij} to this stress. This deformation leads to a new coordinate system described by the three vectors $\hat{x}'_1$, $\hat{x}'_2$ and $\hat{x}'_3$:

$$\begin{aligned} \hat{x}'_1 &= (1+\eta_{11})\hat{x}_1 + \eta_{12}\hat{x}_2 + \eta_{13}\hat{x}_3 \\ \hat{x}'_2 &= \eta_{21}\hat{x}_1 + (1+\eta_{22})\hat{x}_2 + \eta_{23}\hat{x}_3 \\ \hat{x}'_3 &= \eta_{31}\hat{x}_1 + \eta_{32}\hat{x}_2 + (1+\eta_{33})\hat{x}_3 \end{aligned} \tag{2.2}$$

where the length of the new basis vectors differs from unity ($\hat{x}'_1 \cdot \hat{x}'_1 \neq 1$) and the basis vectors are no longer orthogonal ($\hat{x}'_1 \cdot \hat{x}'_2 \neq 0$). The deformation also changes the position of an atom $\vec{r} = x_1\hat{x}_1 + x_2\hat{x}_2 + x_3\hat{x}_3$ in the solid. This displacement may be described by a displacement vector $\vec{R}$ [45, p. 150]:

$$\begin{aligned} \vec{R}(\vec{r}) &= u_1(\vec{r})\hat{x}_1 + u_2(\vec{r})\hat{x}_2 + u_3(\vec{r})\hat{x}_3 \\ &= x_1(\hat{x}'_1 - \hat{x}_1) + x_2(\hat{x}'_2 - \hat{x}_2) + x_3(\hat{x}'_3 - \hat{x}_3) \,. \end{aligned} \tag{2.3}$$

The Taylor expansion of the direction-dependent displacement $u_i(\vec{r})$ for small displacements relates the strain tensor η_{kl} to the spatial derivatives of the displacement:

$$\eta_{kl} = \frac{1}{2}\left(\frac{\partial u_l}{\partial x_k} + \frac{\partial u_k}{\partial x_l}\right) \,. \tag{2.4}$$

This relation clearly indicates the symmetry of the strain tensor ($\eta_{kl} = \eta_{lk}$). Thus the strain tensor η_{kl} has six independent coefficients that read:

$$\eta_{kl} = \begin{bmatrix} \eta_{11} & \eta_{12} & \eta_{13} \\ \eta_{12} & \eta_{22} & \eta_{23} \\ \eta_{13} & \eta_{23} & \eta_{33} \end{bmatrix} \,. \tag{2.5}$$

2.1.2 Hooke's law for crystalline solids

This section introduces the strain-independent elastic tensor c that linearly relates the stress σ_{ij} and the strain η_{ij} in the regime of small strains. This generalised Hooke's law determines the anisotropic thermal expansion in thermal equilibrium that depends on a temperature-induced external stress and a Poisson stress induced by the expansion along other crystal directions. According to Hooke's law the elongation of a harmonic oscillator is associated with an elastic energy determined by the elastic constants. In the simple case of a single, one-dimensional harmonic oscillator with masses at positions R and R' the energy is

$$U^{\mathrm{harm}} = -\frac{1}{4}\left[u_i(R') - u_i(R)\right] D_{ii}(R-R') \left[u_i(R') - u_i(R)\right] = \frac{1}{2} k \Delta u_i^2 \tag{2.6}$$

wherein $u_i(R)$ denotes the displacement of the mass at R and $D_{ii}(R-R')$ denotes the negative second derivative of the potential [46, p. 443], which corresponds to two times the spring constant k. This simple case is extended to a three dimensional lattice by the different directions $\hat{x}_1$, $\hat{x}_2$ and $\hat{x}_3$ and masses at the different lattice positions. A small-amplitude displacement field $u(r)$ at R' can be approximated by the Taylor expansion $u(R') = u(R) + (R'-R)\cdot\nabla u(r)|_{r=R}$. Following [46, p. 444] this transforms equation (2.6) to:

$$U^{\mathrm{harm}} = \frac{1}{2}\sum_{R,ijkl}\left(\frac{\partial}{\partial x_i}u_j(R)\right)\left(\frac{\partial}{\partial x_k}u_l(R)\right)c_{ijkl} = \frac{1}{2}\sum_{R,ij}\sigma_{ij}(R)\eta_{ij}(R) \tag{2.7}$$

where the elastic tensor c_{ijkl} denotes a generalised spring constant. The second identity in equation (2.7) relates the harmonic energy to the product of a generalised force σ_{ij} and a deformation η_{ij} according to Hooke's law using the relation between displacement and strain (2.4). The comparison of the second and the third term relates the stress σ_{ij} to the strain η_{kl} according to a generalised Hooke's law:

$$\sigma_{ij} = \sum_{kl} c_{ijkl}\eta_{kl}\,. \tag{2.8}$$

The elastic tensor c_{ijkl} is a tensor of rank four with, in general, 81 independent parameters. However, the number of independent coefficients is reduced to 36 due to the inherited symmetry from the stress and strain tensor. Due to this symmetry equation (2.8) becomes invariant for interchanging the indices $i \leftrightarrow j$ and $k \leftrightarrow l$. Therefore there are only six different combinations for the index pairs ij and kl. These six different combinations can be abbreviated using the following Voigt notation*:

$$x_1x_1 \to 1,\quad x_2x_2 \to 2,\quad x_3x_3 \to 3,\quad x_2x_3 \to 4,\quad x_1x_3 \to 5,\quad x_1x_2 \to 6\,. \tag{2.9}$$

The six independent combinations in equation (2.9) include three normal $(1,2,3)$ and three shear stress contributions $(4,5,6)$. Using the Voigt notation given in equation (2.9) the three-dimensional Hooke's law (2.8) transforms to†:

$$\sigma_\lambda = \sum_{\mu=1}^{6} c_{\lambda\mu}\eta_\mu = \sum_{\mu=1}^{6}\frac{\partial\sigma_\lambda}{\partial\eta_\mu}\eta_\mu\,. \tag{2.10}$$

In case of small strains η_μ the Taylor expansion of the stress $\sigma_\lambda(\eta_\mu)$ defines the second identity in equation (2.10) and shows the elastic tensor $c_{\lambda\mu}$ to be the parameter describing the strain-caused change of the stress. In analogy to $\mathrm{d}U = p\mathrm{dV}$ at constant entropy, the differential of the elastic energy (2.7) writes $\mathrm{d}U^{\mathrm{harm}} = \sum_\lambda \sigma_\lambda\,\mathrm{d}\eta_\lambda$. For the internal energy U and the free energy F this

---

*In the following I will use roman indices for the cartesian directions and greek indices to indicate when Voigt notation is used.

†Note, the change of the notation introduces a factor of two for the the off-diagonal elements of the strain tensor [45, p. 152]:

$$\sigma_{11} = c_{1111}\eta_{11} + c_{1122}\eta_{22} + c_{1133}\eta_{33} + 2c_{1123}\eta_{23} + 2c_{1113}\eta_{13} + 2c_{1112}\eta_{12}$$

$$\sigma_1 = c_{11}\eta_1 + c_{12}\eta_2 + c_{13}\eta_3 + c_{14}\eta_4 + c_{15}\eta_5 + c_{16}\eta_6\,.$$

leads to a Maxwell relation both for adiabatic (entropy $S = const.$) and isothermal (temperature $T = const.$) spatial dimension changes, respectively:

$$c_{\lambda\mu} = \left.\frac{\partial^2 U}{\partial\eta_\lambda \partial\eta_\mu}\right|_S = \left.\frac{\partial^2 F}{\partial\eta_\lambda \partial\eta_\mu}\right|_T = c_{\mu\lambda} \tag{2.11}$$

wherein the interchangeability of the partial derivations causes the invariance of the elastic tensor for a change of λ and μ reducing the independent coefficients to 21 [47, p. 136]. This symmetry simplifies the relation between strain η_μ and stress σ_λ in equation (2.10) and results in:

$$\begin{aligned}
\sigma_1 &= c_{11}\eta_1 + c_{12}\eta_2 + c_{13}\eta_3 + c_{14}\eta_4 + c_{15}\eta_5 + c_{16}\eta_6 \\
\sigma_2 &= c_{12}\eta_1 + c_{22}\eta_2 + c_{23}\eta_3 + c_{24}\eta_4 + c_{25}\eta_5 + c_{26}\eta_6 \\
\sigma_3 &= c_{13}\eta_1 + c_{23}\eta_2 + c_{33}\eta_3 + c_{34}\eta_4 + c_{35}\eta_5 + c_{36}\eta_6 \\
\sigma_4 &= c_{14}\eta_1 + c_{24}\eta_2 + c_{34}\eta_3 + c_{44}\eta_4 + c_{45}\eta_5 + c_{46}\eta_6 \\
\sigma_5 &= c_{15}\eta_1 + c_{25}\eta_2 + c_{35}\eta_3 + c_{45}\eta_4 + c_{55}\eta_5 + c_{56}\eta_6 \\
\sigma_6 &= c_{16}\eta_1 + c_{26}\eta_2 + c_{36}\eta_3 + c_{46}\eta_4 + c_{56}\eta_5 + c_{66}\eta_6
\end{aligned} . \tag{2.12}$$

Equations (2.12) relate the strain components of the solid to a stress σ_λ as generalised internal restoring force. In the following this relation is extended by including also an external stress $\sigma_\lambda^{\text{ext}}$. This thermoelastic external stress induced by a temperature increase ΔT counteracts the elastic internal stress σ_λ. Since an equilibrium situation corresponds to a vanishing total stress $\sigma_\lambda^{\text{tot}} = \sigma_\lambda - \sigma_\lambda^{\text{ext}} = 0$, a positive external stress ($\sigma_\lambda^{\text{ext}} > 0$) induces an expansion ($\eta_\lambda > 0$). Inserting the internal stress σ_λ according to equation (2.12) defines the strain response to an external stress:

$$\eta_\lambda = \frac{\sigma_\lambda^{\text{ext}}}{c_{\lambda\lambda}} - \sum_{\mu\neq\lambda} \frac{c_{\lambda\mu}}{c_{\lambda\lambda}} \eta_\mu \tag{2.13}$$

wherein the strain components η_μ contain the external stress components σ_μ^{ext}. Equation (2.13) shows that the strain response η_λ is reduced relative to an external stress $\sigma_\lambda^{\text{ext}}$ by the other strain components η_μ via the off-diagonal elements of the elastic tensor. These strain components form the Poisson stress $\sigma_\lambda^{\text{poi}} = \sum_{\mu\neq\lambda} c_{\lambda\mu}\eta_\mu$. The six non-equivalent equations (2.13) for $\lambda \in \{1,2,3,4,5,6\}$ form a linear system of equations and guarantee a solution for the six independent strain components η_λ given by the elastic tensor $c_{\lambda\mu}$ and the external stress components $\sigma_\lambda^{\text{ext}}$. However, the solution including the full elastic tensor with 21 independent coefficients is rather complicated and is not discussed here.

The following paragraphs describe the simplification of the elastic tensor by the crystal symmetry reducing the number of independent coefficients. In chapter 5 and 6 I investigate pseudocubic and hexagonal systems, therefore I derive the corresponding elastic tensors in the following. For both systems the rotation symmetry is an important symmetry operation. The invariance of the elastic tensor under rotations of the coordinate system can be expressed as:

$$c_{ijkl} = \Phi_i \Phi_j \Phi_k \Phi_l c_{ijkl} \tag{2.14}$$

with the rotation matrix Φ. The general form of the rotation matrix for a x_3-axis rotation is:

$$\Phi_3(\phi) = \begin{bmatrix} \cos\phi & \sin\phi & 0 \\ -\sin\phi & \cos\phi & 0 \\ 0 & 0 & 1 \end{bmatrix} . \tag{2.15}$$

The number of equivalent orientations within a rotation of 2π corresponds to the order of the rotation axis and determines the angle ϕ. The cubic crystal exhibits three orthogonal, two-fold

axes ($\phi = \pi$) [47, p. 140f], which cause non-zero elastic coefficients only for an even occurrence of the directions x_1, x_2 and x_3. In Voigt notation (2.9) this coincides with $c_{\lambda\mu} = 0$ in case of $\lambda \neq \mu$ and $\mu \in \{4,5,6\}$ leading to a block-diagonal shape.
Furthermore, the cubic crystal exhibits a triad axis in [111]-direction, which induces an invariance under rotation by $2\pi/3$ about this axis. This rotation represents a cyclic permutation of the indices $x_1x_2x_3$ and induces an invariance of the elastic tensor under this permutation [47, p. 141]. This symmetry analysis of the cubic crystal structure reduces the number of independent elastic constants to three:

$$c_{\lambda\mu}^{\text{cubic}} = \begin{bmatrix} c_{11} & c_{12} & c_{12} & 0 & 0 & 0 \\ c_{12} & c_{11} & c_{12} & 0 & 0 & 0 \\ c_{12} & c_{12} & c_{11} & 0 & 0 & 0 \\ 0 & 0 & 0 & c_{44} & 0 & 0 \\ 0 & 0 & 0 & 0 & c_{44} & 0 \\ 0 & 0 & 0 & 0 & 0 & c_{44} \end{bmatrix} . \tag{2.16}$$

In contrast to cubic crystals the hexagonal crystal structure exhibits a sixth order principal axis corresponding to $\phi = \pi/3$ in the rotation matrix (2.15). The diagonalisation of the resulting rotation matrix with their eigenvalues and eigenvectors reduces the number of independent elastic coefficients to five [47, p. 142ff]. However, both the cubic and hexagonal symmetry suppresses the coupling of shear strain ($\mu \in \{4,5,6\}$) to the normal strain ($\lambda \in \{1,2,3\}$) as seen from the block-diagonal form of $c_{\lambda\mu}$.

$$c_{\lambda\mu}^{\text{hexagonal}} = \begin{bmatrix} c_{11} & c_{12} & c_{13} & 0 & 0 & 0 \\ c_{12} & c_{11} & c_{13} & 0 & 0 & 0 \\ c_{13} & c_{13} & c_{33} & 0 & 0 & 0 \\ 0 & 0 & 0 & c_{44} & 0 & 0 \\ 0 & 0 & 0 & 0 & c_{44} & 0 \\ 0 & 0 & 0 & 0 & 0 & \frac{c_{11}-c_{12}}{2} \end{bmatrix} \tag{2.17}$$

The following paragraphs discuss the explicit dependence of the strain η_λ on the external stress components $\sigma_\lambda^{\text{ext}}$ with $\lambda \in \{1,2,3\}$ neglecting shear stress and strain in a cubic crystal. Using the corresponding simplified, block-diagonal elastic tensor, the equilibrium strain in equation (2.13) relates to the external stress by:

$$\eta_\lambda^{\text{cubic}} = \frac{(1+\tilde{\nu}) \cdot \sigma_\lambda^{\text{ext}} - \tilde{\nu} \sum\limits_{\lambda \neq \mu} \sigma_\mu^{\text{ext}}}{c_{11} \cdot (1 + \tilde{\nu} - 2\tilde{\nu}^2)} . \tag{2.18}$$

The parameter $\tilde{\nu}$ denotes the ratio of the off-diagonal c_{12} to the diagonal element c_{11}. Concerning a typical solid this ratio is smaller than one ($\tilde{\nu} < 1$) and leads to a positive denominator in equation (2.18). Therefore a positive stress $\sigma_\lambda^{\text{ext}}$ induces an expansion ($\eta_\lambda > 0$) while a positive stress σ_μ^{ext} induces a contraction ($\eta_\lambda < 0$). This inverse coupling is related to the Poisson ratio $\nu = -\frac{\eta_\mu}{\eta_\lambda}$ in case of an uniaxial stress σ_λ and $\lambda, \mu \in \{1,2,3\}$. Inserting equation (2.18) determines the known Poisson ratio of isotropic or cubic solids to $\nu = \frac{C_{12}}{C_{11}+C_{12}}$ [47, p. 140]. Assuming an uniaxial stress $\sigma_\lambda^{\text{ext}}$ simplifies equation (2.18) and exemplifies the influence of the Poisson effect:

$$\eta_\lambda^{\text{uni}} = \frac{\sigma_\lambda^{\text{ext}}}{c_{11}} \cdot \frac{1+\tilde{\nu}}{1+\tilde{\nu}-2\tilde{\nu}^2} > \frac{\sigma_\lambda^{\text{ext}}}{c_{11}} = \eta_\lambda^c . \tag{2.19}$$

Here, η_λ^c denotes the strain driven by an external stress under the condition of all other strain components are clamped ($\eta_{\mu \neq \lambda} = 0$). According to equation (2.13) this strain is direct proportional to the external stress via the diagonal element of the elastic tensor c_{11}. The enhanced strain $\eta_\lambda^{\text{uni}}$

in case of uniaxial stress is caused by the Possion effect of the non-vanishing transverse strains. An uniaxial expansive stress $\sigma_\lambda^{\text{ext}}$ induces a contraction perpendicular to the direction of the applied stress $\eta_{\mu\neq\lambda} < 0$ (see equation (2.18)), which causes a negative internal stress. This additional negative restoring force enhances the induced strain $\eta_\lambda^{\text{uni}}$ according to equation (2.13).

2.2 Elastic dynamics described by the wave equation

After the introduction of the tensor quantities stress and strain and their quasi-static relation, this section introduces the wave equation to describe the time-dependent strain that is driven by a spatial gradient of both elastic and external stress. In equilibrium the thermal expansion is determined by the elastic properties of the sample and corresponds to a vanishing of both spatial and temporal heater-induced stress gradients. Since dynamics are in general driven by gradients, in equilibrium no strain dynamics are expected. In this section the additional introduced spatial and temporal stress gradients drive strain waves as elastic response. The first part of the section introduces the homogeneous wave equation describing the strain waves driven by internal stress gradients. The second part extends the discussion by an additional external stress gradient. I provide the solution to the inhomogeneous wave equation for different stress rise times in a simple, experimental relevant transducer-substrate geometry to exemplify the capability of the strain response to indicate spatio-temporal stress.

2.2.1 Homogeneous wave equation in crystalline solids

Before turning to the description of laser-induced dynamics, this section introduces the homogeneous wave equation to describe strain dynamics in the simplified case of vanishing external stress. The general solution of the wave equation is a strain wave propagating with sound velocity. An effective translational force in direction $\hat{x}_i$ for an infinitesimal volume element is given by the spatial change of the anisotropic stress $\sum_j \nabla_j \sigma_{ij}$. According to Newton's Second law this force density is related to a mass density ρ^m times an acceleration $\ddot{u}_i$ of the displacement u_i in $\hat{x}_i$-direction. The definition of the strain η_{kl} (2.4) and its relation to the stress σ_{ij} via the elastic constants in equation (2.8) leads to the homogeneous wave equation:

$$\rho^m \frac{\partial^2 u_i}{\partial t^2} = \sum_j \frac{\partial \sigma_{ij}}{\partial x_j} = \sum_{jkl} \frac{c_{ijkl}}{2} \left(\frac{\partial^2 u_l}{\partial x_j \partial x_k} + \frac{\partial^2 u_k}{\partial x_j \partial x_l} \right) . \tag{2.20}$$

Inserting the elastic constants for the cubic (2.16) and hexagonal (2.17) symmetry simplifies this wave equation. Concerning the $\hat{x}_3$-direction there are three stress contributions σ_{33}, σ_{23} and σ_{13} corresponding to σ_3, σ_4 and σ_5 in Voigt notation, respectively. For the cubic crystal the wave equation transforms to:

$$\rho^m \frac{\partial^2 u_3}{\partial t^2} = c_{11} \frac{\partial^2 u_3}{\partial x_3^2} + c_{44} \left(\frac{\partial^2 u_3}{\partial x_1^2} + \frac{\partial^2 u_3}{\partial x_2^2} \right) + (c_{12} + c_{44}) \left(\frac{\partial^2 u_1}{\partial x_3 \partial x_1} + \frac{\partial^2 u_2}{\partial x_3 \partial x_2} \right) . \tag{2.21}$$

The wave equations for the displacements u_2 and u_3 in directions $\hat{x}_2$ and $\hat{x}_3$ result directly from cyclic permutation of equation (2.21). Using the elastic constants for a hexagonal lattice (2.17), the general wave equation transforms to:

$$\rho^m \frac{\partial^2 u_3}{\partial t^2} = c_{33} \frac{\partial^2 u_3}{\partial x_3^2} + c_{44} \left(\frac{\partial^2 u_3}{\partial x_1^2} + \frac{\partial^2 u_3}{\partial x_2^2} \right) + (c_{13} + c_{44}) \left(\frac{\partial^2 u_1}{\partial x_3 \partial x_1} + \frac{\partial^2 u_2}{\partial x_3 \partial x_2} \right) . \tag{2.22}$$

In contrast to the homogeneous wave equation in case of cubic symmetry, the wave equations of the displacements u_2 and u_3 in directions $\hat{x}_2$ and $\hat{x}_3$ are not directly given by cyclic permutation due to the additional independent diagonal elastic tensor coefficients in case of hexagonal symmetry.

These homogeneous wave equations of cubic and hexagonal crystals reveal the relations between sound velocities v and elastic tensor elements for both longitudinal and transversal elastic waves. In case of a propagation in $\hat{x}_3$-direction the sound velocities are given by inserting the general solutions (2.23) and (2.24) to the wave equation in the crystal structure specified wave equations (2.21) and (2.22). The longitudinal elastic wave with the displacement parallel to the propagation direction as solution to the wave equation is:

$$u_3(x_3,t) = u_{3,0} \exp\left[i(kx_3 - \omega t)\right] \ . \tag{2.23}$$

In case of cubic and hexagonal crystals this ansatz leads to the relation $\omega^2 \rho^m = c_{11} k^2$ and $\omega^2 \rho^m = c_{33} k^2$ with the sound velocities $\sqrt{\frac{c_{11}}{\rho^m}}$ and $\sqrt{\frac{c_{33}}{\rho^m}}$, respectively. The general form of a transversal strain wave with the displacement orthogonal to the propagation direction is given by:

$$u_{1/2}(x_3,t) = u_{1/2,0} \exp\left[i(kx_3 - \omega t)\right] \tag{2.24}$$

where the resulting sound velocities in cubic and the hexagonal crystals is $\sqrt{\frac{c_{44}}{\rho^m}}$ [45, p. 165]. These ansatz (2.23) and (2.24) are formulated for the main symmetry directions and become more complicated for arbitrary crystal directions.

2.2.2 Inhomogeneous wave equation describes laser-induced dynamics

Introducing a laser-induced external stress in the homogeneous wave equation changes the driven strain dynamics. In the following paragraphs I discuss the strain dynamics in the experimentally studied situation of a time-dependent external stress and a transducer-substrate geometry to provide first insight how the spatio-temporal stress influences the strain response.

According to the homogeneous wave equation of crystal structures the elastic tensor elements determine the sound velocity v of propagating elastic waves driven by an internal stress gradient. In an ultrafast pump-probe experiment an additional stress gradient $\nabla_i \sigma_i^{\text{ext}}$ is induced by the laser excitation, which extends the previous discussion by introducing a forcing into the strain dynamics. They are then described by the inhomogeneous wave equation:

$$\rho^m \frac{\partial^2 u_i}{\partial t^2} = \sum_j \frac{\partial(\sigma_{ij} - \sigma_{ij}^{\text{ext}})}{\partial x_j} = \sum_{jkl} c_{ijkl} \frac{\partial^2 u_l}{\partial x_j \partial x_k} - \frac{\partial \sigma_{ij}^{\text{ext}}}{\partial x_j} \ . \tag{2.25}$$

The inhomogeneous wave equation indicates two stress contributions with opposite sign. The internal stress σ_{ij} arising in a strained solid as restoring force is counteracted by the external stress σ_{ij}^{ext}, which causes an expansion if $\sigma_{ij}^{\text{ext}} > 0$.

The wave equation describing a typical laser-pulse-based pump-probe experiment can be simplified for the limiting cases of a continuous thin film and individual small grains. The first simplification is given by the reasonable assumption of vanishing shear forces, due to the in-plane symmetry of the homogeneous excitation and the sample structure. Further assumptions specifying the general inhomogeneous wave equation are determined by the lateral excitation conditions. The significantly larger pump pulse footprint laterally excites the probed sample volume of a thin film ($\hat{x}_1$ and $\hat{x}_2$) homogeneously. This suppresses in-plane stress gradients $\nabla_{1,2} \sigma_{1,2}^{\text{ext}}$ and the lateral strain components of neighbouring unit cells cancel out due to symmetry ($\eta_{1,2} = 0$). These conditions transform the inhomogeneous wave equation (2.25) of the out-of-plane strain η_3 as the observable in X-ray diffraction to:

$$\rho^m \frac{\partial^2 u_3}{\partial t^2} = \frac{\partial}{\partial x_3} \left(c_{33} \frac{\partial u_3}{\partial x_3} - \sigma_3^{\text{ext}} \right) \ . \tag{2.26}$$

The wave equation for a continuous film (2.26) displays the absence of a Poisson stress contribution on ultrafast timescales in the thin film geometry. Therefore the picosecond strain response depends exclusively on the out-of-plane external stress σ_3^{ext} in contrast to the thermal expansion in equilibrium (2.13) where the expansion along the transverse directions provides an additional Poisson stress. In contrast to a continuous thin film, a sample of individual grains exhibits non-zero in-plane strain due to the uncompensated external stress at the grain boundaries. However, in the limit of small lateral dimensions the assumption of instantaneous strain relaxation with sound velocity can be used to obtain a simplified relation, which reads:

$$\rho^m \frac{\partial^2 u_3}{\partial t^2} = \frac{\partial}{\partial x_3}\left(c_{33}\frac{\partial u_3}{\partial x_3} + c_{13}\frac{\partial u_1}{\partial x_1} + c_{23}\frac{\partial u_2}{\partial x_2} - \sigma_3^{\text{ext}} \right) . \tag{2.27}$$

This thesis exclusively investigates continuous thin films on substrates or in heterostructures, whose dynamics after laser excitation are described by equation (2.26). Historically, the solution to this inhomogeneous wave equation was discussed for thick metal films as transducer exceeding significantly the optical penetration depth ξ [1, 2]. In the absence of interfaces the depth dependence of the laser-induced stress $\sigma_3^{\text{ext}}(x_3,t)$ in the transducer follows Lambert-Beers law with the optical penetration depth ξ. Furthermore, the temporal dependence of the stress is neglected by the assumption of instantaneous stress rise, which corresponds to an ultrafast laser pulse excitation and fast microscopic stress generation mechanisms (see Chapter 3). This assumption of negligible temporal dependence is fulfilled under the condition of $\tau \ll \frac{\xi}{v}$ for the stress rise time corresponding to $\tau \ll 5\,\text{ps}$ in a typical metal.

In general the inhomogeneous wave equation is solved by the sum of right and left propagating functions with the sound velocity v and the integral of the inhomogeneity [2]:

$$u_3 = f(x_3 - vt) + g(x_3 + vt) - \eta_{3,0}\xi e^{-\frac{-x_3}{\xi}} \tag{2.28}$$

wherein $\eta_{3,0}$ denotes the laser induced strain at $x_3 = 0$. The extension to $x_3 < 0$ and the necessary symmetry at $x_3 = 0$ determines $f(x_3) = g(-x_3)$, which defines the strain η_3 to

$$\eta_3 = \frac{\partial u_3}{\partial x_3} = f'(x_3 - vt) + f'(-x_3 - vt) - \eta_{3,0} e^{-\frac{-|x_3|}{\xi}} \operatorname{sgn}(x_3) . \tag{2.29}$$

The boundary condition $\eta_3(x_3 = 0) = \eta_{3,0}$ determines the function $f'(x_3)$ and leads to the solution to the spatio-temporal strain $\eta_3(x_3 > 0, t)$ [2]:

$$\eta_3(x_3 > 0, t) = \eta_{3,0} e^{-\frac{x_3}{\xi}} - \frac{\eta_{3,0}}{2}\left[e^{-\frac{x_3+vt}{\xi}} + e^{-\frac{|x_3-vt|}{\xi}} \operatorname{sgn}(x_3 - vt) \right] . \tag{2.30}$$

This particular solution to the inhomogeneous wave equation is depicted in figure 2.2 for different delays after laser excitation.[‡] This depiction displays a bipolar strain wave with leading compressive part propagating from the surface ($x_3 = 0$) into the layer. At the same time an exponential strain profile develops behind the expansive part of the strain wave, which remains after the strain wave has left the near-surface region. This exponential strain profile corresponds to the laser-induced stress profile and is described by the first term in equation (2.30). The third term denotes the bipolar strain wave propagating into the layer with leading compression for $x_3 > vt$. Together with the second term at $t \approx 0$ this compression compensates the expansion from incoherently excited phonons and accounts for the transformation of stress to strain with the speed of sound corresponding to the propagating strain wave.

The introduction of an additional interface extends these observations to a thin film with thickness $d \lesssim \xi$ on a transparent substrate with perfect impedance matching and equal sound velocities. The additional interface limits the laser-induced stress to the film thickness and acts as an additional

---

[‡] This solution is generalised to contractive stress by changing the global sign in equation (2.30). This inverts the driven bipolar strain wave and causes a contraction in the stressed region of the transducer at the surface.

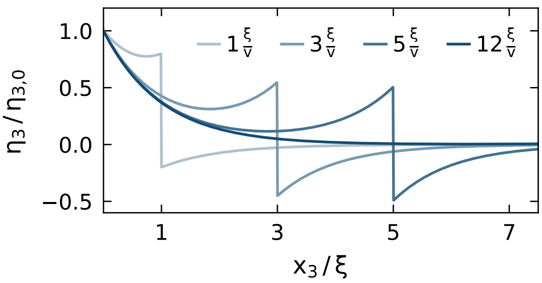

Figure 2.2: Time-dependent strain profile after laser excitation according to equation (2.30). The driven bipolar strain wave propagates with sound velocity v from the surface into the layer. The induced stress according to the optical penetration depth ξ transforms to a thermal expansion.

source of propagating strain waves due to the unbalanced stress gradient. The external stress of a thin film with time dependence $T(t)$ is given by:

$$\sigma_3^{\mathrm{ext}}(x_3>0,t)=T(t)\cdot\sigma_{3,0}e^{-\frac{x_3}{\xi}}\,\mathrm{H}(d-x_3) \tag{2.31}$$

wherein $\mathrm{H}(d-x_3)$ denotes the Heaviside function and $\sigma_{3,0}$ describes the laser-induced stress at $x_3=0$. Under the condition of an initially unstrained thin film, the displacement u_3 as solution to the inhomogeneous wave equation equation (2.26) is given by [48]:

$$u_3(x_3,t)=-\frac{1}{2v}\int\limits_0^t\left[\sigma_3^{\mathrm{ext}}(x_3+v(t-s),s)-\sigma_3^{\mathrm{ext}}(x_3-v(t-s),s)\right]\mathrm{d}s\,. \tag{2.32}$$

This solution includes an imaginary material for $x_3<0$ in front of the transducer. The solution of the half-space $x_3>0$ is conducted by the combination of two solutions $u_3(x_3\geq 0)=u_3(x_3)+u_3(-x_3)$ [48]. Without explicit time dependence of the stress, this determines the strain $\eta_3(x_3,t)$ as spatial derivation of the displacement

$$\eta_3(x_3,t)=-\frac{\mathrm{H}(x_3)}{2v}\left[2\sigma_3^{\mathrm{ext}}(x_3)-\sigma_3^{\mathrm{ext}}(x_3+vt)+\sigma_3^{\mathrm{ext}}(-x_3+vt)-\sigma_3^{\mathrm{ext}}(x_3-vt)\right]\ . \tag{2.33}$$

Here, the external stress σ_3^{ext} fulfils the condition $\sigma_3^{\mathrm{ext}}(x_3<0)=0$, which should be considered for the third and fourth term. This solution is equivalent to the solution given in equation (2.30) in case of a transducer thickness exceeding the optical penetration depth.
An explicit time-dependent stress with a finite stress rise time τ complicates the solution to equation (2.32). Assuming an exponential rising of the stress by $\sigma_3^{\mathrm{ext}}(t)\sim 1-e^{-\frac{t}{\tau}}$ leads to additional terms in equation (2.32). Using discrete time steps t_i this exponential stress rise transforms to $\sum_{t_i}\frac{(t_{i+1}-t_i)}{\tau}e^{-\frac{t_i}{\tau}}$ under the condition of $t_i-t_{i+1}\ll\tau$. This discrete picture simplifies the continuous time-dependent stress to a sum of stress fractions each of them driving dynamics according to equation (2.33) in case of $t=t-t_i>0$. This simple picture directly rationalises the condition $\tau\ll\frac{\xi}{v}$ or $\tau\ll\frac{d}{v}$ for negligible time dependence of the stress rise time concerning thick and thin films, respectively. This condition ensures a coherent superposition of the dynamics driven by the discrete stress fractions, since the decoherence time is given by the propagation of the strain wave on the length scale of its spatial extent (ξ or d).

In the following paragraphs I discuss the solution to the inhomogeneous wave equation for a transducer on a substrate in case of perfect impedance match and equal sound velocities according to equation (2.32) and (2.33) including a time-dependent stress.
Figure 2.3(a) depicts the spatio-temporal strain response for an instantaneous stress and a layer thickness of $d=0.5\,\xi$. The spatial slices in (b) display the generation of a bipolar strain wave that propagates into the substrate. The unbalanced expansive stress at the surface and the interface results in an expansion of the transducer that compresses the substrate at the interface. This compression is complemented to a bipolar strain wave by the bipolar strain pulse driven at the surface.

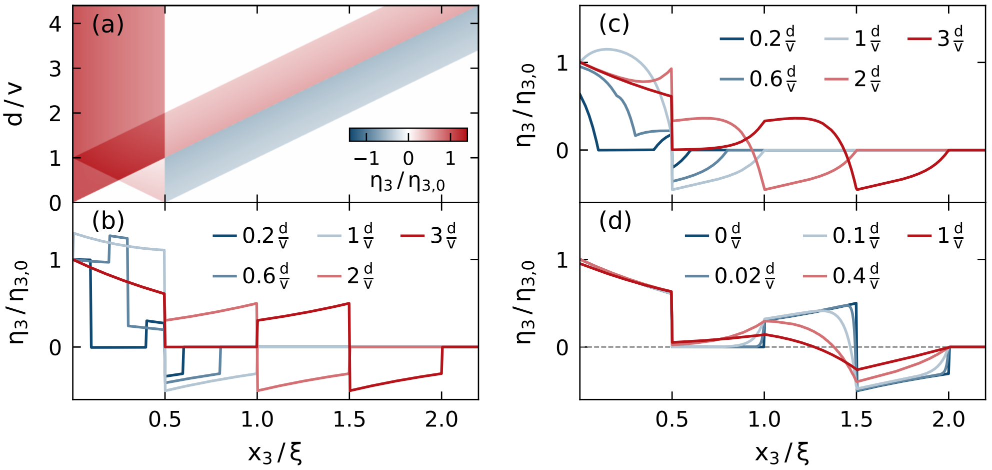

Figure 2.3: Strain dynamics driven by a spatio-temporal laser-induced stress for a perfect impedance-matched transducer-substrate system with $(d = 0.5\xi)$. Assuming instantaneous stress rise, panels (a) and (b) display the generation of a bipolar strain wave. The spatial intersections for different delays in units of $\frac{d}{v}$ identify both the surface and interface as strain source. The comparison to the spatial intersections for a finite stress rise time of $\tau = 0.1\frac{d}{v}$ in (c) reveals a significant change of the shape of the strain wave. This change is systematically depicted in (d) at delay $t = 3\frac{d}{v}$ for different stress rise times in units of $\frac{d}{v}$

The expansive part of the bipolar strain wave leaves the excited film at $t = \frac{d}{v}$. Therefore the transducer exclusively contains the expansive part of the bipolar strain wave that elevates the mean strain of the film to $3/2$ of the bare strain after $t = 2\frac{d}{v}$ [49].

The influence of a finite stress rise time τ is shown in figure 2.3(c) for a stress rise time of $\tau = 0.1\frac{d}{v}$ which contradicts the condition of negligible time dependence of the stress. The slowly increasing expansion at the surface $(x_3 = 0)$ with increasing delays indicates the finite stress rise time in comparison to figure 2.3(b). This finite stress rise time also changes the spatial shape and the amplitude of the driven bipolar strain wave. The finite rise time leads to a superposition of coherently excited phonons that are launched at different delays. The strain dynamics driven by delayed stress components cause a spatial broadening of both the expansive and compressive part of the strain wave according to the length scale given by $\tau \cdot v$. Therefore the smeared out compressive part overlaps with the expansive part and the superposition extends the effective compressive part as shown by the shifted zero-crossing in case of finite stress rise time (figure 2.3(d)). The comparison of the driven strain wave for different rise times τ in units of $\frac{d}{v}$ at a delay of $t = 3\frac{d}{v}$ in figure 2.3(d) displays a systematic trend with increasing stress rise time. A nearly unchanged strain wave is only observable for the smallest, finite rise time fulfilling $\tau \ll \frac{d}{v}$. However, with increasing stress rise time the amplitude of the coherent dynamics decreases due to the incoherent excitation conditions. Furthermore, the superposition of the spatially extended expansive and compressive part causes increasing spatial dimensions of both the compressive and expansive part.

The change of the driven bipolar strain wave also influences the temporal shape of the transient mean strain of the layers in a heterostructure as demonstrated in the supplementary material of [29]. Here, the mean strain of the detection layer indicates a nearly uni-polar strain wave for slow stress rise, since the spatial dimension of the expansive part exceeds the layer thickness causing an asymmetry in the detection. The observed stress dependence of the driven strain dynamics exemplifies the strain response to be characteristic for the spatio-temporal stress. This I use extensively in the analysis of the picosecond strain response in chapter 5 and 6.

CHAPTER THREE

USING GRÜNEISEN PARAMETERS TO MODEL ULTRAFAST STRESSES

In this chapter I discuss the linear relation between the energy density ρ^Q and the stress σ, which is central to the interpretation of the picosecond strain response observed by ultrafast X-ray diffraction in this thesis. The used thermodynamic concepts date back to the work of *E. Grüneisen* in 1912 [17] who studied the temperature-dependent thermal expansion of solids under equilibrium heating. The following sections present the core ideas of this approach and discuss its application in the modelling of laser-induced strain dynamics.

In the first section the potentially anisotropic (negative) thermal expansion is conceptually separated into the induction of a pressure at constant volume by a temperature increase and a subsequent relaxation of the pressure by a volume change according to the elastic properties. The temperature increase driving the thermal expansion relates to the deposition of an energy density by the corresponding heat capacity. In the second section the introduced Grüneisen parameter Γ linearly relates the deposited energy density to a stress as generalised pressure. The extension of this Grüneisen approach to the subsystems of electrons, phonons and magnetic excitations by subsystem-specific Grüneisen parameters enables the separation of the total stress into the individual subsystem contributions. The last section presents the two conceptual steps to model a laser-induced strain response. First, the application of the Grüneisen approach to the equilibration of the laser-induced non-equilibrium of the subsystems results in a thermodynamic model of the time-resolved stress. In a second step a linear-chain model of masses and springs calculates the picosecond strain response including coherently excited strain waves on the basis of the total time-dependent stress.

3.1 Thermodynamics of thermal expansion

This section focusses on the thermodynamic description of the potentially anisotropic (negative) thermal expansion of solids on the basis of previous investigations [15, 19, 50]. This description of the strain response in equilibrium prepares the introduction of the Grüneisen approach, which is the core of the analysis of the laser-induced strain dynamics in the following chapters.

Thermal expansion in general is caused by microscopic intra- and interatomic interactions changing the macroscopic properties of the solid. The thermodynamic description bases on the macroscopic properties and rationalises the behaviour of the solid without a detailed knowledge about the microscopic processes. In case of isotropic elastic properties and thermal stresses the expansion of a solid is characterised by the volumetric expansion coefficient

$$\beta = \frac{1}{V}\left.\frac{\partial V}{\partial T}\right|_p , \tag{3.1}$$

which describes the relative volume change $\Delta V/V$ induced by changing temperature T under constant pressure p. Here, the temperature-dependent volume minimises the Helmholtz free energy

F as thermodynamic potential [15, 19]. The differential of the free energy $F = U - TS$ is given by

$$\mathrm{d}F = -S\mathrm{d}T - p\mathrm{d}V \,, \tag{3.2}$$

wherein S denotes the entropy and U the internal energy. Using the free energy provides further insight into the physics of thermal expansion. The corresponding Maxwell relation based on the interchangeability of partial derivations $\left.\frac{\partial S}{\partial V}\right|_T = \frac{\partial}{\partial V}\left(\frac{\partial F}{\partial T}\right) = \frac{\partial}{\partial T}\left(\frac{\partial F}{\partial V}\right) = \left.\frac{\partial p}{\partial T}\right|_V$ can be used to transform the volumetric expansion to:

$$\beta = -\frac{1}{V}\left.\frac{\partial V}{\partial p}\right|_T \left.\frac{\partial p}{\partial T}\right|_V = \frac{1}{B}\left.\frac{\partial S}{\partial V}\right|_T \,. \tag{3.3}$$

Here, the isothermal bulk modulus B is defined by $B = -\left.\frac{\partial p}{\partial \ln V}\right|_T$ and describes the inverse compressibility of the solid, which determines the volume change as a response to an induced pressure. The first term in equation (3.3) separates the thermal expansion conceptually into two steps. First, a change in temperature induces a pressure at constant volume. This induced pressure stresses the solid and the following relaxation leads, in the second step, to the volume change determined by the elastic properties. This two-step view on thermal expansion is depicted in figure 3.1 by the blue arrows that indicate the underlying minimisation of the free energy F. The figure schematically displays the free energy in dependence of the volume for two temperatures T (gray solid line) and $T + \Delta T$ (black solid line). Here, the induced pressure with increased temperature is represented by the negative slope of the free energy $F(V)$ according to equation (3.2). Since the minimum of the free energy corresponds to $p = 0$, the second step in thermal expansion is associated with a relaxation of the temperature-induced pressure by a volume change, that results in an internal elastic stress counteracting the induced pressure.

Equation (3.3) indicates the important role of the entropy in the thermal expansion, the solid expands if the entropy increases with increasing volume but contracts if the entropy decreases with increasing volume. This observation is supported by the condition of minimised free energy with changing temperature that can be expanded to first order in temperature as [50]:

$$F(T + \Delta T, V) = F(T, V) - S(T, V)\Delta T \,. \tag{3.4}$$

Equation (3.4) shows the correspondence between minimisation of the free energy and the maximisation of the entropy. In case of a volume-dependent entropy the volume changes always in

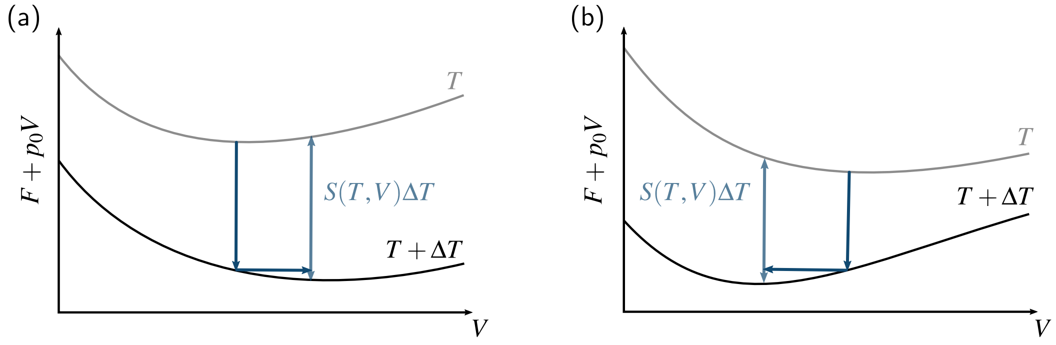

Figure 3.1: Thermodynamic two-step view on thermal expansion based on equation (3.3) and (3.4). The minimum of the volume-dependent Helmholtz free energy $F(T,V) + p_0V$ determines the equilibrium volume V of the solid. Increasing the temperature from T to $T + \Delta T$ shifts the position of the minimum in the first step and causes a volume change in the second step. In (a) the entropy increases with increasing volume ($\partial S/\partial V|_T > 0$) inducing an expansion. However, in (b) $\partial S/\partial V|_T < 0$ shifts the minimum of the free energy to smaller volumes inducing a negative thermal expansion (NTE).

the direction of increasing entropy, that is required by the second law of thermodynamic. The temperature-induced expansion due to a volume-dependent entropy is depicted in figure 3.1. The difference between the volume-dependent free energy at two temperatures relates by equation (3.4) to the volume-dependent entropy times the temperature change. The minimum position of the volume-dependent free energy $F(T,V)$ at temperatures T and $T+\Delta T$ differs, which leads to an expansion. Depending on the volume dependence of the entropy the expansion is either positive (a) or negative (b). The positive expansion corresponds to an increasing volume with increasing temperature, which is in agreement with the usual daily experience. The special case of negative thermal expansion (NTE) is shortly discussed in section 3.1.2.

3.1.1 Anisotropic expansion

In the previous paragraph the assumption of isotropic or cubic solids leads to an isotropic thermal expansion described by the volumetric expansion coefficient β. However, in general both anisotropic elastic properties and anisotropic microscopic stress mechanisms induce anisotropic thermal expansion. The description of anisotropic expansion requires a direction dependence of the temperature-induced pressure p and the relative volume change $\Delta V/V$. The generalised quantities are the external stress $\sigma_\lambda^{\text{ext}}$ and the strain η_λ, which were introduced in chapter 2 and determine the thermal expansion. Equation (3.3) demonstrates the relevance of the temperature-induced pressure for the volumetric expansion. In analogy, the anisotropic expansion is determined by the temperature-induced stress $\sigma_\lambda^{\text{ext}}$. Inserting the relation between stress and strain from the generalised Hooke's law (2.10) results in:

$$\left.\frac{\partial \sigma_\lambda^{\text{ext}}}{\partial T}\right|_\eta = \sum_{\mu=1}^{6} c_{\lambda\mu} \left.\frac{\partial \eta_\mu}{\partial T}\right|_\sigma = \sum_{\mu=1}^{6} c_{\lambda\mu}\alpha_\mu \tag{3.5}$$

where the elastic constants are assumed to be temperature-independent. The elastic constants $c_{\lambda\mu}$ in equation (3.5) relates the temperature-induced stress to the linear thermal expansion coefficient α_μ defined by

$$\alpha_\mu = \left.\frac{\partial \eta_\mu}{\partial T}\right|_\sigma , \tag{3.6}$$

which includes in general also shear strain $\eta_{\mu=4,5,6}$. Equation (3.5) is the general expression of equation (3.3) including anisotropic stress mechanisms and the full elastic tensor with 21 independent coefficients. The generalised ansiotropic case can be transferred to the special isotropic case by the assumption of both isotropic temperature-induced stress and the simplified elastic tensor of cubic symmetry (2.16):

$$\left.\frac{\partial p}{\partial T}\right|_V = \frac{c_{11}+2c_{12}}{3}\cdot 3\alpha \tag{3.7}$$

wherein $\alpha = \alpha_\lambda$ for $\lambda \in \{1,2,3\}$. Equation (3.7) uses the equal sign of pressure and stress in this thesis. This sign definition of the external pressure $\sigma_\lambda^{\text{ext}}$ in contrast to other publications [15, 19, 50] bases on the association of the external stress to counteract the restoring force of the internal stress. Thus positive external stress leads to an expansion (see section 2.1.2). In first order the volumetric expansion coefficient is determined by $\beta = 3\alpha$. Therefore the comparison of equation (3.3) and (3.7) reveals the representation of the bulk modulus by the elastic tensor in case of isotropic or cubic solids [47, p. 140]:

$$B = -\frac{\partial p}{\partial \ln V} = \frac{c_{11}+2c_{12}}{3} . \tag{3.8}$$

Introducing the compliance $s_{\lambda\mu}$ as generalised compressibility, equation (3.5) can be transformed to a definition of the anisotropic expansion coefficient α_μ. Using the reciprocal condition of the compliance and the elastic tensor

$$\sum_\nu c_{\lambda\nu} s_{\nu\mu} = \delta_{\lambda\mu} \tag{3.9}$$

equation (3.5) leads to a relation between the linear thermal expansion α_μ and the direction-dependent external stresses $\sigma_\lambda^{\text{ext}}$ [19]:

$$\alpha_\mu = \sum_{\lambda=1}^{6} s_{\mu\lambda} \left.\frac{\partial \sigma_\lambda^{\text{ext}}}{\partial T}\right|_\eta . \tag{3.10}$$

The stress as generalised pressure is related to the free energy by the derivative $\sigma_\lambda = -\frac{1}{V}\left.\frac{\partial F}{\partial \eta_\lambda}\right|_{\eta',T}$. The subscript η' denotes that all strain coordinates except η_λ are kept constant. Inserting this and using the relation $S = -\frac{\partial F}{\partial T}$ results in:

$$\alpha_\mu = \frac{1}{V}\sum_{\lambda=1}^{6} s_{\mu\lambda} \left.\frac{\partial S}{\partial \eta_\lambda}\right|_{\eta',T} . \tag{3.11}$$

Equations (3.10) and (3.11) indicate the contribution of different stress components to the thermal expansion α_μ. The stress components $\sigma_{\lambda\neq\mu}$ couple to the expansion α_μ via the off-diagonal elements of the compliance tensor that correspond to the Poisson effect. Even if these stress components vanish ($\sigma_{\lambda\neq\mu} = 0$), the thermal expansion includes the Poisson effect as shown by equation (2.18). Thus thermal expansion under equilibrium conditions does not directly correspond to the intrinsic expansion given by the associated external stress components, but also includes the Poisson effect as additional internal stress originating from the transverse strains.

3.1.2 Negative thermal expansion

Under equilibrium conditions at low temperatures both materials investigated in this thesis, $SrRuO_3$ and dysprosium, show a decreasing lattice spacing with increasing temperature thus negative thermal expansion [24, 25]. Therefore this section provides an overview about this phenomenon in various materials induced by different mechanisms, which shares an increasing entropy with decreasing volume [15, 51, 52]. The most familiar example of the resulting negative thermal expansion is the density anomaly of water between 0 and 4°C.

In statistical physics the number of microstates corresponding to the same macrostate determines the entropy. In case of an ideal gas the number of microstates representing the same macrostate increases with increasing volume and thus the entropy increases [53, p. 129]. The maximisation of the entropy in thermal equilibrium results in a positive thermal expansion. A simple example of decreasing entropy with enhanced volume from statistical physics is a one-dimensional polymer chain of free-orientable subunits. The longer the polymer chain is the more subunits have to be orientated parallel to the direction of the chain reducing the number of microstates leading to the same polymer chain length. This example in comparison to the ideal gas highlights the important role of interatomic interactions in negative thermal expansion.

In a solid, the crystal structure results from the interaction between the individual atoms that it hosts. It determines the band structure of electrons and the dispersion relation of phonons including macroscopic phenomena like ferroelectricity and magnetism. The excitation of these quasi-particles and collective phenomena can lead to negative thermal expansion, which occurs in various materials. The following paragraphs provide a brief overview of the different mechanisms leading to negative thermal expansion in various materials.

The so called tension effect [52, 54] induces negative thermal expansion by transverse phonons (see figure 3.2). The transverse oscillation of the atoms stresses the interatomic bound (gray dashed line), which results in an additional restoring force (blue arrow). In open structures like zinc blende or wurtzite the favourable excitation of transverse phonons induces a negative thermal expansion for example in Si, Ge, GaAs, InAs, HgTe or CdTe [19, 52, 55, 56] at low temperatures. In trigonal selenium [57] and tellurium [58] this vibrational effect induces an anisotropic negative thermal expansion over a wide temperature range. One famous example of isotropic negative thermal expansion over a wide temperature range is zirconium tungstate ZrW_2O_8 [59].

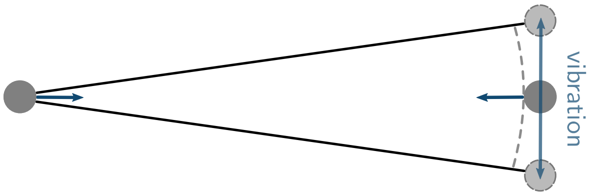

Figure 3.2: Tension effect in two dimensions. Transverse oscillations induce an additional restoring force by stressing the interatomic bond that decreases the effective lattice spacing (dashed gray line).

In general, also strictly positive external stress can induce anisotropic negative thermal expansion. The conditions are a strongly anisotropic stress and large off-diagonal elements of the elastic tensor. According to equation (2.13) the strain component η_λ is reduced by a negative elastic stress generated by other strain components $\eta_{\mu\neq\lambda}$ via the off-diagonal elements of the elastic tensor. Therefore strongly anisotropic induced stress and large off-diagonal elements may induce an effective negative stress. This strong anisotropic stress can be either temperature-induced as in arsenic, indium, zinc and cadmium [60, 61] or induced by the different in-plane expansion of the substrate deforming the unit cells of a thin film that is epitaxially attached to it.

Furthermore, ferroelectric materials like the perovskites $PbTiO_3$ [62] and $BaTiO_3$ [63] exhibit a volumetric negative thermal expansion in the tetragonal phase below their order temperature. Also magnetism induces anisotropic negative thermal expansion for example in rare-earth materials [24, 51] or the perovskite $SrRuO_3$ [25]. Even crystal electrons can cause negative thermal expansion as observed for strontium [64] at low temperatures.

3.2 The Grüneisen model

In the previous section the thermal expansion is conceptually separated into two steps. These are the generation of lattice stress by a temperature change and the following relaxation of the stress by a change of the solids dimensions. While the second step is determined by the elastic properties of the solid, the first step contains the stress generation from an increased entropy that results from an energy density deposition. This section introduces the concept of the Grüneisen parameter Γ as the linkage between energy density ρ^Q and stress σ for phonons, electrons and magnetic excitations. Starting from equilibrium considerations this concept is extended to describe the laser-induced stress on ultrafast timescales with non-thermal distribution functions.

The following paragraphs consider the thermodynamic relations for a heated solid that lead to the definition of the Grüneisen parameter Γ. The temperature increase inducing a deformation of the solid requires the deposition of energy per unit volume at constant volume $\rho^Q = \frac{U}{V}$. In the isochoric case the total differential of the internal energy $\mathrm{d}U = \delta Q + p\mathrm{d}V$ reduces to [53, p. 122]:

$$\frac{\mathrm{d}U}{V} = \frac{\delta Q}{V} = \frac{C_V}{V}\mathrm{d}T\,, \tag{3.12}$$

where C_V denotes the heat capacity at constant volume. This relates the temperature-induced pressure in equation (3.3) to the deposited internal energy U per unit volume [15, 16]:

$$\left.\frac{\partial p}{\partial T}\right|_V = \frac{C_V}{V}\left.\frac{\partial p}{\partial \frac{U}{V}}\right|_V = \frac{C_V}{V}\Gamma\,. \tag{3.13}$$

Here, the Grüneisen parameter defines the induced pressure by energy density deposition, which corresponds to the first conceptual step in the thermal expansion process. Inserting the definition of the temperature-induced pressure in equation (3.3) relates the Grüneisen parameter Γ to the macroscopic properties of the solid, i.e. the volumetric thermal expansion β, the bulk modulus B and the heat capacity C_V:

$$\Gamma = \left.\frac{\partial p}{\partial \frac{U}{V}}\right|_V = BV\frac{\beta(T)}{C_V(T)} . \tag{3.14}$$

According to equation (3.14) the volumetric expansion coefficient β is fully described by the bulk modulus, the heat capacity and the Grüneisen parameter. In analogy to section 3.1.2 this definition of the Grüneisen parameter can be generalised for the case of anisotropic expansion. The anisotropic Grüneisen parameter Γ_λ relates the scalar quantity of deposited energy density ρ^Q to the direction-dependent stress σ_λ. The description of anisotropic expansion in equation (3.5) transforms equation (3.14) to:

$$\Gamma_\lambda = \sum_{\mu=1}^{6} c_{\lambda\mu} V \frac{\alpha_\mu(T)}{C_V(T)} . \tag{3.15}$$

The relation between the linear thermal expansion α_μ and the temperature-induced external stress (3.10) transforms the anisotropic Grüneisen parameter (3.15) to:

$$\Gamma_\lambda = \frac{V}{C_V} \left.\frac{\partial \sigma_\lambda^{\text{ext}}}{\partial T}\right|_\eta . \tag{3.16}$$

For sufficiently small temperature changes dT equation (3.16) simplifies and reveals the Grüneisen parameter relating linearly energy density and induced stress:

$$\sigma_\lambda^{\text{ext}} = \Gamma_\lambda \rho^Q = c_{\lambda\lambda}\eta_\lambda^c = c_{\lambda\lambda}\left(\eta_\lambda + \sum_{\mu\neq\lambda}\frac{c_{\lambda\mu}}{c_{\lambda\lambda}}\eta_\mu\right) . \tag{3.17}$$

The induced stress $\sigma_\lambda^{\text{ext}}$ relates by the elastic tensor element $c_{\lambda\lambda}$ to a strain η_λ^c that corresponds to the new equilibrium position. The superscript c indicates vanishing strain components $\eta_{\mu\neq\lambda} = 0$. The resulting simple relation between stress and strain is rationalised by neglecting the transverse strain components $\eta_{\mu\neq\lambda}$ in equations (2.13) and (3.5). Thus clamping all strain components except η_λ as on ultrafast timescales in a thin film geometry accesses the intrinsic expansion without Poisson effect given by the anisotropic Grüneisen parameter Γ_λ.

Historically, the Grüneisen parameter was introduced by *E. Grüneisen*, who observed heat capacity and thermal expansion share the same temperature dependence in various materials [17]. Since the elastic constants typically vary very little with temperature [16], this leads to a temperature-independent Grüneisen constant according to equation (3.14). In fact, for many materials the Grüneisen parameter is approximately temperature-independent and therefore a Grüneisen constant as for the closed-packed metals aluminium, copper, iron, gold, platinum and silver [65–68] or the insulator magnesium oxide [69]. In this case a deposited energy density induces the same external stress regardless of the sample temperature.

However, in general the Grüneisen parameter of a solid is temperature-dependent. The Grüneisen parameter changes especially at low temperatures, where mainly phonon modes of low energy are occupied [19, 70] (section 3.2.1) or other subsystems r like magnetic excitations (section 3.2.3) add to the phonon contribution [71, 72]. Therefore it is useful to separate the Grüneisen parameter into its subsystem contributions Γ_r weighted by the respective heat capacity [19, 71]:

$$C_V\Gamma = \sum_r \Gamma_r C_r . \tag{3.18}$$

The Grüneisen parameter Γ_r of each subsystem r describes the lattice stress generated by the deposition of energy density ρ_r^Q to the subsystem. Equation (3.18) clearly indicates a temperature-dependent total Grüneisen parameter Γ if the heat capacity contributions of the subsystems with subsystem-specific Grüneisen parameters exhibit a different temperature dependence.

The volume dependence of the entropy offers further insight into the origin of the lattice stress of different subsystems. The total differential of the entropy $S(T,V)$ in equation (3.19) reveals an alternative approach to define the Grüneisen parameter.

$$\begin{aligned} \mathrm{d}S &= \left.\frac{\partial S}{\partial T}\right|_V \mathrm{d}T + \left.\frac{\partial S}{\partial V}\right|_T \mathrm{d}V \\ &= \frac{C_V}{T}\mathrm{d}T + \frac{B\beta V}{V}\mathrm{d}V \end{aligned} \tag{3.19}$$

The partial derivatives of the entropy are associated with the macroscopic properties of the solid by using the second law of thermodynamics [53, p. 127f] $\left(\mathrm{d}S|_V = \frac{\mathrm{d}U}{T}|_V\right)$ and the definition of the volumetric thermal expansion (3.3). As discussed in equation (3.4) and in figure 3.1 the minimisation of the free energy corresponds to a maximisation of the entropy ($\mathrm{d}S = 0$). Thus equation (3.19) relates the Grüneisen parameter to the negative relative temperature change with changing volume:

$$\Gamma = BV\frac{\beta(T)}{C_V(T)} = -\frac{\mathrm{d}\ln T}{\mathrm{d}\ln V} \tag{3.20}$$

Associating the entropy to depend on the occupation of quasi-particle states makes this unconventional definition of the Grüneisen parameter useful. It shows that the Grüneisen parameter describes the volume dependence of the energy of quasi particle states [19], where the temperature determines the occupation via the relevant distribution function. This thesis investigates magnetic metals where the relevant subsystems r are electrons, phonons and magnetic excitations. The entropy of these subsystems depends on the density of states at the Fermi surface [18, 73, 74], the Debye temperature [50, 73, 74] and the magnetic exchange energy [18, 50, 74]. The corresponding Grüneisen parameters and thermal expansion due to electronic excitations, phonons and magnetic excitations are discussed in the following sections.

3.2.1 Phonon Grüneisen parameter

Historically, the Grüneisen description of thermal expansion only includes the phonons [17]. In non-magnetic metals in thermal equilibrium this is, especially at room temperature, a valid simplification, since the electronic heat capacity is small compared to the phononic one. Therefore the total Grüneisen parameter approximately coincides with the Grüneisen parameter of the phonons independently of the electronic Grüneisen parameter (see equation (3.18)). According to equation (3.14) the phononic Grüneisen parameter is determined by the phononic heat capacity contribution and the phonon caused pressure that both results from the internal energy U. The internal energy is determined by the sum of the equilibrium internal energy U^{eq} and the contributions from the phonons as quantised harmonic lattice vibration modes [46, p. 489f]:

$$U = U^{\mathrm{eq}} + \sum_{ks}\left(n_{ks} + \frac{1}{2}\right)\hbar\omega_s(k) \tag{3.21}$$

wherein $n_{ks} = \left(e^{\vartheta\hbar\omega_s(k)} - 1\right)^{-1}$ denotes the occupation of the state with frequency $\omega_s(k)$, wave vector k and polarisation s according to the Bose-Einstein-statistic at temperature $T = (k_\mathrm{B}\vartheta)^{-1}$. Thus the internal energy of the phonons inherits the temperature dependence of the distribution function. In the following I use the temperature-dependent internal energy to determine the phononic heat capacity contribution and the volumetric expansion.

The heat capacity at constant volume C_{ph} of the phonons as lattice vibration quanta is determined by the temperature-induced occupation change of the modes:

$$C_{\mathrm{ph}} = \left(\frac{\partial U}{\partial T}\right)_V = \sum_{ks} \hbar\omega_s(k) \frac{\partial}{\partial T} n_{ks} \,. \tag{3.22}$$

In the simple case of isotropic or cubic solids the temperature-induced pressure describes the volumetric expansion β (3.3). The free energy $F = U - TS$ defines the pressure by $p = -\left.\partial F/\partial V\right|_T$. Using the relation between entropy and internal energy $\left.\frac{\partial S}{\partial T}\right|_V = T\left.\frac{\partial U}{\partial T}\right|_V$ relates the pressure to the internal energy (3.21) [46, p. 489f]. This definition of the pressure originating from the phonons determines the volumetric expansion according to equation (3.3)*

$$\beta = \frac{1}{B} \sum_{ks} \hbar \left(-\frac{\partial}{\partial V}\omega_s(k)\right) \frac{\partial}{\partial T} n_{ks} \,. \tag{3.23}$$

The comparison of the heat capacity C_{ph} (3.22) to the volumetric expansion β (3.23) demonstrates the identical temperature dependence defined by the occupation change of the modes with temperature. Therefore the ratio of those quantities defines a temperature-independent mode-specific Grüneisen constant as historically suggested by *E. Grüneisen*:

$$\gamma_{ks} = \frac{VB\beta_{ks}}{C_{ph,s}(k)} = -\frac{\partial \ln \omega_s(k)}{\partial \ln V} \,. \tag{3.24}$$

The mode-specific Grüneisen constant describes the volume dependence of the energy of quantum mechanical states. Furthermore, it highlights the thermal expansion being an anharmonic effect, since the excitation level of an harmonic oscillator does neither change its equilibrium position nor its resonance frequency. Figure 3.3 depicts an anharmonic potential (black solid line) and the change of the equilibrium position (blue dots) with occupation of higher energetic vibrational states in contrast to a strictly harmonic potential (gray solid line). In non-cubic solids the phononic stress may be anisotropic and the corresponding mode-specific Grüneisen constant $\gamma_{k,s,\lambda}$ corresponds to an anisotropic anharmonicity of the interatomic potential [19]:

$$\gamma_{k,s,\lambda} = -\frac{\partial \ln \omega_s(k)}{\partial \eta_\lambda} \,. \tag{3.25}$$

Anisotropic thermal expansion and the corresponding anisotropic phononic Grüneisen parameter is reported for various trigonal, hexagonal and orthorhombic materials. For an overview see [75, p. 91ff], [16, p. 243] and [19, 60, 61]. As discussed in section 3.1.2 an exclusively positive but anisotropic Grüneisen parameter may cause a negative thermal expansion in one direction via the Poisson effect that induces an additional contractive stress.

The mode-specific Grüneisen constants γ_{ks} define a macroscopic Grüneisen parameter of the phonons Γ_{ph} as the heat capacity contribution weighted mean value of the γ_{ks}:

$$\Gamma_{\lambda,\mathrm{ph}} = \frac{\sum_{ks} \gamma_{\lambda ks} C_{V,s}(k)}{\sum_{ks} C_{V,s}(k)} = -\frac{\partial \ln \omega_D}{\partial \eta_\lambda} \,. \tag{3.26}$$

In the frequently used Debye model the frequency of the normal vibration modes scales linearly with the Debye frequency ω_D. This is due to the assumption of a linear dispersion relation and a

---

*Note, the contradiction between a volume dependence of the phonon frequencies and the treatment of harmonic vibrations in the internal energy is called quasi-harmonic approximation [19]. This is an approximation since, the frequency of a purely harmonic oscillator is volume-independent and the vibrational energy of an anharmonic oscillator includes higher orders in the atomic displacement.

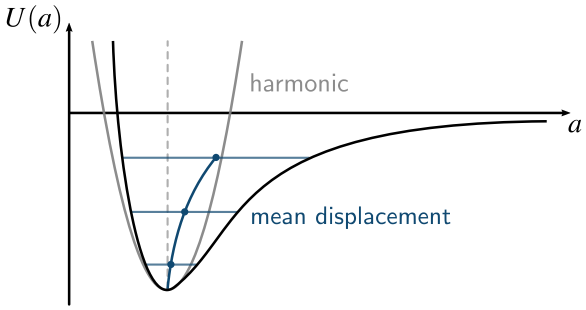

Figure 3.3: Comparison of a strictly harmonic (gray) and an anharmonic interatomic potential (black). The anharmonic potential induces a difference in repulsive and attractive forces leading to a finite mean displacement (blue dots) with occupation of higher vibrational states (light blue lines).

homogeneous distribution of the modes in reciprocal space. Thus all modes exhibits the same Grüneisen constant and the total Grüneisen parameter Γ_{ph} is strictly temperature-independent and related to the negative strain dependence of the Debye frequency [46, p. 491].
However, in real solids not all modes exhibit the same Grüneisen constant. Therefore the total Grüneisen parameter inherits the temperature dependence of the mode contribution to the total heat capacity. At low temperatures low-frequency phonon modes are mainly occupied and their Grüneisen constant determines the total Grüneisen parameter. The resulting temperature-dependent thermal expansion in equilibrium can be calculated by determining the mode specific Grüneisen constants by an anharmonic interatomic potential in the crystal structure [70, 76–78]. Since the Debye temperature Θ_{D} corresponds to the temperature leading to an occupation of all phonon modes, the macroscopic Grüneisen parameter typically changes well below the Debye temperature ($\sim 0.5\Theta_{\text{D}}$) [79]. In open structures like zinc blende or wurtzite the transverse phonons have low frequencies and are therefore energetically favourable. Since transverse phonon modes potentially exhibit a negative Grüneisen constant via the tension effect (see figure 3.2), it is common that in these solids the total Grüneisen parameter is strongly temperature-dependent and in some materials even negative at low temperatures (see section 3.1.2). Furthermore, high-frequency optical phonons with a different mode-specific Grüneisen constant can vary the Grüneisen parameter at high temperatures near the Debye temperature. For example in rutile (TiO_2) the optical phonon modes exhibit a significant smaller Grüneisen constant, therefore their occupation at high temperatures reduces the macroscopic Grüneisen parameter [80] according to equation (3.26).

$$\sigma_{\text{ph}} = \frac{1}{V}\sum_{ks}\gamma_{ks}\hbar\omega_S(k)\delta n_{ks} \tag{3.27}$$

From a microscopic perspective this translates the lattice stress induced by phonons to be dependent on the occupation of these modes. From this microscopic perspective the deposition of energy leads to an occupation change of different modes δn_{ks}. Thus the deposited energy density reads $\rho^Q = \frac{1}{V}\sum_{ks}\hbar\omega_S(k)\delta n_{ks}$. In analogy to the general definition of the Grüneisen parameter (3.17) the energy density per mode $\rho^Q_{ks} = \frac{1}{V}\hbar\omega_S(k)\delta n_{ks}$ times the mode-specific Grüneisen parameter γ_{ks} defines the resulting lattice stress [31]. The formulation of the phonon stress in equation (3.27) is also valid in strongly non-equilibrium situations that occur upon laser-pulse excitation.

3.2.2 Electron Grüneisen parameter

In solids the electrons together with the nuclei determine the crystal structure and interatomic potentials. Therefore a changing occupation of electronic states also induces a lattice stress by influencing the interatomic potentials. However, in non-magnetic metals at room temperature the anharmonic phonon-phonon interactions dominate the equilibrium thermal expansion, due to the negligible electronic specific heat. In equilibrium most of the energy density is deposited in the phonon subsystem and the phononic Grüneisen parameter therefore determines the thermal expansion according to equation (3.18). In equilibrium the electronic stress contribution only becomes significant at low temperatures, where the electronic heat capacity $C_{\text{el}} \sim T$ becomes comparable to the phononic specific heat $C_{\mathrm{ph}} \sim T^3$. Since the Grüneisen parameter linearly relates the energy density to the lattice stress, the electron contribution to the volumetric expansion manifests as a term linear in temperature [64]. Additionally, in non-equilibrium situations after the excitation by ultrashort laser pulses the electronic stress contribution may be separable as demonstrated for gold, aluminium, nickel and copper [6, 9–11, 81–84] in X-ray diffraction and all-optical experiments. Since the pump pulse in the visible range excites exclusively the electrons, their stress contribution significantly influences the generated picosecond strain pulse, which provides access to the electronic Grüneisen parameter.

Equation (3.4) demonstrates the important role of entropy for thermal expansion minimising the free energy. In regards to the simple Sommerfeld model for a free electron gas the entropy depends on the density of states at the Fermi energy $n(E_{\mathrm{F}})$ and on the temperature T smearing out the Fermi edge that enables the changing occupation of electronic states [19]:

$$S_{\mathrm{el}} = \frac{2}{3}\pi^2 k_{\mathrm{B}}^2 T n(E_{\mathrm{F}}) = C_{\mathrm{el}} \,. \tag{3.28}$$

Equation (3.19) relates the volume dependence of the entropy $\partial S/\partial V|_T$ to the product of heat capacity C_V and Grüneisen parameter Γ per volume V. Thus the electronic entropy (3.28) defines the electronic Grüneisen Γ_{el} to:

$$\Gamma_{\mathrm{el}} = \left.\frac{\partial \ln n(E_{\mathrm{F}})}{\partial \ln V}\right|_T \,. \tag{3.29}$$

This formulation of the electronic Grüneisen parameter is generalised for anisotropic non-cubic solids by a direction dependence as in magnesium [85] and iron-platinum [31]:

$$\Gamma_{\lambda,\mathrm{el}} = \left.\frac{\partial \ln n(E_{\mathrm{F}})}{\partial \eta_\lambda}\right|_{T,\eta'} \,. \tag{3.30}$$

In case of free electrons described by the Sommerfeld model the density of states at Fermi energy is proportional to $V^{\frac{2}{3}}$. Inserting this dependence in equation (3.29) or (3.30) results in $\Gamma_{\mathrm{el}} = \frac{2}{3}$ independent of the direction. However, the electronic Grüneisen parameter of most of the metals is between $\Gamma_{\mathrm{el}} = 1$ and $\Gamma_{\mathrm{el}} = 3$ and therefore differs significantly from this free electron value. For an overview see [19], [16, p. 230] and [75, p. 70]. The band structure of a real solid with overlapping bands contradicts the single band assumption of the Sommerfeld model and causes peaks in the density of states enhancing its volume dependence at the Fermi energy.

In analogy to the phonons the lattice spacing dependence of the electronic states defines a state-specific Grüneisen constant

$$\gamma_{\lambda,i,k} = \frac{\partial \ln E_{i,k}}{\partial \eta_\lambda} \tag{3.31}$$

where $E_{i,k}$ denotes the energy of the electronic state with wavevector k and electronic band index i. The microscopic stress of the electronic subsystem is in analogy to equation (3.27) given by the occupation change δn_k and the state specific Grüneisen constant $\gamma_{\lambda,i,k}$ [3]:

$$\sigma_{\mathrm{el}} = \sum_k \gamma_{k,\mathrm{el}} E_{i,k} \delta n_k \,. \tag{3.32}$$

The dependence of the electronic state on the lattice spacing is also known as deformation potential, that is often introduced in the context of semiconductors [86, p. 122ff]. The deformation potential describes a change of the electronic band structure with changing interatomic distances, which corresponds to changing interatomic potentials. The Grüneisen constant captures the inverse process, i.e. the rise of a lattice stress by changing the occupation of electronic states.

In most materials, the electronic Grüneisen parameter is strictly positive and therefore induces an expansion, except for strontium [68], barium [68], manganese [18] and chromium [87]. However, the negative thermal expansion proportional to the temperature in chromium and manganese is assumed to correspond to a magnetic contribution that arises from the magnetic order.

3.2.3 Magnetic Grüneisen parameter

The previous sections exemplify the description of thermal expansion of non-magnetic metals by electronic and phononic Grüneisen parameters. In magnetic metals the magnetic order provides an additional energy reservoir and entropy source. Therefore the magnetic excitations influence the thermal expansion both in equilibrium [24, 25, 88–95] and on ultrashort timescales [26–31, 35, 36] for ferro- and antiferromagnetic coupling in various materials like $3d$-transition metals or rare-earth materials. This coupling of the magnetism to the lattice is called magnetostriction, which is divided into the spontaneous (thermal) and forced (magnetic field) magnetostriction [96, p. 174f][21–23]. This section focuses on the spontaneous magnetostriction, which can be linked to a magnetic Grüneisen parameter denoting the stress generation by magnetic excitations.

The strength of the magnetic order can be characterised by the parameter $\frac{J(r)}{k_\mathrm{B}T}$, where $J(r)$ denotes the exchange interaction parameter and $k_\mathrm{B}T$ the thermal energy. Therefore the entropy depends on the exchange interaction parameter, which depends intrinsically on the interatomic distances by the overlap of the electronic wave functions [96, p. 149]. In analogy to equation (3.20) the magnetic Grüneisen parameter is given by [18, 33, 34, 97]:

$$\Gamma_\mathrm{mag} = -\frac{\partial \ln J}{\partial \ln V} = -\frac{\partial \ln T_\theta}{\partial \ln V} \,. \tag{3.33}$$

Here, T_θ denotes the ferro- or antiferromagnetic order temperature corresponding to the exchange interaction strength, thus the Curie temperature T_C or the Néel temperature T_N. This order temperature denotes the vanishing of the long range magnetic order that corresponds to a vanishing heat capacity. This full demagnetisation introduces an intrinsic saturability of the magnetic stress. Since the exchange interaction parameter determines the frequencies of the magnons, the magnetic Grüneisen constant can be associated with the volume dependence of the magnon states [33]. In analogy to the Grüneisen parameter of phonons and electrons the magnetic Grüneisen parameter may also be anisotropic via the lattice spacing dependence of the exchange interaction along different crystal directions

$$\Gamma_{\lambda,\mathrm{mag}} = -\frac{\partial \ln J}{\partial \eta_\lambda} \,. \tag{3.34}$$

As discussed in section 3.1 the lattice constant in equilibrium corresponds to the minimisation of the free energy. In the Heisenberg model the Hamilton operator H relates to the dot product of neighbouring magnetic moments $\vec{S}_i$ and $\vec{S}_j$ and the exchange interaction parameter via $H = -J\sum_{i,j}\vec{S}_i\cdot\vec{S}_j$. With increasing temperature the minimisation of the free energy corresponds to a maximisation of the entropy (see equation 3.4). Since an enhanced exchange strength stabilises the magnetic order, the number of micro states leading to the same macro state and therefore the entropy increases with decreasing exchange interaction strength. In the case of a volume-dependent exchange interaction the excitation of the magnetic subsystem results in a lattice stress by the so-called exchange-striction mechanism [21, 22]. Therefore an increasing exchange strength with increasing interatomic distances ($\frac{\partial \ln J}{\partial \ln \eta_\lambda} > 0$) induces a contraction of the solid by maximising the entropy. This is in agreement with the associated negative magnetic Grüneisen parameter, which relates a deposited energy density to a contractive lattice stress.

The strain response caused by magnetic excitations shows large variations. It can be isotropic [88–91, 95] or anisotropic [24, 25, 72, 93] and expansive (nickel [34, 88], titanomagnetites [98] and cobalt [34]) or contractive (iron [34], chromium [34], strontium ruthenat [25] and dysprosium [24]). In most of the magnetic materials the lattice stress originating from the magnetism is only a small correction to the phonon stress due to small Grüneisen parameter and heat capacity contribution. Therefore in some ultrafast experiments the magnetic stress contribution is even neglected in the interpretation of lattice dynamics [10, 99, 100]. In contrast, the magnetic stress dominates the lattice dynamics in rare-earth metals like holmium and dysprosium [28, 29].

The magnetic Grüneisen parameter can be determined directly via the pressure dependence of the order temperature T_θ [98] or via the separation of the heat capacity C_V and the thermal expansion α_λ into the subsystem contributions [27–29, 34, 74] according to equation (3.17) and (3.18). This subsystem separation is based on a model of the electronic and phononic heat capacity and thermal expansion as discussed in detail for SrRuO$_3$ in chapter 5 and dysprosium in chapter 6.

3.3 Grüneisen perspective on laser excitation of thin films

The Grüneisen model enables the investigation of the influence of the magnetic stress on the picosecond strain by the separation of the time-dependent stress into the subsystem contributions. In this section I present both the modelling of the ultrafast stress $\sigma_\lambda^\mathrm{ext}$ by subsystem-specific Grüneisen constants $\Gamma_{\lambda,r}$ and the simulation of the corresponding strain response by a linear-chain model of masses and springs. The first section discusses the limitations of a Grüneisen constant for each subsystem under non-equilibrium conditions after the laser excitation. In the second section I present briefly the main ingredients of the linear-chain model of masses and springs that I use to translate the modelled spatio-temporal stress to a picosecond strain response.

A laser pulse in the visible range exclusively interacts with the electrons and causes intra- and interband transitions. Right after the ultrashort laser pulse excitation the absorbed energy density ρ^Q_abs is exclusively stored in the electronic system and the subsystems are in non-equilibrium. Subsequently, the subsystems equilibrate by transferring energy (density) between the subsystems via their coupling mechanisms. Thus the energy density $\rho^Q_r(t)$ stored in the different subsystems r is not only potentially different as in equilibrium but also strongly time-dependent if the coupling timescales exceed the duration of the laser pulse. The coupling of the subsystems during equilibration after the laser-induced non-equilibrium is sketched in figure 3.4. Due to the lack of insight which modes and states are occupied during the relaxation of the subsystems, the subsystems Grüneisen parameters Γ_r are in first order simplified to a macroscopic Grüneisen constant that is strictly independent of the excited quantum states. The subsystem-specific Grüneisen constants relate the time-dependent excitation of the subsystems to stress contributions under the boundary condition of energy conservation. The time-dependent stress contributions add up to the total lattice stress $\sigma^\mathrm{ext}(t)$, which drives the strain dynamics according to the inhomogeneous wave equation (2.26). Since the driven strain wave depends on the temporal stress profile (see section 2.2.2), detecting the strain dynamics provides access to the subsystem coupling timescales and stress mechanisms in case of different Grüneisen constants. The total lattice stress after the laser pulse excitation of a magnetic metal reads:

$$\sigma^\mathrm{ext}(t) = \Gamma_\mathrm{el}\cdot\left(\rho^Q_\mathrm{abs}-\rho^Q_\mathrm{ph}(t)-\rho^Q_\mathrm{mag}(t)\right)+\Gamma_\mathrm{ph}\cdot\rho^Q_\mathrm{ph}(t)+\Gamma_\mathrm{mag}\cdot\rho^Q_\mathrm{mag}(t)\,. \tag{3.35}$$

After the equilibration of the subsystems, their heat capacities determine the deposited energy density in each subsystem in the static limit. The corresponding total lattice stress $\sigma^\mathrm{ext}(t\rightarrow\infty)$) is then given by:

$$\sigma^\mathrm{ext}(t\rightarrow\infty) = \Gamma_\mathrm{el}\int_T^{T'}\frac{C_\mathrm{el}(T'')}{V}\mathrm{d}T''+\Gamma_\mathrm{ph}\int_T^{T'}\frac{C_\mathrm{ph}(T'')}{V}\mathrm{d}T''+\Gamma_\mathrm{mag}\int_T^{T'}\frac{C_\mathrm{mag}(T'')}{V}\mathrm{d}T''\,. \tag{3.36}$$

The difference between the temperatures T' and T denotes the laser-induced temperature increase. This temperature increase results from the distribution of the deposited energy density ρ^Q_dep into all subsystems according to their summed specific heat capacity C_tot:

$$\rho^Q_\mathrm{dep} = \int_T^{T'}\frac{C_\mathrm{tot}(T'')}{V}\mathrm{d}T'' \tag{3.37}$$

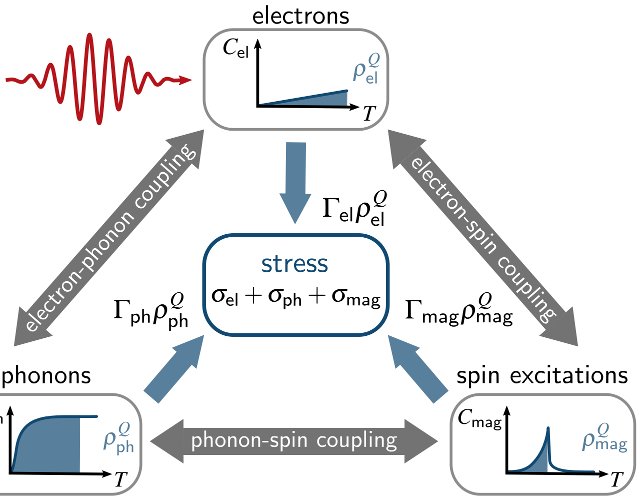

Figure 3.4: Sketch of the coupling of electrons, phonons and spins in a magnetic metal and their subsystem contribution to the total lattice stress σ. The laser pulse excitation exclusively deposits energy density ρ^Q_{dep} in the electronic system that is subsequently distributed to phonons and magnetic excitations. The subsystem coupling mechanisms corresponds to material-specific time constants determining the time-dependent energy density $\rho^Q_r(t)$ stored in each subsystem r. This energy density induces a time-dependent stress contribution via the subsystem-specific Grüneisen constant Γ_r and these contributions add up to the total lattice stress driving the strain response according to the inhomogeneous wave equation (2.25).

Equation (3.35) except for the magnetic term is commonly used to describe the lattice dynamics of non-magnetic metals [6, 9, 11, 81–84, 99, 101, 102], where the phonon stress rises with $1-e^{-t/\tau_{\mathrm{el\text{-}ph}}}$ due to the energy density transfer from the electrons to the phonons during the equilibration of the subsystems. The exponential temporal dependence of the energy transfer characterised by the timescale $\tau_{\mathrm{el\text{-}ph}}$ results from the two-temperature model introduced by *Anisimov and co-workers* [103]. The material-specific electron-phonon coupling time constant $\tau_{\mathrm{el\text{-}ph}}$ depends on the temperature-independent electronic and phononic heat capacity and the electron-phonon coupling parameter $g_{\mathrm{el\text{-}ph}}$ [48, p. 5f] and ranges between hundreds of femtoseconds in nickel or aluminium [9, 10] to several picoseconds in gold [11].

In magnetic materials the two-temperature model is extended by including the magnetic system. The additional heat bath modifies the energy transfer rate between electrons and phonons [104] by its additional coupling channels to the electrons $\tau_{\mathrm{el\text{-}mag}}$ and the phonons $\tau_{\mathrm{ph\text{-}mag}}$. Therefore the two-temperature model is extended to a three temperature model including the magnetic system, which is also used to describe ultrafast demagnetisation [105]. An Elliot-Yaffet phonon-mediated spin-flip scattering was proposed to cause the coupling [106] of the magnetic system to the other subsystems. The heat capacities of the phonons and the magnetic system and their coupling constants to the electrons determine whether the magnetic system or the phononic system equilibrates first with the electronic system. These two possibilities also correspond to the two types of ultrafast demagnetisation reported for transition metals like nickel and rare-earth metals like gadolinium [106, 107].

3.3.1 Limitations of the constant Grüneisen parameter

In the following chapters the analysis of the total stress arising from the subsystems assumes a macroscopic Grüneisen constant of each subsystem, which I determine from thermal expansion data of bulk material. This section discusses the limitations of this assumption on ultrafast timescales and its thin film application. The assumption of a macroscopic Grüneisen constant for each subsystem corresponds to a temperature-independent Grüneisen parameter, which neglects the temperature-dependent occupation of different quasi-particle states and their specific Grüneisen constants. Furthermore, assuming a temperature for each subsystem on ultrafast timescales is a simplification as demonstrated in various experimental and theoretical studies even for non-magnetic metals [108–115]. The investigations reveal a mode-specific electron-phonon coupling [111, 113, 115] and a long lasting non-thermal state of both electrons and phonons for several tens of picoseconds [110, 112, 114, 116]. Furthermore, the electron-phonon coupling depends on the non-thermal electron state after laser-pulse excitation [108, 109], which may be used to manipulate the electron-phonon coupling by specific optical excitation [117]. In case of strictly mode-specific Grüneisen constants for electrons and phonons these non-thermal distributions on picosecond timescale influence the induced lattice stress and should be taken into account for an exact solution as demonstrated in [31] by *Reid et al.*. In this case the description of the stress is given by equations (3.27) and (3.32). However, this potentially long lasting non-equilibrium of the phonons only influences the lattice stress, if the mode-specific Grüneisen constants of the strongly excited modes by electron-phonon coupling differ significantly from the thermodynamic average over all modes. In the simple case of a shared Grüneisen constant for all modes, the assumption of a macroscopic Grüneisen constant is even exact.

In addition to this potential modification of the Grüneisen parameter on ultrafast timescales, the thin film geometry also modifies the Grüneisen parameter with respect to its bulk values. On ultrafast timescales the non-absorbing substrate does not influence the expansion of the thin film by laser-induced elastic stress (see section 3.1.2). However, the lattice mismatch between substrate and thin film induces a distortion of the unit cell of the film to ensure a coherent growth as for $SrRuO_3$ on $SrTiO_3$ [118]. Since the Grüneisen parameter of various materials depends on the unit cell volume changed by pressure [119–122], the substrate induced distortion potentially influences the anisotropic Grüneisen parameter. The relevance of this effect depends on the magnitude of the substrate-induced distortion, but also on the material. The out-of plane distortion of the SRO unit cell by $5\,‰$ corresponds to an additional elastic out-of plane-stress of about $1\,\mathrm{GPa}$, which causes a increase of the Grüneisen parameter between 2 and 10% in various materials like sodium, potassium, magnesium oxide or quartz. In contrast, the Grüneisen parameter of fluorite decreases with expansive stress [120]. In summary, the substrate-induced stress arising from an in-plane lattice mismatch between film and substrate potentially influences the Grüneisen parameter of a thin film and should be kept in mind while using bulk Grüneisen parameter.

3.3.2 The one-dimensional linear-chain model

The analysis of the picosecond strain response measured by ultrafast X-ray diffraction and the determination of the underlying stress require the modelling of the strain response to the spatio-temporal stress modelled by the Grüneisen approach. In this thesis I use a one-dimensional linear-chain model of masses and springs [123] to determine the picosecond strain response including strain waves to a spatio-temporal stress. This section introduces the model and describes the implementation of tensile and contractive stress.

On ultrafast timescales the laser excitation exclusively drives out-of-plane lattice dynamics, since the lateral homogeneous excitation and the symmetry of the thin film geometry lead to vanishing in-plane stresses and strains in the probed volume (see section 2.1.2). Therefore the laser-induced total stress σ_3^{ext} is equal to the total stress σ_3 due to the vanishing Poisson stress σ_3^{poi}. The description of the pump-probe experiment reduces to the out-of-plane direction $\hat{x}_3$. Section 2.1.2 introduces the inhomogeneous wave equation to determine the time-resolved strain response $\eta_3(x_3,t)$ to an external stress $\sigma_3^{\mathrm{ext}}(x_3,t)$. This continuum approach can be simplified by the discrete representation of the solid by a linear-chain of masses and springs following Hooke's law [123]. Here, the springs describe the elastic properties of the solid and the masses represent the unit cells of the sample structure. The masses are harmonically coupled by the springs and the chain behaves as coupled oscillators described by a set of coupled linear differential equations.

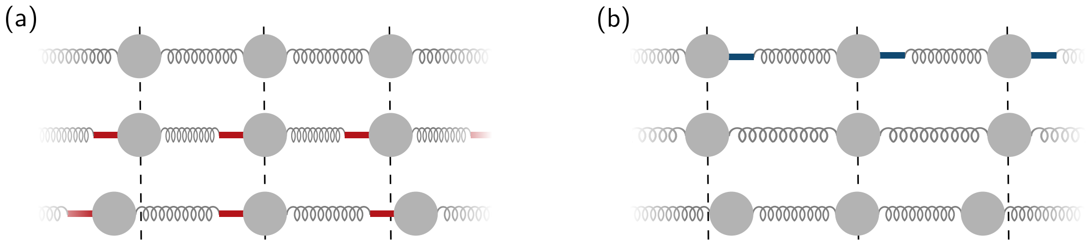

Figure 3.5: The (negative) thermal expansion of a solid represented by a one-dimensional linear-chain of masses and springs. The temperature-induced tensile or contractive stress is included by inserting (a) or removing (b) spacer sticks, respectively. The external stress at constant lattice spacing corresponds to the first conceptual step of thermal expansion (figure 3.1) and stresses the springs. In the second step the springs relax back to their initial length corresponding to the minimisation of the harmonic energy (2.7) as internal energy. This minimisation of the relevant thermodynamic potential leads to a change of lattice spacing according to the sign of the external stress and drives also strain waves for a stress rise faster than its relaxation.

In the modelling of the strain response to a laser-induced stress these coupled linear differential equations are solved numerically by the modular MATLAB library UDKM1DSIM [124] to obtain the time-resolved displacement of each mass. The thermal expansion with regard to this simplified model for $t \to \infty$ after the laser excitation is shown in figure 3.5. In analogy to figure 3.1 the (negative) thermal expansion caused by tensile or contractive stress is separated into two steps. First, inserting or removing spacer sticks represents the external stress and compresses or stretches the springs. This shifts the minimum of the total energy of the coupled harmonic oscillators to a new equilibrium spacing. In the second step the system minimises its thermodynamic potential and the springs relax back to their initial length, so that the total stress reduces to zero ($\sigma - \sigma^{\text{ext}} = 0$). The relaxation of the springs finally changes the interatomic distances.[†] It is interesting to note, this implementation of contractive stress includes an implicit saturability of the contractive stress by completely removing the initial spacer stick. Although negative thermal expansion does not have to be saturable in general, chapter 5 and 6 demonstrate a contractive magnetic stress, that saturates upon complete demagnetisation of the material.

Figure 3.5 shows that the length of the spacer sticks directly determines the thermal expansion. Therefore the length of the inserted or removed spacer sticks Δa is given by[‡]:

$$\Delta a(x_3,t) = \frac{a_0}{c_{33}} \sigma_3^{\text{ext}}(x_3,t) = \frac{a_0}{c_{33}} \sum_r \Gamma_{3,r} \rho_r^Q(x_3,t) \; . \tag{3.38}$$

The simple relation between the thermal expansion $\Delta a(x_3,t)$ and $\sigma_3^{\text{ext}}(x_3,t)$ by the elastic constant c_{33} indicates the absence of an additional Poisson stress. The time- and depth-dependent stress translates into time- and depth-dependent spacer sticks. The depth dependence of the external stress is determined by the optical penetration depth of the laser pulse leading to a depth-dependent energy density deposition. On long timescales the depth dependence is also influenced by heat transport. Here, the temporal dependence of the stress captures the energy flow between the subsystems after laser pulse excitation. The second term in equation (3.38) indicates that the superposition of the stress contributions of the subsystems determines the total length of the spacer stick. Inserting or removing the resulting total spacer sticks on a timescale faster than the relaxation time of the stress induces next to the thermal expansion in figure 3.5 also strain waves as coherent dynamic that are captured well by the linear-chain model.

[†] Note, this simplified picture exemplifies the induced external stress, whereas the internal stress arising as an elastic response to the expansion is not represented explicitly.

[‡] Equation (3.38) indicates in contrast to section 3.1, that in this approach the first step also includes the elastic properties of the solid by the diagonal element of the elastic tensor.

Chapter Four

Strain determination by ultrafast X-ray diffraction

In this thesis I use the transient strain of the sample structure to investigate the laser-induced stress contributions of phonons and magnetic excitations. The transient strain as observable requires the time-resolved determination of the out-of-plane lattice constant, which I determine by ultrafast X-ray diffraction using a pump-probe scheme. In this chapter I describe the concepts of strain determination by X-ray diffraction and the setup for measuring time-resolved lattice dynamics at the plasma X-ray source of the UDKM group in Potsdam.

The first section summarises the basic principles of X-ray diffraction and relates the diffraction signal to the lattice constant of the solid. The periodic arrangement of atoms in real space leads to a constructive interference of the scattered X-rays. This intensity maximum at a certain scattering vector is called Bragg peak. In the second section I quantitatively relate the shift of a Bragg peak in reciprocal space to a lattice strain. The third section introduces the pump-probe technique to measure the time-resolved strain after laser excitation using ultrashort X-ray pulses. These X-ray pulses are generated by a laser-based table-top plasma X-ray source its setup and X-ray pulse generation mechanism are briefly summarised.

4.1 Principle of X-ray diffraction

This section derives the relation between the lattice constant of a crystalline solid and an intensity maximum in the diffraction called Bragg peak. The Bragg peak occurs when the scattering vector $\vec{Q}$ that links the incoming $\vec{k}_{\text{in}}$ and the detected X-rays $\vec{k}_{\text{out}}$ coincides with a reciprocal lattice point of the probed crystal structure. The probed scattering vector depends on the diffraction geometry. Its systematic variation in the experiment provides a scan of the reciprocal space.

In general, the phenomenon of diffraction from a lattice corresponds to the constructive or destructive interference of different light waves. While the constructive interference occurs at a summation of amplitude in phase, the destructive interference corresponds to a phase shift of π between the scattered waves. In the case of spatially separated sources the difference in propagation length Δx determines the phase shift between the scattering contributions. Such a situation may

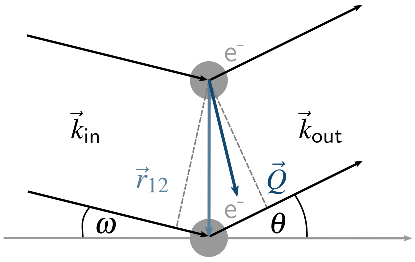

Figure 4.1: Scattering process at two electrons (e⁻) spatially separated by $\vec{r}_{12}$ with the exemplary chosen combination of the incident $\vec{k}_{\text{in}}$ and the scattered wave vector $\vec{k}_{\text{out}}$. The scattering vector is $\vec{Q} = \vec{k}_{\text{in}} - \vec{k}_{\text{out}}$. Together with the distance between the electrons it defines the phase shift of the two contributions $\Delta\phi = \vec{Q} \cdot \vec{r}_{12}$. If this phase shift is an integer multiple of 2π the contributions interfere constructively.

be associated with an elastic scattering process at more than one object separated by $\vec{r}$. Figure 4.1 exemplarily displays such a scattering geometry for two electrons that are spatially separated by $\vec{r}_{12}$. The dashed gray lines indicate the difference in propagation length of the two parallel beam components due to the spatial separation of the two scattering sources. Considering the geometry, the difference in propagation length is $\Delta x = |\vec{r}_{12}| \cdot (\sin\omega + \sin\theta)$. The corresponding phase is given by $\Delta\phi = \frac{2\pi\Delta x}{\lambda}$ with the wavelength λ. Introducing the scattering vector $\vec{Q} = \vec{k}_{\text{in}} - \vec{k}_{\text{out}}$ simplifies the description of the scattering process and the phase relation of the scattered contributions. Here, $\vec{k}_{\text{in}}$ and $\vec{k}_{\text{out}}$ denote the wave vector of the incident and the scattered light, respectively. This scattering vector determines together with the distance between the scattering sources $\vec{r}_{12}$ the phase shift

$$\Delta\phi = \vec{Q} \cdot \vec{r}_{12} = \frac{2\pi|\vec{r}|}{\lambda} \cdot (\cos(90^\circ - \omega) - \cos(90^\circ + \theta)) \ , \tag{4.1}$$

which is in agreement with the definition of the difference in propagation length using the trigonometric summation theorem. Since the wavelength λ determines the absolute value of the wave vector $\left|\vec{k}_{\text{in}}\right| = \frac{2\pi}{\lambda}$, the phase is only relevant for the interference if the spacing $\vec{r}$ and the wavelength are of the same order of magnitude. Therefore, X-rays are used for the diffraction from the crystal structure of solids with a typical lattice constant of several Angstroms.

In a solid the X-rays scatter exclusively at the electrons, due to the mass in the denominator of the cross section in the Thomson scattering. The simple case of the scattering at two electrons is sketched in figure 4.1. In the following paragraphs I extend the description of the scattering process to a crystal structure that consists of a periodic arrangement of atoms. The scattering contribution of a single atom with many electrons is given by the atomic form factor $f^0(\vec{Q})$, which results from the integral of the spatial electron distribution and the corresponding phase as in equation (4.1):

$$f^0(\vec{Q}) = \int \rho^e(\vec{r}) e^{i\vec{Q}\cdot\vec{r}} \mathrm{d}\vec{r} \tag{4.2}$$

wherein $\rho^e(\vec{r})$ denotes the spatially distributed electron density. The integral in equation (4.2) corresponds to a continuous summation of infinitesimal scattering sources with their associated phase as in the two electron case. This relates the diffraction amplitude of an atom $f^0(\vec{Q})$ to the Fourier transformation of its electron density $\rho^e(\vec{r})$ [125, p. 9].

In case of a crystalline solid the diffraction is determined by the periodic arrangement of atoms in a crystal structure that consists of a lattice and a basis. The lattice denotes the periodicity of the crystal and is given by one of the fourteen Bravais lattices [45, p. 17]. Due to its periodicity the lattice can be described by a lattice vector $\vec{R}$:

$$\vec{R}_n = n_1\vec{a}_1 + n_2\vec{a}_2 + n_3\vec{a}_3 \tag{4.3}$$

where $n_1, n_2, n_3 \in \mathbb{Z}$. Here, the absolute values of the three primitive translation vectors $\vec{a}_1$, $\vec{a}_2$ and $\vec{a}_3$ denote the lattice constants of the unit cell. Integer combinations n_1, n_2 and n_3 of the primitive vectors reach every lattice point. To result in a crystal structure, this lattice is convoluted with a basis consisting of different atoms j at the position $\vec{r}_j$ in the unit cell. This convolution results in a crystal structure with the basis pinned to every lattice point (see [125, p. 10]). This conceptual separation of the crystal structure into a lattice with a basis simplifies the analysis of the scattering contributions. The total scattering amplitude $F^{\text{crystal}}(\vec{Q})$ is the sum of the scattering contribution of each atom at the position $\vec{R}_n + \vec{r}_j$ according to the specific atom from factor $f^0(\vec{Q})$ with their phase given by the dot product with the scattering vector $\vec{Q}$:

$$F^{\text{crystal}}(\vec{Q}) = \sum_{n,j} f_j^0(\vec{Q}) e^{i\vec{Q}\cdot(\vec{R}_n + \vec{r}_j)} = \underbrace{\sum_j f_j^0(\vec{Q}) e^{i\vec{Q}\cdot\vec{r}_j}}_{\text{structure factor}} \cdot \underbrace{\sum_n e^{i\vec{Q}\cdot\vec{R}_n}}_{\text{lattice sum}} \ . \tag{4.4}$$

In equation (4.4) the summation over n denotes the summation over all possible n_1, n_2 and n_3 combinations in case of an infinite crystal in regards to the kinematic description of X-ray diffraction. The second term in equation (4.4) separates the sum over the atoms in the product of the contribution from the basis (structure factor) and the lattice (lattice sum). Thus the Fourier transformation of a convolution is the product of the Fourier transformations according to the convolution theorem. The absolute square of $F^{\text{crystal}}(\vec{Q})$ describes the intensity of the diffraction. Constructive interference enhances the intensity and this maximum of the diffraction intensity is called Bragg peak. Despite the fact that X-rays scatter exclusively from the electrons, the Bragg peak encodes the arrangement of the nuclei. While the core electrons of the atoms are located at the nuclei and inherit their periodic arrangement, the valence electrons form the interatomic binding and are strongly delocalised in metals. The spatially distributed probability density of the valence electrons leads only to weak constructive interference. Thus the constructive interference leading to a Bragg peak is dominated by the electrons localised at the ion core and the position in reciprocal space depends on the periodic arrangement of the nuclei [126].

In analogy to the diffraction from optical gratings the lattice sum describes an infinite periodic arrangement of delta functions and the structure factor a real geometrical slit of finite size. Following this analogy the lattice sum determines whether or not the Bragg peak (constructive interference of the lattice contributions) is allowed and the structure factor defines an additional amplitude factor, which could also be zero. In this case the Bragg peak is forbidden due to the arrangement of the atoms in the unit cell. This atomic arrangement of the atoms changes transiently due to the excitation of optical phonons that describe the counteracting oscillation of the atoms in the unit cell. Since the atomic arrangement determines the structure factor, the amplitude of the Bragg peak becomes time-dependent according to the frequency of the optical phonon. A famous example is the A1_g optical phonon mode in bismuth detected by an oscillation of the Bragg peak intensity that can be observed by ultrafast X-ray diffraction [127].

In the following paragraphs I describe the conditions of a constructive interference of the scattering contribution that are yielded by the lattice sum and lead to the occurrence of a Bragg peak. The lattice sum in equation (4.4) leads to a constructive summation of the contributions under the condition $\vec{Q}\cdot\vec{R}_n = m\cdot 2\pi$ with m an integer as generalised description of the two electron case in equation (4.1). This leads to the Laue condition $\vec{Q}=\vec{G}$ for elastic X-ray scattering with $\vec{G}$ the reciprocal lattice vector:

$$\vec{G} = h\vec{b}_1 + k\vec{b}_2 + l\vec{b}_3\ . \tag{4.5}$$

Here, the vectors $\vec{b}_1$, $\vec{b}_2$ and $\vec{b}_3$ describe the primitive reciprocal lattice vectors defined by the cyclic permutation of $\vec{b}_1 = \frac{2\pi}{a_1}\hat{a}_2\times\hat{a}_3$ with $\vec{a}_1 = a_1\hat{a}_1$. The Miller indices h,k,l are integers and characterise the studied Bragg peak (hkl) in a diffraction experiment. The combination of the Miller indices h,k,l corresponds to a family of lattice planes $[hkl]$. Their spacing in real space determines the scattering vector of the occurring Bragg peak. Thus the position of a Bragg peak in reciprocal space directly depends on the lattice constant of the solid via the reciprocal lattice vector $\vec{G}$. This enables the individual determination of the strain of materials with different lattice constants by monitoring the shift of the separated Bragg peaks.

Figure 4.2 sketches the co-planar diffraction geometry at lattice planes not parallel to the surface of the sample. The crystal structure with the plotted lattice planes in real space reveals the relevance of two sets of angles to describe the diffraction. The direction of the incident and the scattered wave vector are described by the angles relative to the lattice planes (ω and θ) and the angles relative to the solids surface (α_{in} and α_{out}). If the lattice planes of the diffraction are parallel to the surface these two angle pairs coincide ($\omega=\alpha_{\text{in}}$ and $\theta=\alpha_{\text{out}}$). The offset between the angle pairs corresponds to the angle between the lattice planes and the surface of the sample. In a diffraction experiment scanning the reciprocal space these angles are set by the rotation of the sample and the detector relative to the X-ray source and the sample, respectively.

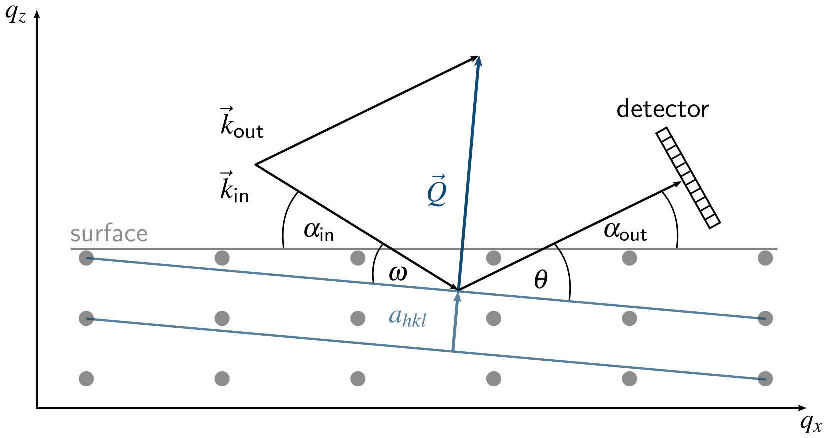

Figure 4.2: Schematic sketch of a co-planar diffraction from lattice planes non-parallel to the surface of the sample. The crystal structure (gray dots) and the plotted lattice planes with spacing a_{hkl} in real space (light blue lines) determine the diffraction. Two sets of angles (ω, θ and $\alpha_{\text{in}}, \alpha_{\text{out}}$) relative to the lattice planes and the surface describe the scattering vector $\vec{Q} = \vec{k}_{\text{in}} - \vec{k}_{\text{out}}$. The shown coordinate system of the reciprocal space is oriented with q_z perpendicular to the solids surface. The resulting geometrical relation between the two-dimensional scattering vector and the diffraction angles is given by equation (4.7).

In the special case of diffraction from lattice planes parallel to the surface of the solid the geometry simplifies the analysis by $\omega = \theta$. Under this condition the scattering vector is perpendicular to the surface of the sample and the diffraction is described by Bragg's law [45, p. 68]:

$$\frac{\lambda}{2} = a_{hkl} \sin \theta_{\text{B}} \tag{4.6}$$

where a_{hkl} denotes the spacing of the lattice planes $[hkl]$ including the diffraction order. The angle θ_{B} describes the angle between the incident X-ray beam and the lattice plane, where at $2\theta_{\text{B}}$ between incident and diffracted beam a Bragg peak occurs.
To relate these angles of the diffraction experiment to the corresponding scattering vector $\vec{Q}$ a coordinate system has to be chosen. Since this thesis only investigates thin films, the out-of-plane direction becomes the reference direction (see section 2.2.2) and is chosen as q_z component of the scattering vector. In the co-planar diffraction geometry the scattering plane contains the surface normal of the sample. Therefore the scattering vector $\vec{Q}$ is characterised by only two components q_x and q_z via the diffraction angles [128, 129]:

$$\vec{Q} = \begin{pmatrix} q_x \\ q_z \end{pmatrix} = \begin{pmatrix} \cos \alpha_{\text{out}} - \cos \alpha_{\text{in}} \\ \sin \alpha_{\text{out}} + \sin \alpha_{\text{in}} \end{pmatrix} |\vec{k}| \tag{4.7}$$

where α_{in} and α_{out} denote the incident and scattering angle relative to the surface (see figure 4.2). In the case of a diffraction from lattice planes parallel to the surface α_{in} coincides with ω and the Bragg peak occurs at $\alpha_{\text{in}} = \alpha_{\text{out}} = \theta_{\text{B}}$. In this case the Bragg peak occurs at $q_x = 0$ and the condition $\vec{Q} = \vec{G}$ simplifies the analysis to Bragg's law (4.6).

4.2 Determination of strain from Bragg peak shifts

The change of the lattice constant of a crystalline solid translates into a shift of Bragg peaks in reciprocal space. This section briefly describes the quantitative determination of the lattice strain from the Bragg peak shift in full reciprocal space mapping and single-angle measurements. Chapter 2 introduces the quantity strain as a relative change of the lattice spacing a of a solid $\eta = \frac{\Delta a}{a_0}$. This change of the lattice spacing translates into the change of the lattice vector $\vec{R}$ (4.3) and therefore also in a change of the reciprocal lattice vector $\vec{G}$ (4.5) via the reciprocal relation between primitive lattice and reciprocal lattice vectors $\vec{a}_i$ and $\vec{b}_i$. According to the Laue condition $\vec{Q} = \vec{G}$ the Bragg peak (hkl) corresponding to the lattice spacing a_{hkl} thus arises at a different scattering vector $\vec{Q}$, which corresponds to a different position in reciprocal space. This shift of the Bragg peak in reciprocal space directly depends on the changed lattice spacing. The out-of-plane laser-induced strain of thin films investigated in this thesis results in a shift of the Bragg peak at $q_x = 0$ along the q_z-direction that originates from the changing spacing of the lattice planes parallel to the surface of the sample. The corresponding shift of the Bragg peak along the q_z-direction in reciprocal space is monitored by a symmetric θ-2θ-scan, where ω is equal to θ and both angles are changed together. The shift of the Bragg peak Δq_z observed by this routine determines the out-of-plane strain η_3 by:

$$\eta_3 = \frac{a_3 - a_{3,0}}{a_{3,0}} = \frac{q_{z,0} - q_z}{q_z} \ . \tag{4.8}$$

The full reciprocal space mapping by rotating the sample and the X-ray detector is time consuming especially in time-resolved measurements, which require a θ-2θ-scan for each time delay between pump and probe pulse. Using a position-sensitive line or area detector provides an alternative measurement routine called reciprocal space slicing [130].

As sketched in figure 4.2 a position-sensitive line or area detector detects simultaneously the diffraction intensity for different angles θ. According to equation (4.7) this relates to different scattering vectors and thus to a subset of the reciprocal space. If the detector only covers a small range of $\Delta\theta \ll \theta$, the detector can be approximated as a linear subset in the reciprocal q_x-q_z-space that depends on the diffraction angle θ:

$$q_z = -\frac{q_x}{\tan\theta} + q_{z,0} \ . \tag{4.9}$$

In the reciprocal space slicing scheme the diffraction angles are set to the Bragg angle ($\omega = \theta = \theta_\mathrm{B}$) and the shift of the Bragg peak in reciprocal space is monitored within the subset of the reciprocal space provided by the position-sensitive detector. This single angle measurement requires a Bragg peak that is broadened along the q_x-direction, because the Bragg peak otherwise shifts out of the probed subset of the reciprocal space when an out-of-plane strain occurs.

In a diffraction experiment at a real solid the Bragg peak may become broad due to a non-monochromatic, non-parallel X-ray beam, a pronounced mosaicity or internal strain gradient of the sample. The mosaicity describes the tilting of crystallites in non-perfect crystals relative to the out-of plane direction, which is often related to thin films. Due to the mosaicity the sample intrinsically exhibits lattice planes slightly non-parallel to the surface. The diffraction from these lattice planes leads to the occurrence of a Bragg peak at $\alpha_\mathrm{out} \neq \theta$ corresponding to a broadening of the total Bragg peak along q_x. Therefore reciprocal space slicing is a time-effective and suitable method to measure the strain of non-perfect crystalline thin films. The shift of the Bragg peak on the detector corresponds to a change of the diffraction angle $\Delta\theta$, which translates via equation (4.7) to a shift along q_z. Thus the strain detected with this method for small $\Delta\theta$* reads [130]†:

$$\eta_3 = \frac{q_{z,0} - q_z}{q_z} \approx S \cdot \frac{-\Delta\theta}{2} \cot\theta_\mathrm{B} \tag{4.10}$$

---

*In this context small means that the assumption of a Taylor expansion to the first order is justified:

$$\sin(\theta_\mathrm{B} + \Delta\theta) = \sin\theta_\mathrm{B} \cdot \cos\Delta\theta + \sin\Delta\theta \cdot \cos\theta_\mathrm{B} = \sin\theta_\mathrm{B} + \cos\theta_\mathrm{B} \cdot \Delta\theta$$

†Note, inserting $a_3 = \frac{2\pi k}{q_z}$ from Bragg's law results in q_z in the denominator of the relative q_z change. Since the relative shift of the Bragg peak typically does not exceed several permill, q_z can be approximated by $q_{z,0}$ to simplify the relation between strain and angular shift on the detector.

wherein the factor S denotes a geometrical scaling factor depending on the dimensions of the Bragg peak in reciprocal space and the diffraction angle. In the case of mosaic thin films this factor is of order unity but increases for perfect crystals by an order of magnitude. This geometric scaling factor will be discussed in a dedicated publication from our group. [130]

4.3 Pump-probe experiments with X-ray diffraction

This section describes the experimental setup for the time-resolved X-ray diffraction experiments presented in chapter 5 and 6. This includes the excitation conditions in a pump-probe experiment and the generation of ultrashort X-ray pulses using the laser-based table-top plasma X-ray source of the UDKM-group in Potsdam [131, 132]. The previous sections demonstrate the capability of X-ray diffraction to measure the lattice constant via the position of the Bragg peak in reciprocal space. The change of the lattice constant translates into a Bragg peak shift in reciprocal space and is monitored by full reciprocal space mapping or in case of mosaic thin films by reciprocal space slicing. The time-resolved determination of the strain response to a laser-induced stress may be realised by a pump-probe technique, which requires ultrashort X-ray pulses to probe the time-resolved lattice spacing by ultrafast X-ray diffraction.

The pump-probe technique typically involves the splitting of an ultrashort laser-pulse into two, where one excites the sample and the second probes the induced sample response. The time delay between the pump and the probe pulse provides a snapshot of the induced dynamics at a certain time after the excitation corresponding to the delay between the pump and probe pulse. Therefore repeating the experiment with various time delays between pump and probe pulse reveals the time-dependent processes. Therefore the pump-probe technique requires a reversible response of the sample that comes back to the initial state within the inverse repetition rate of the laser. Since the time-resolution of the technique depends next to geometrical time-smearing effects and the uncertainty of the delay setting on the duration of the probe pulse, the time-resolved determination of the strain response requires ultrashort X-ray pulses. Such an ultrashort X-ray pulse as probe pulse for a pump-probe experiment is generated at the laser-based table-top plasma X-ray source of the UDKM group in Potsdam [131, 132]. Figure 4.3 schematically shows the experimental setup for the experiments on $\mathrm{SrRuO_3}$ and dysprosium presented in chapter 5 and 6.

The laser system consist of a *Mantis* oscillator generating ultrashort laser pulses and a *Legend Elite Duo* chirped-pulse amplifier system, which generates intense, near-infrared laser pulses with a duration of approximately 40 fs and a repetition rate of 1 kHz. The generated laser pulses are split up into an intense probe pulse and a weak pump pulse by a beam splitter. Unlike typical pump-probe experiments the 'probe' laser pulse is relatively intense, because it is used to generate the X-ray probe pulse. The pump pulse is led over the mechanical delay stage towards the sample, which is mounted on a two-circle goniometer for the geometrical setting of the X-ray diffraction. The mechanical delay stage determines the time delay between the pump and probe pulse. Their temporal overlap is adjusted before the experiment using a superlattice reference sample [134, 135]. Additionally the spot size A and the power of the pump beam $P = E \cdot 1\,\mathrm{kHz}$ with the pulse energy E are adjusted by a lens telescope and a combination of a $\lambda/2$-plate and a pair of polarising mirrors (not shown), which set the polarisation of the pump pulse to p-polarisation [14]. This modification sets the excitation density called fluence F:

$$F = \frac{E}{A} = \frac{E \sin(\omega + 20^\circ)}{\pi \sigma_x \cdot \sigma_y} . \tag{4.11}$$

Here, σ_x and σ_y denote the spatial extension of the pump beam assuming a two-dimensional, elliptical top-hat profile, where the pulse energy is spread homogeneously within the area. Furthermore, the sample conditions can be set by a closed-cycle cryostat and a vacuum chamber providing an adjustable sample temperature, which is particularly important in the context of magnetic materials due to the arising magnetic order below the magnetic order temperature.

Meanwhile, the probe beam is guided onto a parabolic mirror, which focusses the intense optical probe pulse on a 10 or $20\,\mu\mathrm{m}$ thick copper tape. The widening of the probe beam in front of the parabolic mirror improves the focus on the copper tape. Focussing the intense ultrashort laser pulse on the copper tape creates an electron plasma due to the changed nuclear potential by the strong electric field releasing the valence electrons. The freed valence electrons are subsequently accelerated in the oscillating electric field of the laser pulse and their recollision with the copper band generates X-ray radiation [132, 133, 136]. The details of this complex X-ray generation with a strong laser field are still an area of research that aims for improving the laser-based plasma X-ray generation process [137, 138]. In a simple picture this generation process is very similar to the generation mechanism in classical X-ray tubes. In a X-ray tube a static electric field accelerates the electrons onto a metal target and the deceleration of the electrons in the target generates radiation. This radiation contains X-rays, which can be classified either as Bremsstrahlung or as characteristic radiation from the excitation of core electrons. In a plasma X-ray source the static electric field is replaced by the oscillating electric field of the laser pulse accelerating the electrons during the presence of the laser pulse. Thus the length of the generated X-ray pulse is of the same order of magnitude as the optical laser pulse. At the plasma X-ray source the length of the X-ray probe pulse is typically approximately $200\,\mathrm{fs}$ [128].

The generated X-ray radiation contains various wavelengths analogue to the classical X-ray tube. Since a not well defined incident wave vector $\vec{k}_{\mathrm{in}}$ due to different wavelengths broadens the Bragg peak in reciprocal space, the precise determination of the lattice strain requires a monochromatisation of the X-ray pulse. A fraction of the isotropically emitted X-ray photons pass through a Montel optic. The Montel optic monochromatises the X-ray pulse to Cu-K$_\alpha$-radiation ($\lambda = 1.54\,\text{Å}$) and focusses the beam to a $300 \times 300\,\mu\mathrm{m}^2$ beam spot at the sample position [139]. The X-ray generation efficiency strongly fluctuates, mainly due to the mechanical instabilities of the moving copper tape in the laser focus. Therefore the generated X-ray intensity is recorded for each incoming laser pulse using a reference detector that detects a fraction of the transmitted X-rays

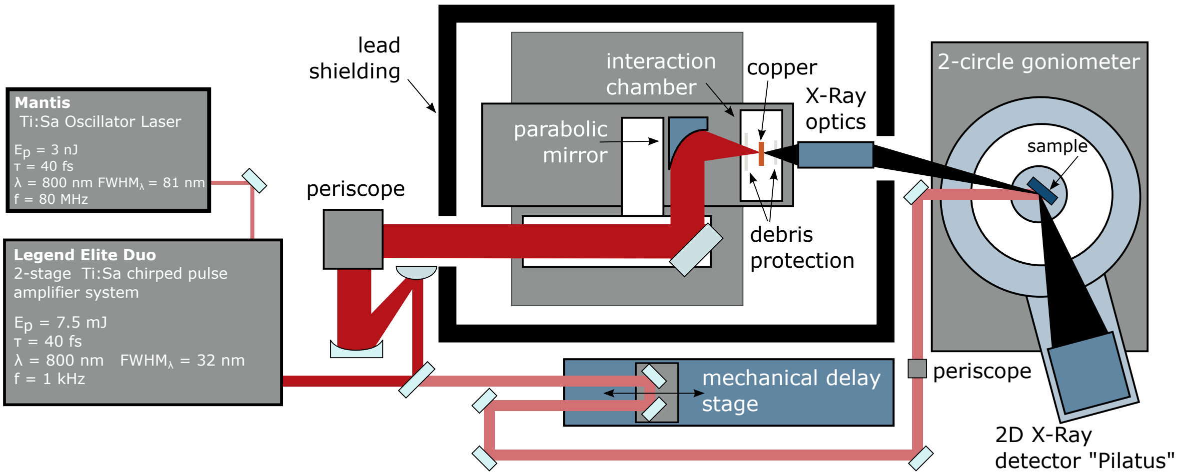

Figure 4.3: Schematic sketch of the plasma X-ray source to measure time-resolved laser-induced lattice dynamics by X-ray diffraction. The laser system of *Mantis* and *Legend Elite Duo* generates femtosecond laser pulses with a repetition rate of $1\,\mathrm{kHz}$. The laser pulses are separated into a probe and a pump pulse. The parabolic mirror focusses the probe pulse on a copper tape generating X-ray pulses. The subsequent Montel optic monochromatises and focusses the X-ray pulse on the sample and the scattered X-ray photons are detected by a *Pilatus* area detector. The diffraction geometry is adjusted by a two-circle goniometer orienting the sample and the detector individually. A lens telescope and a combination of $\lambda/2$-plate and polarising mirrors determine the excitation density and the mechanical delay stage adjusts the time delay between pump and probe pulse in the pump-probe experiment. (Adopted from [133])

for the normalisation [132]. The subsequent diffraction is determined by the orientation of the sample and the detector on a two-circle goniometer. The orientation of the sample relative to the incoming radiation defines the angles ω and α_{in} and the wave vector $\vec{k}_{\text{in}}$ (see figure 4.2) by rotating the inner circle. Since the Montel optic focuses the X-ray beam, the incoming beam provides intrinsically different wave vectors $\vec{k}_{\text{in}}$ corresponding to the convergence of $0.3°$.
The X-ray photons of the probe pulse ($\approx 1 \cdot 10^6 \, \frac{\text{Photons}}{\text{s}}$ [136]) are scattered from the sample and the intensity is detected by a two-dimensional *Pilatus* detector, whose position is adjusted by the outer circle of the goniometer that determines the angles θ and α_{out}. The gated single-photon area detector is divided into $172 \times 172\,\mu\text{m}^2$ sized pixels. Since each pixel corresponds to a different $\vec{k}_{\text{out}}$ the intensity $I(\vec{Q})$ for different scattering vectors $\vec{Q}$ is measured. The intensity of the vertical pixels (direction perpendicular to the diffraction plane) is summed [133] and the diffraction geometry becomes co-planar as sketched in figure 4.2. Thus each horizontal pixel corresponds to specific q_x-q_z-coordinates and the detector measures the intensity along a slice through the reciprocal space as shown by equation (4.9). In the here reported ultrafast X-ray diffraction on thin magnetic films I follow the shift of the Bragg peaks for different, mechanically set pump-probe delays. The time-dependent peak position is determined using Gaussian fits or center-of-mass analysis of the diffracted intensity distributions as detailed in the following chapters.

CHAPTER FIVE

SATURATION OF THE MAGNETIC STRESS IN SRRUO$_3$ PROBED BY DOUBLE-PULSE EXCITATION

In this chapter I investigate the influence of the magnetic stress on the ultrafast expansion under the facilitating conditions of a homogeneous excited transducer and a sub-picosecond equilibration of the subsystems. The two different excitation fluences enables the investigation of the role of the saturation of the magnetic stress for the temperature dependence of the picosecond strain response. I present the temperature-dependent ultrafast strain response of a ferromagnetic strontium ruthenate (SRO) metal film on an insulator strontium titanate (STO) substrate to a double-pulse excitation measured by ultrafast X-ray diffraction. In the ferromagnetic phase the magnetic excitations induce a contractive stress that counteracts the tensile phonon stress. Therefore, the total lattice stress upon laser-excitation decreases below the Curie temperature T_C. The laser-induced full demagnetisation of the transducer is equivalent to a saturation of the magnetic stress. The strain response to the second excitation indicates this saturation by the absence of a contractive magnetic stress contribution exciting the fully demagnetised film. The analysis of the temperature and fluence dependence of the total stress using an anisotropic Grüneisen model reveals the role of the saturated magnetic stress.

In the first section I determine the anisotropic Grüneisen constant of the phonons and the magnetic excitations by separating the thermal expansion and the heat capacity of SRO into the subsystem contributions. The second section describes the determination of the picosecond strain response by reciprocal space mapping in a pump-probe experiment including a double-pulse excitation. In the last section I present the temperature- and fluence-dependent strain response. Below T_C, the excitation of the magnetic subsystem reduces the ultrafast expansion driven by the total laser-induced stress. The Grüneisen model assuming equilibrated subsystems extracts the temperature-dependent magnetic stress contribution. It is proportional to the magnetic heat capacity in the limit of small fluences, but follows the integral of the remaining magnetic heat capacity in the regime of high excitation fluences where SRO is transiently excited above T_C.

5.1 Equilibrium properties of a thin SrRuO$_3$ film

This section prepares the analysis of the ultrafast X-ray diffraction experiments that yield the picosecond strain by summarising the equilibrium properties of SrRuO$_3$. Below the Curie temperature $T_\mathrm{C} = 160\,\mathrm{K}$, SRO exhibits a ferromagnetic order. Its excitation induces a contractive stress that leads to an Invar behaviour by the compensation of the tensile phonon stress. I use the equilibrium expansion and the subsystem-separated heat capacity C_tot to determine the anisotropic Grüneisen constants of the phonons and the magnetic excitations $\Gamma_{3,\mathrm{ph}} = 1.6$ and $\Gamma_{3,\mathrm{mag}} = -26$ that I use to model the temperature-dependent laser-induced stress in the following sections.

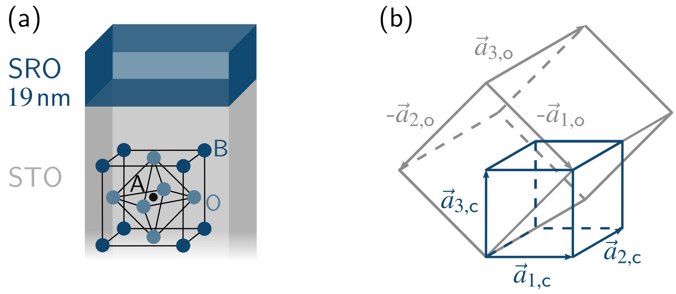

Figure 5.1: Schematic sketch of the crystal structure of the perovsikte sample. (a) The sample structure consists of a 19 nm SRO metal film on an insulating STO substrate. The inset depicts the cubic unit cell of the perovskite structure ABO$_3$. The A atom is in the center of an oxygen octahedron within the cubic arrangement of the B atoms. The panel (b) displays the orientation of the orthorhombic and pseudocubic unit cell representation of SRO relative to the out-of-plane direction in the thin film geometry given by $\vec{a}_{3,c}$.

The following paragraphs describe the crystal structure of the sample that consists of a 19 nm crystalline SrRuO$_3$ transducer grown on a single crystal SrTiO$_3$ substrate using pulsed laser deposition [140, 141]. Both the transducer and the substrate exhibit the perovskite crystal structure with the stoichiometry ABO$_3$. In the case of a cubic lattice, the A atom in the center of the unit cell is surrounded by an oxygen octahedron, which is embedded in the cubic arrangement of the B atoms as depicted in figure 5.1(a). In STO the tilting of the oxygen octahedra leads to a slight tetragonal distortion of the cubic unit cell below 105 K. Above this structural phase transition STO exhibits a cubic unit cell with a lattice constant of $a = 3.905\,\text{Å}$ at 300 K [118, 142]. In contrast, the tilting of the oxygen octahedra in SRO remains up to 950 K [143], which leads to an orthorhombic unit cell of SRO at 300 K with the lattice constants $a_{1,\mathrm{o}} = 5.573\,\text{Å}$, $a_{2,\mathrm{o}} = 5.554\,\text{Å}$ and $a_{3,\mathrm{o}} = 7.851\,\text{Å}$ [25, 144, 145]. Due to the only slight orthorhombic distortion ($a_{1,\mathrm{o}} \approx a_{2,\mathrm{o}}$), the orthorhombic unit cell can be associated with a pseudocubic unit cell [146, 147]. The relation between these two representations is depicted in figure 5.1(b). The lattice vectors $a_{1,\mathrm{o}}$ and $a_{2,\mathrm{o}}$ form the face diagonals of the pseudocubic unit cell and the lattice constant $a_{3,\mathrm{o}}$ is twice the pseudocubic lattice constant $a_{2,\mathrm{c}}$ according to the doubling of the unit cell along this direction due to the counterrotation of neighbouring oxygen octahedra. Thus the lattice constants of the two representations are related by $a_{2,c} = 0.5 \cdot a_{3,o}$ and $a_{1/3,c} = \frac{1}{\sqrt{2}}(a_{1,o} + a_{2,o})$, which results in a pseudocubic lattice constant of $a_\mathrm{c} = 3.93\,\text{Å}$ [146, 147].

The unit cells in the thin SRO film on the STO substrate are oriented with the orthorhombic $[110]_\mathrm{o}$- and the pseudocubic $[001]_\mathrm{c}$-direction pointing out-of-plane [148, 149]. The small in-plane lattice mismatch ($-0.67\,\%$) of the bulk lattice constants of the pseudocubic SRO ($3.93\,\text{Å}$) and the cubic STO ($3.905\,\text{Å}$) unit cells ensures a coherent growth of the SRO film on the STO substrate. The coherent growth changes the in-plane lattice constants of the SRO unit cells at the transducer-substrate interface to those of the STO substrate. Thus the lattice mismatch induces an in-plane biaxial compressive stress that translates via the Poisson effect to a tensile out-of-plane stress increasing the lattice constant by $0.5\,\%$ with respect to bulk material [118].

5.1.1 X-ray diffraction perspective on the sample structure

In this section I present the characterisation of the sample by X-ray diffraction. In a co-planar geometry (figure 4.2), X-ray diffraction using a microfocus Cu-K_α X-ray source yields a reciprocal q_x-q_z-space map that determines the out-of-plane lattice constant of the materials by their Bragg peak position along the q_z-direction. The temperature-dependent Bragg peak position of SRO displays a negative thermal expansion in the ferromagnetic phase while STO exclusively expands.

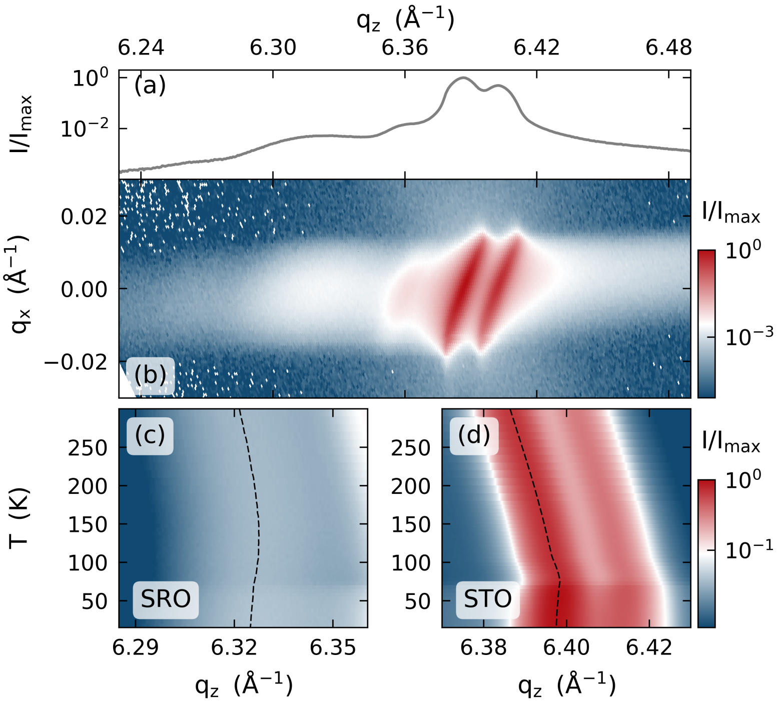

Figure 5.2: Characterisation of the sample by X-ray diffraction. The integration of the reciprocal space map at $300\,\mathrm{K}$ (b) along the q_x-direction yields the projection of the diffraction intensity on the q_z-axis (a). The barely separated $(004)_\mathrm{c}$ Bragg peaks of SRO at $6.32\,\mathrm{Å}^{-1}$ and STO at $6.39\,\mathrm{Å}^{-1}$ as intensity maxima correspond to the similar out-of-plane lattice constant of the materials. The temperature-dependent intensity distribution along q_z displays the out-of-plane contraction of the SRO film (c) and the expansion of the STO substrate (d) by the Bragg peak shift. In (c) the SRO Bragg peak is scaled by a factor of ten to improve the contrast.

In figure 5.2(b) the reciprocal space map of the sample structure at $300\,\mathrm{K}$ displays the barely separated $(004)_\mathrm{c}$ Bragg peaks of the film and the substrate as intensity maxima. The position of the Bragg peaks along the q_z-direction encodes the out-of-plane lattice constants* via $q_z = \frac{m \cdot 2\pi}{a_{3,c}}$. Integrating the reciprocal space map along the q_x-direction yields the projection on q_z in figure 5.2(a), which displays the Bragg peak of SRO at $6.32\,\mathrm{Å}^{-1}$ and of STO at $6.39\,\mathrm{Å}^{-1}$.

The intensity distribution in reciprocal space is generally given by the convolution of the diffraction intensity from the lattice according to equation (4.4) and the instrument resolution area [128, 130]. In case of the single-crystal substrate the shape of the Bragg peak corresponds to the instrument resolution area, because the intrinsic diffraction yields a delta peak. As shown in figure 5.2(b) the resolution area of the plasma X-ray source (see section 4.3) consists of two parallel, along q_x elongated ellipses, which correspond to the characteristic X-ray radiation $K_{\alpha,1}$ and $K_{\alpha,2}$ and the convergence of the X-ray beam. The Bragg angle θ_B of the substrate determines their tilt angle with respect to the q_x-direction [128]. The absence of a pronounced instrument resolution area for the SRO Bragg peak indicates a broad intrinsic diffraction intensity distribution. This relates to a non-prefect periodicity of the only 48 unit cells thick crystal structure. The Bragg peak of the SRO film appears as a shoulder on the left of the STO Bragg peak due to the similar out-of-plane lattice constant. The only slight broadening along q_x indicates a negligible mosaicity of the SRO film. The broadening along q_z may be related to a gradient of the substrate-induced deformation along the out-of-plane direction in the film due to the in-plane lattice mismatch.

---

*The q_z direction only describes the out-of-plane direction in regards to the choice of the reciprocal coordinate system used in this thesis, which is introduced in section 4.1.

The lattice mismatch also distorts the substrate [150]. The diffraction maximum at $6.36\,\text{Å}^{-1}$ resembles the ellipses of the instrument resolution area, which hints at a strained surface layer of the substrate. The projection on the q_z-axis provides access to the thermal out-of-plane expansion of the thin film and the substrate. In figures 5.2(c) and (d) the temperature-dependent q_z-projections display a temperature-induced shift of the Bragg peaks along q_z, which determines the out-of-plane strain according to equation (4.8). Fitting the corresponding q_z-projections with four Pseudovoigt profiles according to the number of intensity maxima determines the temperature-dependent Bragg peak positions[†], which are denoted by black dashed lines. The shift of the Bragg peak of STO to smaller q_z values indicates a positive thermal expansion above $105\,\text{K}$. In contrast, SRO contracts along the out-of-plane direction up to the magnetic order temperature T_C indicated by the shift of the Bragg peak to higher q_z values.

5.1.2 Magnetism influencing thermodynamic properties

In this section I briefly summarise the magnetic properties of SRO and their coupling to the lattice. The coupling of magnetism and lattice results in an anisotropically reduced thermal expansion in the ferromagnetic phase. Below the Curie temperature $T_C = 160\,\text{K}$, the ferromagnetic order provides an energy reservoir described by a magnetic contribution to the heat capacity contribution, which I extract from the total heat capacity.

Bulk SRO becomes ferromagnetic below the Curie temperature of $T_C = 160\,\text{K}$ [151, 152]. The finite magnetic moment of $1.62\,\mu_B$ per Ru-atom [145, 153] originates from the itinerant ferromagnetism of the strongly hybridised Ru-4d and O-2p electrons [152–154]. The resulting macroscopic magnetisation M points along the easy axis in $[100]_o$-direction for bulk SRO. In case of a thin film on STO the magnetisation points at 45° with respect to the surface normal at T_C according to the orientation of the orthorhombic unit cell (see figure 5.1). With decreasing temperature the angle continuously changes to 30° [155, 156]. The orientation of the magnetisation in the thin film geometry indicates an unusually high magnetocrystalline anisotropy with an anisotropy field of around $7\,\text{T}$ [157] that dominates over the shape anisotropy. This high magnetocrystalline anisotropy indicates a strong spin-orbit interaction, which is experimentally observed by a high ferromagnetic resonance frequency and a fast phonon-mediated demagnetisation [157, 158]. These findings indicate a pronounced interplay of the crystal structure and the ferromagnetism in SRO. In thin film samples, the substrate-induced tetragonal distortion of the pseudocubic unit cell changes the magnetic properties by reducing the Curie temperature to $T_C = 150\,\text{K}$. It also broadens the second order phase transition, which is especially pronounced in recently grown SRO nanodots [118, 141]. The changing temperature-dependent magnetisation including the reduced Curie temperature is depicted in figure 5.4(a). Vice versa, the magnetic order also influences the lattice by freezing the temperature-dependent mutual oxygen octahedra tilting in the ferromagnetic phase as observed by neutron diffraction experiments [144, 145]. This coupling between lattice and magnetism leads to a finite lattice stress caused by the excitation of the magnetic order. In the ferromagnetic phase this additional stress results in a vanishing volumetric expansion coefficient β of SRO [25, 144, 145]. This volumetric Invar effect indicates a contractive stress contribution by the magnetic excitations that counteracts the normal expansive phonon stress.

The temperature-dependent strain of the orthorhombic lattice constants from the literature [25, 144, 145] is depicted in figure 5.3(a). The lattice constant along the $[100]_o$ and $[001]_o$-direction show an Invar behaviour up to the Curie temperature $T_C = 160\,\text{K}$, while the lattice constant along the $[010]_o$-direction exhibits a positive thermal expansion. Despite the positive thermal expansion the absence of a kink in the strain at the phase transition indicates a contractive magnetic stress along the $[010]_o$-direction. While in the paramagnetic phase the expansion along

---

[†] The Pseudovoigt profile contains four parameters: the amplitude, the width, the position and the weighting of Gaussian and Lorentz profile. The parameters of the two Pseudovoigts describing the substrate Bragg peak with the instrumental resolution area are related by temperature-independent factors.

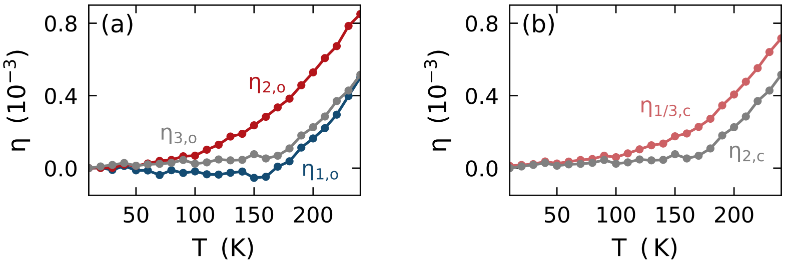

Figure 5.3: Anisotropic thermal expansion along the orthorhombic (a) and pseudocubic (b) unit cell directions of SRO [25, 144, 145]. An anisotropic contractive magnetic stress results in an Invar behaviour of $\eta_{1,\mathrm{o}}$ and $\eta_{3,\mathrm{o}}$ with nearly vanishing expansion below $T_\mathrm{C} = 160\,\mathrm{K}$. In contrast, $\eta_{2,\mathrm{o}}$ displays a positive thermal expansion. The relation of the orthorhombic and the pseudocubic unit cell representation determines the two different pseudocubic lattice strains according to figure 5.1(b). Along the out-of-plane direction of the thin film sample ($\vec{a}_3$) the pseudocubic unit cell shows an expansion even in the ferromagnetic phase.

the orthogonal directions induces a contractive stress by the Poisson effect, in the ferromagnetic phase the contractive magnetic stress replaces the vanishing Poisson stress due to the Invar behaviour. In total, the direction-dependent behaviour of the strain displays an anisotropic magnetic stress that counteracts the isotropic tensile phonons stress that results in the shared temperature dependence of the lattice constants in the paramagnetic phase. The relation between the orthorhombic (subscript o) and pseudocubic (subscript c) representation of the unit cell in figure 5.1(b) determines the temperature-dependent expansion of the pseudocubic unit cell by $\eta_{1/3,\mathrm{c}} = 0.25 \cdot \sqrt{(1+\eta_{1,\mathrm{o}})^2 + (1+\eta_{2,\mathrm{o}})^2} - 1$ and $\eta_{2,\mathrm{c}} = \eta_{3,\mathrm{o}}$. The resulting strain of the pseudocubic unit cell in figure 5.3(b) displays an identical positive expansion along two directions $\left(\eta_{1/3,\mathrm{c}} > 0\right)$ and an Invar behaviour along the third direction in the ferromagnetic phase. In the Grüneisen model the anisotropic magnetic stress originates from an energy density deposited to the magnetic subsystem that is given by the integral of the magnetic heat capacity.

In the following paragraphs I extract the magnetic heat capacity contribution from the total heat capacity at constant volume C_tot [159] by modelling the electronic and phononic temperature-dependent heat capacity contributions. In the first step I use the Sommerfeld model to approximate the electronic contribution by $C_\mathrm{el} = \gamma_\mathrm{S} T$ wherein γ_S denotes the Sommerfeld constant of SRO $\gamma_\mathrm{S} = 30\frac{\mathrm{mJ}}{\mathrm{mol \cdot K^2}} = 0.8\frac{\mathrm{mJ}}{\mathrm{m^3 \cdot K^2}}$ [159]. In the second step I model the temperature-dependent phonon contribution to the heat capacity. Since the Debye temperature Θ_D becomes strongly temperature-dependent in SRO due to the widely dispersed phonon density of states including high frequency optical phonons, the phononic contribution to the heat capacity is not well described by a Debye model. Instead I use the weighted sum of the heat capacities of the respective oxides SrO [160] and RuO [161] to describe the phononic heat capacity contribution as frequently used in the literature [162]. In the paramagnetic phase above $200\,\mathrm{K}$ the phononic contribution to the heat capacity is determined by the difference between the electronic contribution and the total heat capacity. I determine the temperature-independent weighting factors of the oxide heat capacities by fitting the phononic contribution in this temperature range. The weighting factors determine the temperature-dependent phononic contribution to the heat capacity. Finally, the magnetic contribution to the total heat capacity for bulk SRO is determined by the difference between the total heat capacity and the contributions from electrons and phonons. Figure 5.4(b) depicts the subsystem-separated heat capacity contributions. The magnetic contribution vanishes at $T_\mathrm{demag} = 200\,\mathrm{K}$ slightly above the Curie temperature T_C. The resulting finite integral of the magnetic heat capacity contribution is equivalent to a saturation of the magnetic stress due to a maximum amount of energy density storable to the magnetic excitations.

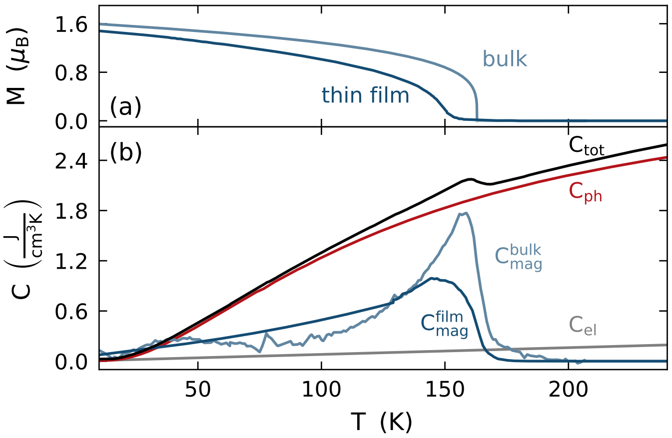

Figure 5.4: Temperature-dependent magnetisation and subsystem-separated heat capacity for bulk SRO and a thin film on STO. In panel (a) the temperature-dependent magnetisation [141, 155] displays a shifting and broadening of the phase transition in the thin film. I consider this change by a magnetic heat capacity of the thin film $C_{\text{mag}}^{\text{film}} \propto M \cdot \mathrm{d}M/\mathrm{d}T$ via molecular field theory. Panel (b) depicts the final separation of the total heat capacity [159] into the contributions from electrons, phonons and the magnetic system (scaled by a factor of 10).

In thin films, the substrate-induced distortion of the pseudocubic unit cell influences the magnetism by shifting the transition temperature to lower temperatures and broadening the phase transition. To analyse my experiment in section 5.3, I include these changes of the magnetisation into the magnetic heat capacity. The molecular field theory relates the magnetisation and the magnetic heat capacity by $C_{\text{mag}} \propto M\frac{\mathrm{d}M}{\mathrm{d}T}$ [96, p. 179]. Using the magnetisation $M(T)$ of a comparable film [141, 155] (figure 5.4(a)) yields the magnetic heat capacity of a thin film $C_{\text{mag}}^{\text{film}}$. Here, I use the description of the magnetisation by Bloch's $T^{\frac{3}{2}}$ law for temperatures below $130\,\text{K}$ [155]. The amplitude of the heat capacity is determined by fitting the heat capacity below $50\,\text{K}$ to the magnetic heat capacity of bulk SRO. The comparison with the bulk magnetic heat capacity in figure 5.4 displays a shift of the maximum by $-10\,\text{K}$ with respect to bulk according to the reduced Curie temperature in the thin film geometry.

5.1.3 Determination of anisotropic Grüneisen constants

In this section I relate the anisotropic Invar behaviour in the ferromagnetic phase of bulk SRO to a contractive stress provided by the magnetic excitations. The out-of-plane external stress σ_3^{ext} extracted from the thermal expansion in equilibrium along the corresponding crystal direction determines the phononic and magnetic Grüneisen constant. The Grüneisen approach separates the total external stress into the contribution of the phonons and the magnetic excitations that prepare the application to the laser-induced stress in the following.
The Grüneisen approach linearly relates the energy density ρ_r^Q in each subsystem r to an out-of-plane stress contribution $\sigma_{3,r}^{\text{ext}}$ by a subsystem-specific Grüneisen parameter $\Gamma_{3,r}$. These stress contributions superimpose to the total anisotropic external stress σ_3^{ext}, which induces a lattice strain η_3 via Hooke's law (2.13). In thermal equilibrium the thermal expansion along the orthogonal crystal directions provides an additional Poisson stress $\sigma_3^{\text{poi}} = \sum_{\lambda\neq 3} c_{\lambda 3}\eta_\lambda$ via the off-diagonal elements of the elastic tensor $c_{\lambda 3}$. Therefore the thermal expansion η_3 is induced by both the external stress and the Poisson stress according to $c_{33} \cdot \eta_3 = \sigma_3^{\text{ext}} - \sigma_3^{\text{poi}}$. In case of SRO the pseudocubic symmetry of the lattice simplifies the Poisson stress to $\sigma_3^{\text{poi}} = c_{12}\,(\eta_1 + \eta_2)$ and the

definition of the anisotropic Grüneisen constant (3.17) to:

$$\Gamma_{3,r} = \frac{\sigma_{3,r}^{\text{ext}}}{\rho_r^Q} = \frac{c_{33}}{\rho_r^Q}\left(\eta_{3,c} + \frac{c_{13}}{c_{33}}\left(\eta_{1,c}+\eta_{2,c}\right)\right)_r \,, \tag{5.1}$$

wherein the subscript r denotes the contribution of the subsystem r to the strain components. Figure 5.5 displays the extraction of the external stress from the total stress driving the expansion in thermal equilibrium $\sigma_3 = c_{33}\cdot\eta_{3,c}$ for both bulk SRO (a) and the thin film sample (b). In the case of bulk material the in-plane expansion is given by the pseudocubic lattice strains $\eta_{1,c}$ and $\eta_{2,c}$ that are depicted in figure 5.3(b). The pseudocubic elastic constants $c_{13} = 132\,\text{GPa}$ and $c_{33} = 252\,\text{GPa}$ [163] result in the Poisson stress for bulk SRO depicted as gray line in (a). The Poisson stress contribution is very similar to the total equilibrium stress (red line) and determines the external stress (open symbols) by their sum according to equation (5.1). In the case of the thin film the equilibrium stress is given by the out-of-plane expansion in figure 5.2(c). In contrast to bulk material, the thin SRO film on the STO substrate exhibits a negative thermal expansion below the magnetic order temperature. This is mainly related to an additional substrate-induced Poisson stress contribution that originates from the in-plane expansion of the cubic STO unit cells, which is identical to the out-of-plane expansion above the phase transition at $105\,\text{K}$ depicted in figure 5.2(d). Due to the coherent growth of the SRO transducer on the STO substrate, the in-plane expansion of the unit cells directly attached to the substrate follows the expansion of the substrate, which changes the Poisson stress contribution with respect to bulk material. Therefore I assume a linear change of the in-plane expansion of the thin film from substrate-like at the interface to bulk-like at the surface. The assumed gradient of the substrate-induced deformation along the out-of-plane direction is indicated by the broadening of the SRO Bragg peak along q_z in figure 5.2(b). This assumption results in a Poisson stress that differs quantitatively from the Poisson stress for bulk material. The resulting external stress (open symbols) is well described by a Grüneisen model (black solid line) using the phononic and magnetic Grüneisen constants as for bulk material and the subsystem-separated heat capacity and the thin film.

Based on the extracted temperature-dependent out-of-plane external stress σ_3^{ext} of bulk SRO I determine the phononic and magnetic Grüneisen constant that is needed to analyse the picosecond strain response of the thin film. According to equation (5.1) the temperature-dependent subsystem contribution to the external stress $\sigma_{3,r}^{\text{ext}}$ relates linearly to the deposited energy density in the subsystem via its Grüneisen constant. The separation of the external stress into its subsystem contributions is based on the vanishing magnetic stress in the paramagnetic phase due to the

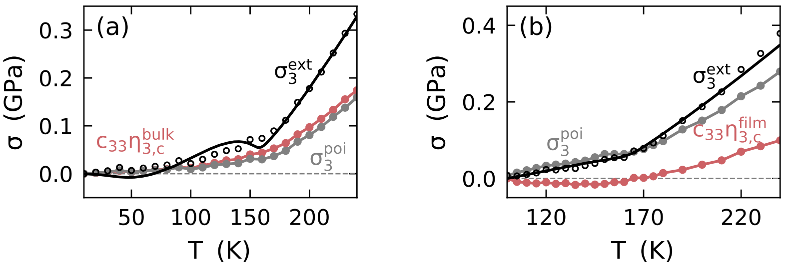

Figure 5.5: Separation of the temperature-dependent stress σ_3 driving the expansion in thermal equilibrium into the external σ_3^{ext} and Poisson σ_3^{poi} contribution. The thermal expansion along the orthogonal crystal directions determines the Poisson stress (gray lines). In bulk SRO (a) the Poisson stress is negligible below the Curie temperature, whereas in the thin film geometry (b) the in-plane expansion of the STO substrate enhances the Poisson contribution that causes the contractive total stress in the ferromagnetic phase. The solid black lines denote the Grüneisen model of the external stress using the Grüneisen constants of bulk material and the respective magnetic heat capacity contribution.

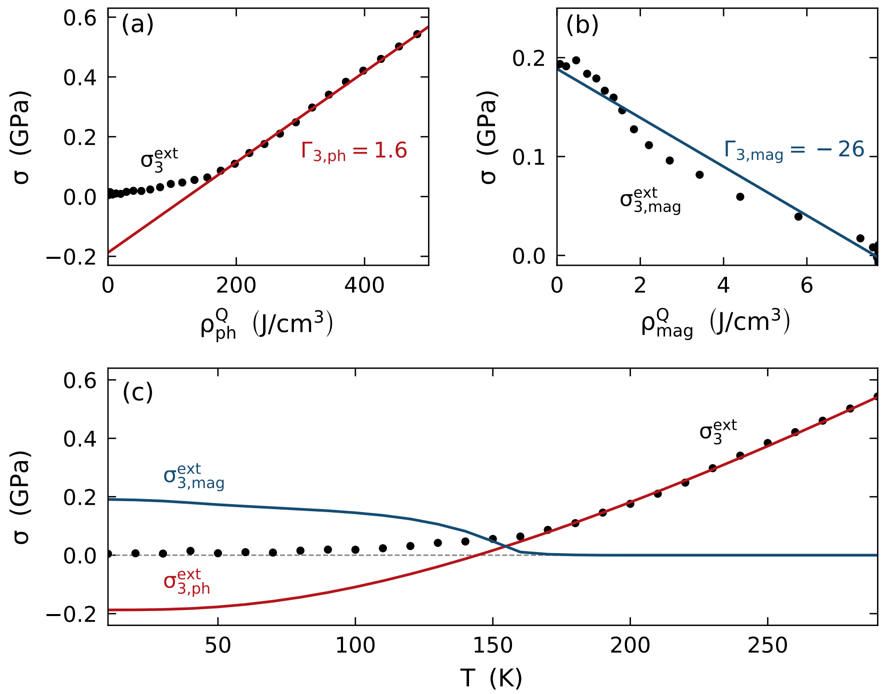

Figure 5.6: Determination of the Grüneisen constant of the phonons and the magnetic excitations. The linear dependence of the external stress on the energy density stored in the phonons above $T_{\text{demag}}^{\text{bulk}}$ (a) determines the phononic Grüneisen constant to $\Gamma_{3,\text{ph}} = 1.6$, which defines the phononic stress contribution (solid red line). The difference to the total stress corresponds to the magnetic stress contribution (b) that depends linearly on the energy density stored in the magnetic subsystem given by the respective heat capacity contribution (see figure 5.4(b)). The resulting magnetic Grüneisen constant of $\Gamma_{3,\text{mag}} = -26$ determines the temperature-dependent magnetic stress contribution. Its superposition with the phononic stress contribution gives the temperature-dependent total external stress (c).

finite magnetic energy reservoir. Figure 5.6 displays the determination of the Grüneisen constant of the phonons (a) and the magnetic excitations (b) by a linear dependence of the external stress contribution on the deposited energy density in the subsystem. The Grüneisen approach determines the corresponding temperature-dependent external stress contributions (c) that superimpose the total external stress. To reduce the number of free parameters, I simplify the following analysis by assuming that the electrons and the phonons exhibit the same Grüneisen parameter. This is a valid assumption, because the Grüneisen parameters of phonons and electrons typically have the same order of magnitude and the heating from 20 to 250 K deposits only 6% of the energy density to the electrons resulting in a negligible stress contribution‡. Since ultrafast experiments report a quasi-instantaneous electron-phonon coupling [26, 49] the assumption that most of the energy is stored in the phonons holds even on ultrafast timescales. In the following I will refer to the combined electron-phonon system as phonon system.

The non-magnetic heat capacity contribution in figure 5.4(b) relates the temperature-dependent external stress σ_3^{ext} to the deposited energy density in the phonons as shown in figure 5.6(a). Above $T_{\text{demag}}^{\text{bulk}} = 200\,\text{K}$, the total stress is exclusively caused by the phonons due to the vanishing magnetic heat capacity. Therefore a linear fit determines the phononic Grüneisen constant to $\Gamma_{3,\text{ph}} = 1.6$. The temperature-independent phononic Grüneisen constant defines the temperature-dependent

---

‡Below 30 K, the phononic and electronic heat capacity become comparable and a significant fraction of energy density is stored in the electrons inducing a non-negligible stress contribution. However, these low temperatures are not the scope of the ultrafast X-ray diffraction experiment.

expansive stress contribution of the phonons. The comparison of the phonon contribution (red solid line) and the total stress σ_3^{ext} below the magnetic order temperature indicates an additional stress contribution that originates from the magnetic system and vanishes with diminishing magnetic order. Figure 5.6(b) displays this magnetic stress $\sigma_{3,\text{mag}}^{\text{ext}}$ as function of the deposited energy density in the magnetic system given by the bulk magnetic heat capacity. The dependence on the magnetic energy density can be approximated by a linear function, which yields the magnetic Grüneisen constant along the out-of-plane direction of the thin film to $\Gamma_{3,\text{mag}} = -26$. The large negative magnetic Grüneisen constant denotes a large contractive stress induced by the small amount of energy density storable in the magnetic system (see figure 5.4(b)). The resulting magnetic stress contribution counteracts the expansive phonon stress and reduces the total stress in the ferromagnetic phase, which leads to the Invar behaviour in thermal equilibrium. Figure 5.6(c) shows the resulting temperature-dependent subsystem contributions to the external out-of-plane stress in the Grüneisen model. The separation of the total stress $\sigma_3^{\text{ext}}(T)$ into the subsystem contributions offers insight into the origin of the non-linear temperature dependence. Therefore the Grüneisen approach including the Grüneisen constants $\Gamma_{3,r}$ is a useful concept to analyse the induced lattice stress in magnetic materials.

5.2 Time-resolved reciprocal space mapping

In this section I describe the determination of the transient strain of the SRO transducer by a pump-probe experiment using ultrafast X-ray diffraction. I use the setup described in section 4.3 to determine the transient shift of the Bragg peak in reciprocal space by time-resolved reciprocal space mapping. Due to the partially transparent thin SRO film, the pump-probe experiment contains an additional delayed excitation that results in a double-pulse excitation scheme.

Figure 5.7 provides a schematic sketch of the pump-probe experiment. The near-infrared pump pulse is exclusively absorbed in the metallic SRO transducer. To first order this absorption is described by Lambert Beer's law. The temperature-independent optical penetration depth of the 800 nm pump pulse of 52 nm [26, 123, 164] exceeds the layer thickness. Therefore, a significant fraction of the pump pulse is transmitted through the transducer and enters the STO substrate. The back reflection at the substrate-copper interface at the sample holder leads to a second, delayed excitation. The non-adjustable delay between the two laser-excitations is determined by the optical propagation length through the substrate. Furthermore, the excitation fluence of the initial pump pulse and the second excitation are related by a constant factor, which depends on the transmission through the transducer and the reflectivity at the sample holder interface. In a pump-probe experiment the induced lattice response to both excitations is probed by an ultrashort X-ray pulse with a delay t relative to the first excitation. The ultrafast excitation condition in the thin film geometry induces exclusively out-of-plane strain dynamics as discussed in section 2.2.2. The laser-induced out-of-plane mean strain results in a shift of the SRO Bragg peak in reciprocal

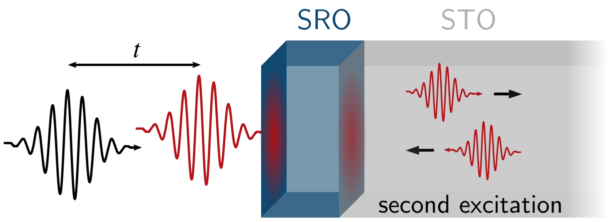

Figure 5.7: Schematic sketch of the pump-probe experiment including a double-pulse excitation. Since the optical penetration depth of the near-infrared pump pulse exceeds the thickness of the metallic SRO transducer, a fraction of the pump pulse is transmitted through the film. Its back-reflection at the sample holder leads to a second, delayed excitation. At a delay t with respect to the first excitation an ultrashort X-ray pulse probes the induced strain response.

space along the q_z-direction. Section 4.2 describes the two routines of reciprocal space mapping and reciprocal space slicing to quantitatively determine the shift of the Bragg peak. Since the Bragg peak of SRO is located on the left shoulder of the substrate peak, the quantitative determination of the shift is influenced by the non-constant background. Additionally, the shape of the Bragg peak in reciprocal space and the large diffraction angle lead to a geometrical scaling factor of $S \approx 10$ for the strain determination by reciprocal space slicing according to equation (4.10). This large scaling factor implies only small shifts of the Bragg peak on the position-sensitive area detector, which corresponds to a bad signal-to-noise ratio. Therefore I use time-resolved reciprocal space mapping to quantitatively determine the transient shift of the background-free Bragg peak of SRO by modelling the underlying substrate Bragg peak.

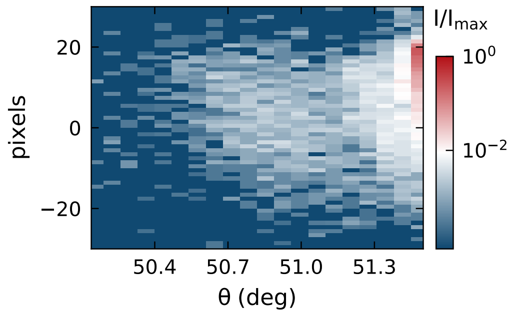

Figure 5.8: Results of a $\theta - 2\theta$-scan with a position-sensitive area detector at $250\,\mathrm{K}$. The variation of the diffraction angle $\theta = \alpha_{\mathrm{in}} = \alpha_{\mathrm{out}}$ provides the diffraction intensity as function of the angle and the detector pixels within the diffraction plane. While the centerpixel corresponds to a symmetric diffraction, the other pixels probe an asymmetric diffraction with $\alpha_{\mathrm{in}} \neq \alpha_{\mathrm{out}}$.

To determine the Bragg peak shift of SRO I map the reciprocal q_x-q_z-space around the $(004)_{\mathrm{c}}$ SRO Bragg peak by varying both the incident α_{in} and the diffraction angle α_{out} in a symmetric $\theta - 2\theta$-scan of 21 angle steps of $0.07°$ for the low fluence and 10 angle steps of $0.2°$ for the high fluence. With an integration time of $7\,\mathrm{s}$ the position-sensitive area detector determines the scattering intensity at each detector pixel within the diffraction plane. The resulting normalised intensity as a function of incident diffraction angles θ and detector pixels is shown in figure 5.8 at $250\,\mathrm{K}$ before the first excitation. Here, the intensity on the detector at the different angles is normalised to the total number of incident X-ray photons during the integration time, which is recorded by a reference detector behind the Montel optic [132]. The pixels within the diffraction plane correspond to different diffraction angles α_{out} as depicted in figure 4.2. The center pixel of the detector fulfils the condition $\alpha_{\mathrm{in}} = \alpha_{\mathrm{out}}$ and is determined by the intensity maximum of the SRO Bragg peak[§]. Associating the detector pixels with individual angles α_{out} depending on the pixel size and the sample-detector distance, the detected intensity depends on the angles α_{in} and α_{out}. This intensity distribution in angular space transforms by equation (4.7) to the reciprocal q_x-q_z-space. The non-linear transformation relates the intensity of a rectangular area in angular space to an intensity of a polygon in reciprocal space. The underlying change of the area is corrected by the Jacobian matrix of the transformation [133].

In order to obtain the projection on the q_z-direction yielding the out-of-plane lattice constant the intensity has to be mapped onto a rectangular q_x-q_z-grid. During this mapping the intensity of a rectangular grid cell is given by the intensity of the irregular shaped grid cell, which contains the center point of the new grid cell. The reciprocal space map with the orthogonal grid is shown in figure 5.9(b). Since the angle steps of the $\theta - 2\theta$ scan are relatively large, the dimension of the grid cells along q_z are limited to avoid numerical artefacts for the integration along the q_x-direction. The integration yields the projection on the q_z-axis (a) that displays the SRO Bragg peak at $6.32\,\mathrm{\AA}^{-1}$ on the shoulder of the substrate Bragg peak. Associating the finite substrate with a truncation rod I describe the substrate Bragg peak shoulder by a Lorentzian profile, which

---

[§] In the UDKM group the center pixel is usually determined by the maximum intensity provided by the substrate Bragg peak. In this experiment the STO Bragg peak is not fully recorded to reduce the measurement time. Therefore the global maximum in intensity does not correspond to the center of the substrate Bragg peak.

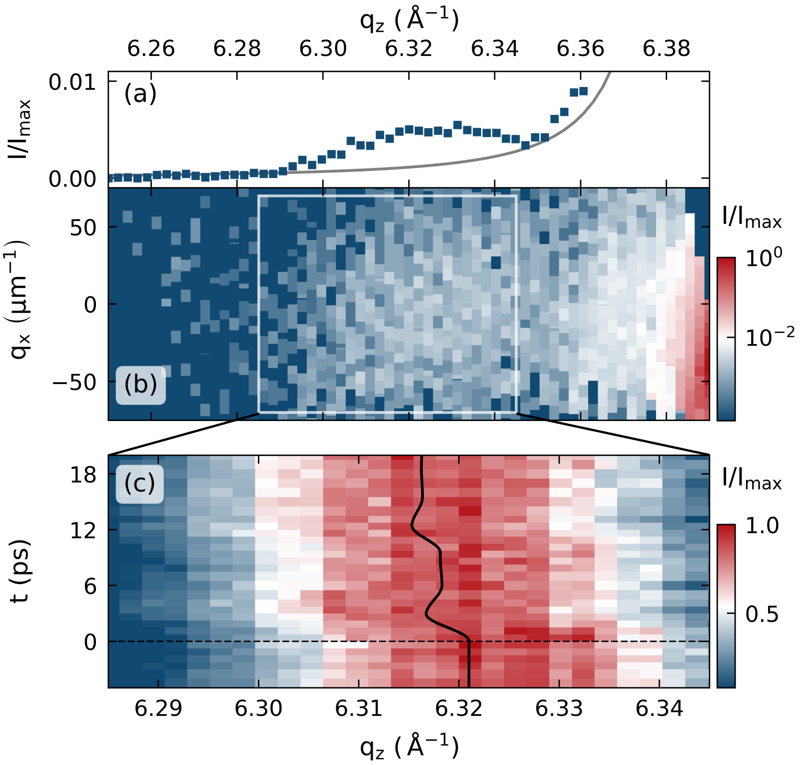

Figure 5.9: Determination of the time-resolved Bragg peak shift by reciprocal space mapping. The mapping of the diffraction intensity in figure 5.8 to a rectangular grid in the reciprocal q_x-q_z-space by equation (4.7) provides the reciprocal space map (b) before the first excitation. The integration along q_x yields the projection on the q_z-axis (a). The Bragg peak of SRO is given by the difference to the Lorentzian profile (gray line) that describes the diffraction from the substrate truncation rod. The time-dependent projection on the q_z-axis (c) displays the transient shift of the Bragg peak of SRO that determine the picosecond strain response by equation (4.8).

is fitted to the diffraction intensity below and above the Bragg peak of SRO. The resulting non-constant background of the SRO Bragg peak is depicted as gray solid line and defines the Bragg peak of SRO. The mean out-of-plane lattice constant of the thin film belongs to the position of the Bragg peak along q_z, which I determine by a center-of-mass analysis. This routine applied at each pump-probe time delay determines the time-resolved q_z-position of the Bragg peak of SRO. Figure 5.9(c) displays the time-dependent shift of the Bragg peak along the q_z-axis in the pump-probe experiment. The solid black line denotes the transient Bragg peak position modelled by the modular MATLAB library UDKM1DSIM. The shift of the Bragg peak to lower q_z-values for positive pump-probe delays ($t > 0$) displays the laser-induced expansion that is enhanced by the second excitation leading to an additional delayed shift of the Bragg peak to lower q_z-values.

5.3 Fluence-dependent saturation of the magnetic stress

In this section I investigate the influence of the saturation of the magnetic stress on the total laser-induced stress. Therefore I present the picosecond strain response of SRO at initial temperatures above and below T_C for two different excitation fluences. Under the condition of a saturated magnetic stress the strain response to the second excitation becomes temperature-independent. The saturation of the magnetic stress in the limit of high fluences qualitatively changes the temperature dependence of the laser-induced stress by the changing excitation of the magnetic system that becomes proportional to the integral of the remaining magnetic heat capacity.

The first part provides the modelling of the temperature-dependent picosecond strain response to the double-pulse excitation. The ultrafast equilibration of the subsystems results in a quasi-instantaneous laser-induced stress that drives a bipolar strain wave propagating into the substrate. The excitation of the magnetic subsystem provides an additional contractive stress that reduces the amplitude of the ultrafast expansion. In the second part I model the underlying temperature- and fluence-dependent total stress in a Grüneisen model assuming equilibrated subsystems. The Grüneisen model captures the qualitative change of the temperature dependence of the stress with increasing fluence. The extracted ultrafast temperature- and fluence-dependent magnetic stress relates this qualitative change to the saturation of the magnetic stress.

5.3.1 Reduced lattice stress in the ferromagnetic phase

In this section I describe the strain response of the SRO transducer to a double-pulse excitation. The shape of the transient strain is modelled by a linear-chain model of masses and springs and encodes a bipolar strain wave propagating into the substrate that is driven by a quasi-instantaneous tensile stress. The additional contractive stress provided by the magnetic excitations in the ferromagnetic phase reduces the total stress. Under the facilitating conditions of equilibrated subsystems a Grüneisen model captures well the resulting temperature-dependent amplitude of the bipolar strain wave and the ultrafast expansion.

In a first step I analyse the picosecond strain response at $250\,\mathrm{K}$. In the paramagnetic phase the laser-induced stress driving the strain response originates exclusively from the phonons due to the absence of a magnetic energy reservoir. Under this condition the rise time and the amplitude of the total ultrafast stress depend on the electron-phonon relaxation time and the phononic Grüneisen constant, respectively. Figure 5.10 depicts the transient mean strain of the SRO transducer at $250\,\mathrm{K}$ at an incident fluence of $F = 1.4\,\frac{\mathrm{mJ}}{\mathrm{cm}^2}$. The strain response to the double-pulse excitation is well described by a linear-chain model of masses and springs (solid line) that I calculate by the modular MATLAB library UDKM1DSIM [124]. The laser-induced stress translates into inserted spacer sticks (see section 3.3.2 driving a strain response according to the discretised inhomogeneous wave equation of the coupled harmonic oscillators. The mean displacement of the masses translates via dynamical X-ray diffraction theory to the shift of the SRO Bragg peak¶, which determines the lattice strain as in a diffraction experiment by equation (4.8).

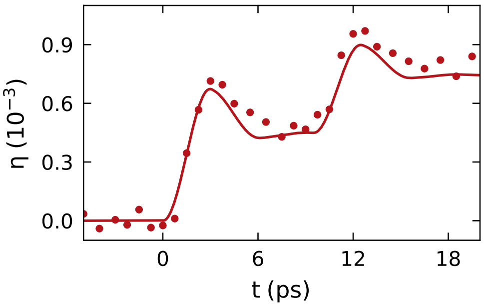

Figure 5.10: Picosecond strain response to a double-pulse excitation at $250\,\mathrm{K}$ with $F = 1.4\,\frac{\mathrm{mJ}}{\mathrm{cm}^2}$. The linear-chain model of the MATLAB library UDKM1DSIM [124] (solid line) describes the transient strain of the acoustic impedance-matched film-substrate system under the assumption of a quasi-instantaneous tensile stress.

In agreement with the literature [26, 49], the strain model assumes an electron-phonon coupling on the timescale of $100\,\mathrm{fs}$. Therefore, the deposition of energy by the pump pulse induces a quasi-instantaneous tensile stress. The unbalanced stress at the surface and the transducer-substrate interface drive a bipolar strain wave as depicted in figure 2.3 for the general case of a thin film on a transparent substrate. The superposition of the strain wave and the relaxation of the laser-induced stress to strain with sound velocity determine the transient mean strain of the SRO transducer. The propagation of the expansive part of the bipolar strain wave from the surface to

---

¶This includes the X-ray sensitivity function [165], which describes the dependence of a Bragg peak shift on the specific location of a delta-like strain along the sample depth.

the interface results in a maximum expansion of SRO 3 ps after the excitation according to the layer thickness $d = 19\,\text{nm}$ and the sound velocity $v = 6.31\,\frac{\text{nm}}{\text{ps}}$ [143]. The subsequent propagation of the expansive part into the substrate reduces the mean strain of SRO within the next 3 ps according to the spatial extension of the strain wave. The almost perfect acoustic impedance match of the SRO transducer and the STO substrate suppresses a reflection of the strain wave at the transducer-substrate interface and the strain wave enters completely the substrate. The remaining expansion as quasi-static elastic response to the laser-induced stress depends linearly on the total out-of-plane stress σ_3^{ext} by the elastic constant c_{33} and is $2/3$ of the maximum expansion [49]. At a pump-probe delay of 9.6 ps the second excitation induces an additional stress that drives a bipolar strain wave superimposing with the ultrafast expansion induced by the first excitation. Since the remaining expansion after the strain wave has propagated into the substrate depends linear on the stress, the strain from 6 to 9 ps and from 16 to 20 ps reveals the laser-induced stress by the first and the second excitation, respectively. The modelling of the ultrafast expansion calibrates the absorbed fluence to one third of the incident fluence and the ratio of the excitation fluences of the first and the second pulse to $5/3$. The further analysis of the strain response for different initial sample temperatures is facilitated by the approximately temperature-independent absorbed fluence and fluence ratio of the two excitations. The constant deposited energy density originates from the temperature-independent reflection of the pump pulse from the surface of the sample and transmission through the transducer due to the temperature-independent dielectric function of SRO [26, 164].

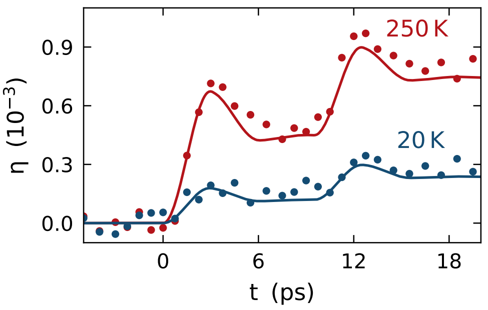

Figure 5.11: Comparison of the strain response at 20 and 250 K with the same excitation fluence of $F = 1.4\,\frac{\text{mJ}}{\text{cm}^2}$. The reduced amplitude and the identical temporal shape at the initial sample temperature of 20 K indicates a contractive magnetic stress rising on the electron-phonon coupling timescale in the ferromagnetic phase.

In the second step I extend the modelling of the picosecond strain response to the ferromagnetic phase below $T_{\text{C}} = 150\,\text{K}$. Below the Curie temperature, the arising magnetic order provides an additional energy reservoir. According to the negative Grüneisen constant $\Gamma_{\text{mag}} = -26$ the excitation of the magnetic subsystem induces a contractive stress that counteracts the tensile phonon stress and reduces the total stress σ_3^{ext}. The excitation of the magnetic subsystem by the coupling to the laser-excited electrons determines the rise time of the additional stress contribution. In figure 5.11 I compare the strain response at 20 and 250 K for an incident fluence of $F = 1.4\,\frac{\text{mJ}}{\text{cm}^2}$. In the ferromagnetic phase the ultrafast expansion and the amplitude of the driven bipolar strain wave are significantly reduced. However, the temporal shape of the transient strain turns out to be temperature-independent, which indicates a quasi-instantaneous tensile total stress including the magnetic stress contribution. The temperature-independent quasi-instantaneous stress indicates an ultrafast equilibration of electrons, phonons and magnetic excitations in agreement with a previous investigation of the magnetic stress in SRO [26]. In this publication the authors observe a temperature-independent phase of the time-resolved intensity oscillation of the Bragg peak of a superlattice consisting of SRO and STO layers. The sub-picosecond demagnetisation detected by the magneto-optical Kerr effect [158] corroborates the underlying assumption of a sub-picosecond excitation of the magnetic system by the coupling to the laser-excited electrons. The assumption of an ultrafast equilibration of the subsystems implies to a time-independent distribution of the laser-deposited energy density between the subsystems identical to equilibrium.

In the Grüneisen model the temperature-dependent out-of-plane lattice stress results in:

$$\sigma_3^{\mathrm{ext}}(T,z) = \Gamma_{3,\mathrm{ph}} \int_{T}^{T+\Delta T(z)} C_{\mathrm{ph}}(T')\,\mathrm{d}T' + \Gamma_{3,\mathrm{mag}} \int_{T}^{T+\Delta T(z)} C_{\mathrm{mag}}(T')\,\mathrm{d}T' \,. \tag{5.2}$$

Here, $\Delta T(z)$ denotes the laser-induced temperature increase, which is defined by the total heat capacity C_{tot} and the absorbed energy $Q_{\mathrm{abs}}(z)$ via the condition $Q_{\mathrm{abs}}(z) = \int_T^{T+\Delta T(z)} C_{\mathrm{tot}}(T')\mathrm{d}T'$. In consideration of the heat capacities of the thin film from section 5.1.2 and the Grüneisen constants of the phonons $\Gamma_{3,\mathrm{ph}} = 1.6$ and the magnetic excitations $\Gamma_{3,\mathrm{mag}} = -26$ the Grüneisen model (5.2) defines the temperature- and depth-dependent total stress. I use this stress to model the strain response at $20\,\mathrm{K}$ in a linear-chain model of masses and springs using the MATLAB library UDKM1DSIM depicted by the blue solid line in figure 5.11.

In the following paragraph I describe the strain response at different initial sample temperatures set by a closed-cycle cryostat for two excitation fluences 1.4 and $6.3\,\frac{\mathrm{mJ}}{\mathrm{cm}^2}$. Figures 5.12 (a) and (b) summarise the temperature-dependent strain measured by time-resolved reciprocal space mapping (dots) and modelled by the MATLAB library UDKM1DSIM (solid lines)[‖] for the low and the high fluence, respectively. The excitation fluence deposits temperature-independently the same amount of energy to the transducer due to the temperature-independent dielectric function of SRO. Therefore the temperature dependence of the total laser-induced stress σ_3^{ext} is exclusively caused by the excitation of the magnetic system and the associated contractive stress in the ferromagnetic phase. For both fluences the excitation of the magnetic subsystem below T_{C} reduces the total stress. However, the temperature dependence differs for both fluences. In case of the high fluence of $6.3\,\frac{\mathrm{mJ}}{\mathrm{cm}^2}$ the expansion after both the first and the second excitation decreases slightly below the Curie temperature. In contrast, the expansion after the first and the second excitation decreases step-like at the phase transition in case of the low fluence of $1.4\,\frac{\mathrm{mJ}}{\mathrm{cm}^2}$. Additionally, the expansion after the first and the second excitation displays a different temperature dependence, which leads to a larger expansion driven by the second pulse than by the first pulse at $140\,\mathrm{K}$. The temperature-dependent stress of the Grüneisen model (5.2) results in the modelled strain response (solid lines) in a linear-chain model of masses and springs using one set of parameters calibrated in the paramagnetic phase. The modelled strain response captures the temperature dependence of the laser-induced expansion. In the following section I extract from the ultrafast expansion the temperature-dependent lattice stress induced by the first and the second pump pulse, respectively. The stress induced by the second pump pulse is given by the difference between the strain after the second and the first excitation due to the linear elastic response of SRO.

5.3.2 The temperature- and fluence-dependent magnetic stress

In this section I relate the fluence-dependent temperature dependence of the total laser-induced stress to the saturation of the magnetic stress. The extraction of the ultrafast magnetic stress by a Grüneisen model rationalises the temperature-dependent ultrafast expansion and exemplifies the effect of the saturation on the total stress. The saturation of the magnetic stress is probed by the temperature-independent stress induced by the second pulse exciting the fully demagnetised sample. In the limit of high fluences, which transiently heat above the phase transition, the magnetic stress is proportional to the integral of the remaining heat capacity. In contrast, in the low fluence limit the magnetic stress follows the magnetic heat capacity.

The temperature- and fluence-dependent total laser-induced stress σ_3^{ext} relates linearly to the ultrafast expansion remaining after the bipolar strain wave has propagated into the substrate.

[‖] The following analysis is restricted to the total laser-induced stress due to the ultrafast equilibration of the subsystems that results in a temperature-independent shape of the driven strain wave. Therefore I measure at some initial sample temperatures only the ultrafast expansion depending linearly on the stress.

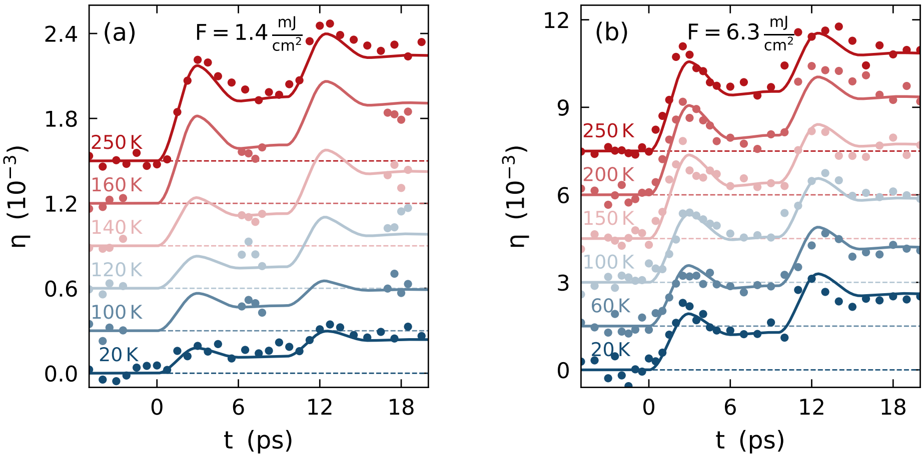

Figure 5.12: Temperature-dependent strain response to a double-pulse excitation with an incident fluence of 1.4 (a) and 6.3 $\frac{\mathrm{mJ}}{\mathrm{cm}^2}$ (b). The dots denote the measured strain from time-resolved reciprocal space mapping and the solid lines result from the linear-chain model of the MATLAB library UDKM1DSIM [124] using the temperature-dependent stress of the Grüneisen model (5.2). The laser-induced lattice response for the two fluences show a qualitative difference in the temperature dependence of both the expansion after the first and the second excitation.

Therefore I use the strain from 6 to 9 ps and 16 to 20 ps in figure 5.12 to extract the laser-induced stress. The resulting temperature-dependent, laser-induced stress is shown in figure 5.13(a) and (c) for the small and the high fluence, respectively. Here, the blue points denote the stress induced by the first excitation and the red squares denote the stress induced by the second excitation. With non-zero magnetic heat capacity below $T_{\text{demag}}^{\text{film}} = 170\,\text{K}$ the total stress decreases and the different temperature dependencies are rationalised in the following paragraphs. This analysis is supported by a Grüneisen model that captures the temperature-dependent stress induced by both excitations for both fluences and simplifies in the limit of high and low fluences.

In the case of the small fluence of $F = 1.4\,\frac{\mathrm{mJ}}{\mathrm{cm}^2}$, the total stress induced by the first and the second pulse shows a step-like decrease at 170 and 135 K, respectively. This shifted step-like temperature dependence is rationalised by the sketch of the excitation of the magnetic subsystem in figure 5.13(b). The blue and the red arrows describe the laser-induced temperature increase relative to the magnetic heat capacity $C_{\text{mag}}^{\text{film}}$ induced by the first and the second pulse, respectively. At low temperatures the magnetic stress is not saturated, because both pulses together do not heat above the phase transition. Under this condition the magnetic excitations cause a reduced total stress for both excitations. Since the magnetic heat capacity exhibits a peak at the phase transition, the maximum fraction of energy density is transferred to the magnetic system, when the laser pulse transiently heats up to the transition temperature. The enhanced energy density deposited to the magnetic system corresponds to a maximal magnetic but a minimal total stress. Therefore the initial sample temperature corresponding to this full demagnetisation defines the lower bound of the step-like change of the total stress. With increasing temperature the magnetic stress becomes saturated and the energy density storable to the magnetic excitations decreases. With vanishing magnetic heat capacity at 170 K the magnetic stress contribution vanishes and the total stress is maximised and becomes temperature-independent. This analysis of the temperature dependence relates the width of the step-like change to the laser-induced temperature increase by the first laser pulse. It increases the effective temperature of the SRO film before the second excitation and shifts the step-like change of the total stress induced by the second pulse to 135 K. The observed temperature dependence is well described by the Grüneisen model (5.2) depicted by the solid lines for the homogeneous excitation of the layer exceeding the optical penetration depth.

In the limit of an infinitesimal deposited energy Q_{dep} inducing a sufficiently small temperature step $\Delta T = \frac{Q_{\text{dep}}}{C_{\text{tot}}}$, the temperature-dependent stress induced by the first excitation results in

$$\sigma_3^{\text{low}}(T) = \frac{Q_{\text{dep}}}{V}\left(\frac{\Gamma_{\text{mag},3}C_{\text{mag}}(T)+\Gamma_{\text{ph},3}C_{\text{ph}}(T)}{C_{\text{tot}}(T)}\right) . \tag{5.3}$$

Here, the deposited energy density in the subsystem r is given by $\rho_r^Q = C_r \cdot \Delta T/V$**. Since the phononic heat capacity contribution exhibits a pronounced temperature dependence in the investigated temperature range, the total stress according to equation (5.3) inherits the temperature dependence of both the phononic and magnetic heat capacity. However, around the phase transition the phononic heat capacity is approximately temperature-independent and the laser-induced stress becomes proportional to the magnetic heat capacity. In this limit the magnetic heat capacity provides the step-like change of the total stress as already observable for $1.4\,\frac{\text{mJ}}{\text{cm}^2}$.

Increasing the fluence and thus the laser-induced temperature change qualitatively modifies the temperature dependence of the stress induced by the first and the second pulse. In the case of the fluence of $F = 6.3\,\frac{\text{mJ}}{\text{cm}^2}$, the stress induced by the first pulse increases continuously with temperature up to the Curie temperature, whereas the stress induced by the second pulse shows no temperature dependence at all. Since the same amount of energy is deposited at each initial sample temperature the temperature-independent stress indicates the absence of a magnetic stress contribution for initial sample temperatures in the ferromagnetic phase. This reveals the saturation of the magnetic stress by the first excitation for all temperatures, which is equivalent to a transient heating above the phase transition. The underlying excitation of the magnetic system in the double-pulse excitation scheme is sketched in figure 5.13(d). The arrows denote the laser-induced temperature increase relative to the magnetic heat capacity for different initial sample temperatures. Irrespective of the temperature, the first pump pulse (blue arrow) transiently heats above the Curie temperature and deposits the maximum amount of energy to the magnetic system given by the temperature-dependent integral of the magnetic heat capacity. Therefore the temperature-dependent integral of the remaining magnetic heat capacity determines the magnetic stress contribution that counteracts the tensile phonon stress. Under the assumption of a homogeneous excitation, the temperature-dependent stress induced by the first pulse results in

$$\sigma_3^{\text{high}}(T) = \Gamma_{\text{ph},3}\rho_{\text{dep}}^Q + \left(\Gamma_{\text{mag},3} - \Gamma_{\text{ph},3}\right)\rho_{\text{mag}}^Q(T) . \tag{5.4}$$

Due to the conservation of energy, the energy density $\rho_{\text{mag}}^Q(T) = \int_T^{170\,\text{K}} C_{\text{mag}}^{\text{film}}(T')\text{d}T'$ deposited to the magnetic system reduces the fraction of the total deposited energy density ρ_{dep}^Q deposited in the phonons. In total, the excitation of the magnetic system results in a decreased total stress due to the reduced energy density stored in the phonons and the additional contractive magnetic stress contribution according to the negative magnetic Grüneisen constant. The saturation of the magnetic stress by the first pump pulse causes an exclusive excitation of phonons by the second pump pulse leading to the observed temperature-independent stress. The solid lines in figure 5.13(c) represents the Grüneisen model of the temperature-dependent stress according to equation (5.4). Above $T_{\text{demag}}^{\text{film}} = 170\,\text{K}$, the stress induced by the second excitation is scaled by the fluence factor of 0.6 relative to the maximum stress induced by the first excitation. The good agreement between the measurement and the model demonstrates the suitability of the Grüneisen model to describe the ultrafast stress in the magnetic metal SRO.

In figure 5.13 the comparison of the temperature-dependent stress for the two fluences displays a fluence dependence that originates from the laser-induced saturation of the magnetic stress. Under the facilitating conditions of homogeneous excitation of the transducer and ultrafast equilibrated

---

**Note, deviations from the approximation by equation (5.3) become larger with decreasing heat capacity at low temperatures, because even small excitations induce large temperature steps including a significant variation of the heat capacity contributions.

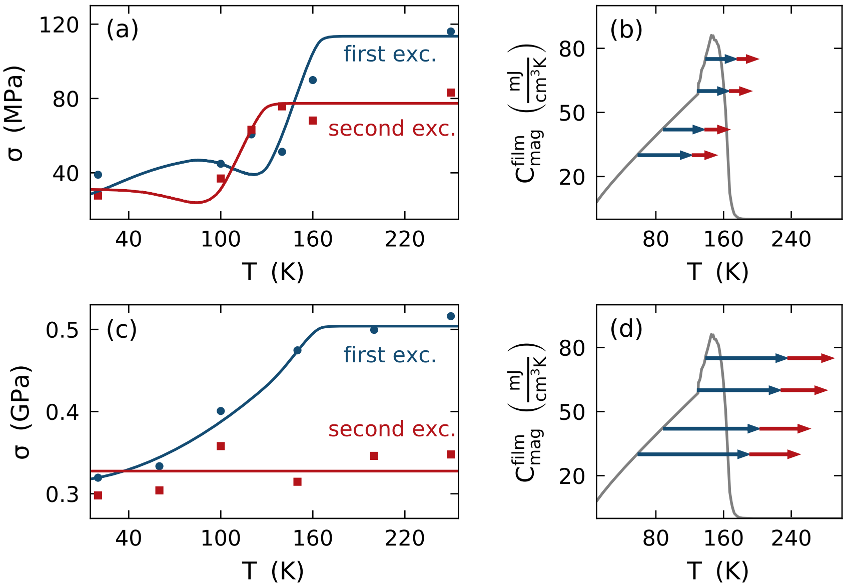

Figure 5.13: Extracted temperature-dependent stress induced by the first and the second excitation for both fluences. (a,c) The blue dots and red squares denote the extracted laser-induced stress from the measurements in figure 5.12 for the first and the second excitation, respectively. The solid lines relate to the Grüneisen model (5.2) describing well the temperature dependence. The schematic sketch of the excitation of the magnetic subsystem by the laser-induced temperature increase (arrows) in comparison to the magnetic heat capacity (b,d) rationalises the fluence-dependent temperature dependence of the total stress.

subsystems, the Grüneisen model captures this fluence dependence. In figure 5.14 I present the temperature-dependent total and magnetic stress for different fluences modelled by the Grüneisen approach. The temperature- and fluence-dependent magnetic stress exemplifies the influence of the magnetic stress on the dependencies of the total stress. The Grüneisen model describes the crossover from the low-fluence to the high-fluence temperature dependence of the total stress in panel (a). In the limit of infinitesimal excitations the total stress according to equation (5.3) (gray solid line) decreases in a step-like fashion slightly above the phase transition and exhibits a minimum at the Curie temperature corresponding to a maximum in the magnetic stress contribution depicted in panel (b). This maximum corresponds to an enhanced amount of deposited energy density due to the maximum of the magnetic heat capacity at the phase transition. Since the deposited energy density to the magnetic excitations depends also on the phononic heat capacity, the temperature-dependent magnetic stress is not exclusively given by the magnetic heat capacity. Below 50 K, the different temperature dependencies of the phononic and magnetic heat capacity contribution approximated by $\sim T^3$ and $\sim T^{\frac{1}{2}}$ enhances the fraction of energy density stored to the magnetic system that leads to an increasing magnetic stress. Under the assumption of a constant phononic heat capacity in the Dulong-Petit limit the magnetic stress contribution is indeed proportional to the magnetic heat capacity as depicted by the gray dashed line.

With increasing fluence the pump pulse transiently demagnetises the SRO transducer for lower initial sample temperatures, thus the corresponding minimum in the total stress shifts to lower initial sample temperatures and the step-like change of the stress around the Curie temperature is broadened. Starting from a fluence of $F = 3.5\,\frac{\mathrm{mJ}}{\mathrm{cm}^2}$, the first excitation heats above the phase transition and saturates the magnetic stress independently of the initial sample temperature. The corresponding temperature-dependent magnetic stress contribution becomes maximal and stays constant with further increase of the fluence. In this case the magnetic stress is proportional to the integral of the remaining magnetic heat capacity described by the squared magnetisation

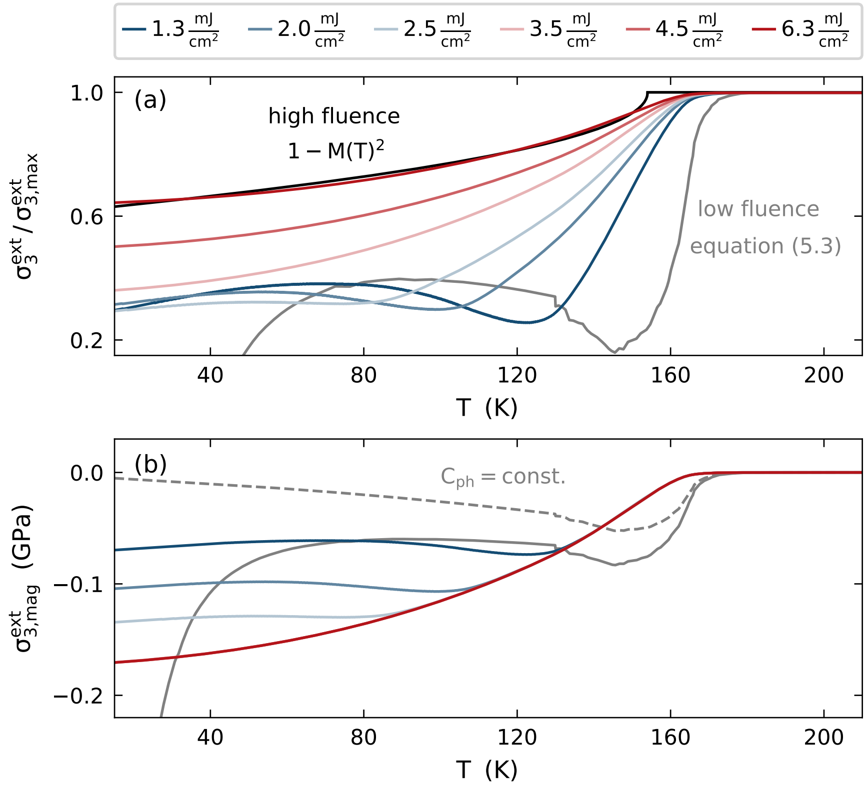

Figure 5.14: Crossover from the low-fluence to the high-fluence temperature dependence of the total and magnetic stress. The Grüneisen model of the ultrafast stress (5.2) determines the temperature-dependent total (a) and magnetic stress (b) for different fluences. In the limit of infinitesimal excitations and a temperature-independent phononic heat capacity the magnetic stress is given by the magnetic heat capacity (gray dashed line). However, the temperature-dependent phononic heat capacity influences the energy density deposited to the magnetic excitations and thus it changes the magnetic and the total stress (gray solid line). In the limit of high fluences the temperature dependence of the total stress is given by the integral of the remaining magnetic heat capacity following $1-M(T)^2$ (black solid line).

$M(T)^2$ in regards to the molecular field approximation. This dependence is in agreement with the temperature dependence of the spontaneous magnetostriction in equilibrium [166] due to the ultrafast equilibration of the phonons and the magnetic excitations. The dependence of the magnetic stress results in a total stress described by $1-M(T)^2$ as demonstrated by the black solid line in figure 5.14(a). However, with increasing fluence the additional energy is exclusively stored in the phonons. The decreasing fraction of energy density stored in the magnetic excitation reduces the relative decrease of the total stress in the ferromagnetic phase.

In the case of SRO, the analysis of the laser-induced stress is facilitated by the ultrafast equilibration of the subsystems that results in a time-independent energy distribution as in equilibrium. Therefore the equilibrium temperature-dependent external stress in figure 5.5 describes the ultrafast stress according to the laser-induced temperature increase given by the total heat capacity. However, the application of the Grüneisen model reveals the origin of the temperature and fluence dependence of the ultrafast stress by the separation into the phononic and magnetic contribution. This exemplifies the Grüneisen concept to be a useful approach for analysing picosecond strain dynamics and to investigate the role of the magnetic excitations. In the next chapter I extend the Grüneisen approach to a laser-induced non-equilibrium of the subsystems.

CHAPTER SIX

SPATIO-TEMPORAL MAGNETIC STRESS IN THE RARE-EARTH DYSPROSIUM

In this chapter I examine the question how the excitation of the magnetic subsystem on two timescales in an inhomogeneously excited transducer influences the total stress and the driven strain pulses. I focus especially on the influence of the spatial-dependent saturation of the magnetic stress on the transient expansion of the transducer and the strain pulses. Therefore I present the analysis of the temperature- and fluence-dependent strain response in a heterostructure that consists essentially of an optically excited dysprosium transducer and a buried niobium detection layer. Below the Néel temperature, the excitation of the antiferromagnetically ordered spin system in dysprosium results in a contractive stress that even dominates over the tensile phonon stress. The inhomogeneous excitation of the transducer and the laser-induced non-equilibrium between the phonons and the magnetic excitations cause an explicit spatial and temporal dependence of the total stress in dysprosium that is captured by a Grüneisen model.

This chapter is based on our recent publication that is dedicated to the unconventional picosecond strain pulses that are triggered in a rare-earth transducer [29]. In that publication I conducted the modelling of the strain response using the Grüneisen concept in cooperation with my colleague Alexander von Reppert, who together with Jan-Etienne Pudell conducted the X-ray diffraction measurements. This chapter extends the publication by the simulated heat transport providing a first attempt to model the remagnetisation of the laser-excited dysprosium and an analysis of the strain response to a double-pulse excitation. In the first section I determine the Grüneisen constant of the phonons and the magnetic system using the subsystem-separated heat capacity and the equilibrium expansion of the hexagonal unit cell. The second section describes the modelling of the subsystem-separated spatio-temporal stress in the heterostructure by the Grüneisen approach. The excitation of the magnetic subsystem on two timescales reduces the energy density stored in the phonons and is assumed to share the spatial profile of the phononic stress, which is calibrated in the paramagnetic phase. In the third section I present the modelled strain response including unconventional strain pulses driven by the complex total spatio-temporal stress. The depth-dependent saturation of the magnetic stress rationalises the temperature- and fluence-dependent strain response. The last section presents the application of the Grüneisen model to a variable double-pulse excitation scheme wherein the expansion driven by the second pulse verifies the saturation of the magnetic stress at the top side of the dysprosium layer.

6.1 Equilibrium properties of dysprosium

This section summarises the equilibrium magnetic and thermodynamic properties of the rare-earth metal dysprosium that acts as a transducer in the investigated heterostructure. Dysprosium exhibits large magnetic moments originating from the localised $4f$-electrons that order antiferromagnetically below the Néel temperature $T_\mathrm{N} = 180\,\mathrm{K}$ and ferromagnetically below the Curie

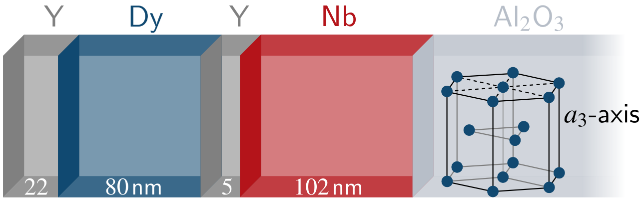

Figure 6.1: Schematic sketch of the investigated crystalline heterostructure. The 80 nm-thick dysprosium layer (Dy) between the two yttrium (Y) layers serves as an optically excited magnetic transducer. The hexagonal-closed packed crystal structure of these materials is exemplary sketched in the inset. The buried body-centred cubic 102 nm thick niobium layer (Nb) is used as a detection layer, which also enables the crystalline growth on the sapphire substrate (Al_2O_3).

temperature $T_C = 85\,K$ (see review by *Koehler* [167]). The magnetic order provides an additional energy reservoir and the magnetic excitations result in a pronounced negative thermal expansion along the a_3-axis of the hexagonal unit cell. The negative thermal expansion indicates a contractive magnetic stress contribution that dominates over the tensile stress due to anharmonic phonon-phonon interactions. The magnetic stress arising from the excitation of the magnetic order is well described by an anisotropic Grüneisen constant of $\Gamma_{3,\mathrm{mag}} = -2.9$ along the a_3-axis of the unit cell pointing along the out-of-plane direction in the sample structure.

In the following paragraphs I summarise the structural properties of the heterostructure supported by a X-ray diffraction measurement that provides the lattice constants of the materials by the separated Bragg peaks. The investigated sample structure is sketched in figure 6.1. The crystalline heterostructure consists of various layers and different materials. The (0001)-oriented dysprosium (Dy) transducer (80 nm) is located between two (0001)-oriented yttrium (Y) layers (22 nm and 5 nm). These materials exhibit a hexagonal-closed packed (hcp) crystal structure that is depicted in the inset of figure 6.1. The hexagonal unit cells in these layers are oriented with the a_3-axis pointing out-of-plane and the a_1-axis within the basal plane corresponds to the in-plane lattice constant. The buried body-centred cubic (110)-grown niobium (Nb) detection layer (102 nm) ensures the crystalline growth on the hcp-$(11-20)$ sapphire (Al_2O_3) substrate.

Reciprocal space mapping with a convergent beam and a X-ray area detector [128] provides additional information on the individual out-of-plane lattice constants of the materials and the crystalline quality of the layers. In a co-planar diffraction geometry a symmetric θ-2θ scan maps the reciprocal q_x-q_z space. The reciprocal space map in figure 6.2(b) measured by a microfocus Cu-K_α X-ray source displays the well separated Bragg peaks of the different materials as diffraction maxima. The Bragg peaks of dysprosium (0002), yttrium (0002) and niobium (110) at $q_z = 2.22\,Å^{-1}$, $2.07\,Å^{-1}$ and $2.7\,Å^{-1}$ show an elongation along q_x, respectively. This broadening of the Bragg peaks along q_x indicates a mosaicity of the layers where the tilting of the crystallites leads to an asymmetric diffraction relative to the sample surface so that $\alpha_{\mathrm{in}} \neq \alpha_{\mathrm{out}}$. This corresponds to an imperfect crystal structure of these layers. In contrast, the sharp Bragg peak of the sapphire substrate exhibits the instrument resolution area of the setup [128] indicating the well-defined periodicity of the crystal structure. Integrating the reciprocal space map along q_x yields the projected diffraction intensity on the q_z-axis, which encodes the out-of-plane lattice constants a_3 of the different materials by the position of the Bragg peaks along $q_z = \frac{2\pi \cdot m}{a_3}$*.

The equilibrium thermal expansion of the materials in the heterostructure can be used to determine the Grüneisen constants and thus yields an important reference for the interpretation of the ultrafast pump-probe experiments. The out-of-plane expansion results in a peak-shift of the material-specific Bragg peak along q_z. Figures 6.2(c) and (d) display the temperature-dependent peak shift of dysprosium and niobium, respectively. The black dashed lines denote the Bragg

---

*The q_z direction only describes the out-of-plane direction in regards to the choice of the reciprocal coordinate system used in this thesis, which is introduced in section 4.1.

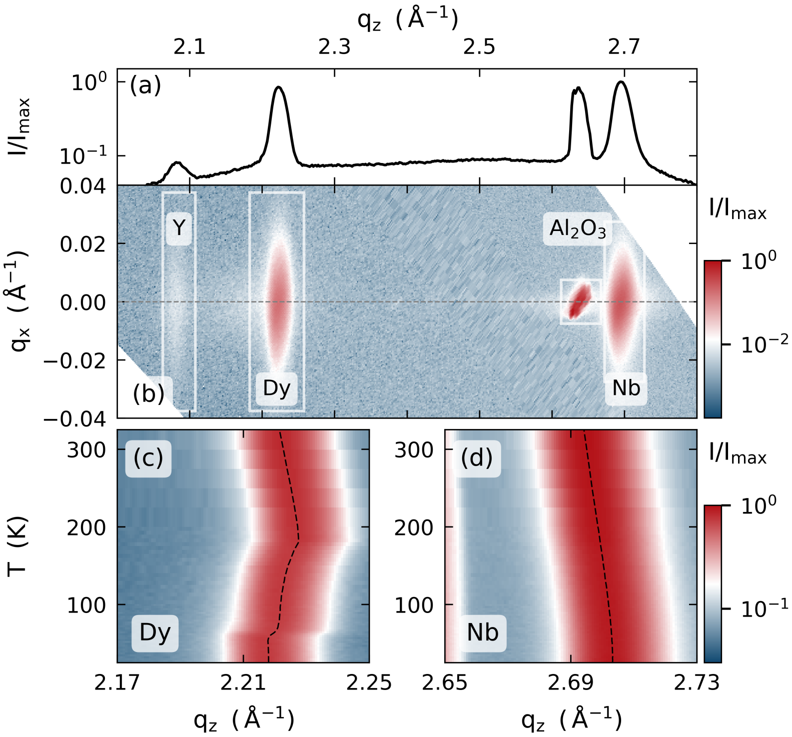

Figure 6.2: Characterisation of the investigated heterostructure by X-ray diffraction. The reciprocal space map (b) displays the Bragg peaks of the yttrium (Y), dysprosium (Dy) and niobium (Nb) layers and the sapphire (Al_2O_3) substrate as intensity maxima. The integration along q_x yields the projection on q_z (a), which determines the out-of-plane lattice constant. The thermal expansion of dysprosium (c) and niobium (d) corresponds to a shift of the Bragg peak along the q_z direction. While niobium exhibits the common positive thermal expansion, dysprosium shows a negative thermal expansion below $180\,K$. (Adopted from [29])

peak position that determines the out-of-plane lattice constant. The niobium Bragg peak shifts monotonously to smaller q_z, which corresponds to the common positive thermal expansion that originates from anharmonic phonon-phonon interactions. In contrast, the temperature-dependent expansion of dysprosium is non-continuous including a step-like change at $40\,K$ and a change from negative thermal expansion to positive thermal expansion at $180\,K$. The unusual thermal expansion of dysprosium hints at an additional contractive magnetic stress arising at low temperatures.

6.1.1 Magnetism-induced negative thermal expansion

This section relates the negative thermal expansion of dysprosium in the range between 40 and $180\,K$ in figure 6.2(c) to the magnetism of the rare-earth metal. The giant magnetostriction results from a pronounced coupling of the magnetism to the lattice by exchange-striction and spin-orbit coupling. These mechanisms originate from the indirect Rudermann-Kittel-Kasuya-Yosida (RKKY) interaction [168–170] and the anisotropic 4f orbitals providing the magnetic moments.

Elemental bulk dysprosium exhibits a large magnetic moment of $10.6\,\mu_B$ per atom, which mainly originates from the partially filled 4f orbitals and lies within the basal plane of the hexagonal unit cell [171]. According to Hund's rules the nine 4f electrons contribute $10\,\mu_B$ to the total magnetic moment [45, p. 673] whereas the remaining moment is associated with the spin polarisation of the itinerant 5d6s conduction band electrons [172]. The 4f orbitals are localised at the nucleus and their probability density decays rapidly with interatomic distance [173]. Therefore there is no direct overlap between the electronic wave functions of adjacent lattice sites and the direct exchange interaction of these moments is inhibited. Instead, the large 4f magnetic moments are coupled indirectly by the itinerant 5d6s conduction band electrons via the RKKY interaction [174, p. 200ff], which includes an intra-atomic coupling between the 4f- and 5d6s-magnetic moments and an inter-atomic coupling of the spin polarised delocalised conduction band electrons. This coupling of the magnetic moments of adjacent lattice sites is described by a Heisenberg Hamiltonian including the exchange parameter $J_{i,j}^{\mathrm{RKKY}}$ [174, p. 207]. The corresponding exchange energy provides a minimum in the Free energy, which favours a collective magnetic order at low temperatures. In bulk dysprosium the magnetic moments order ferromagnetically (FM) below the Curie temperature $T_\mathrm{C}^\mathrm{bulk} \approx 85\,\mathrm{K}$ [167] with the easy axis along the a_1-axis of the unit cell [171]. Growing dysprosium as thin film on yttrium reduces the Curie temperature to $T_\mathrm{C} \approx 60\,\mathrm{K}$, which corresponds to a stabilisation of the anti-ferromagnetic order [175, 176]. Above the Curie temperature dysprosium becomes antiferromagnetic (AFM) up to the Néel temperature of $T_\mathrm{N} \approx 180\,\mathrm{K}$ [167]. The antiferromagnetically ordered magnetic moments form a helix with a finite angle between the magnetic moments of neighbouring unit cells along the a_3-axis. This rotation angle of the helix increases with increasing temperature. The helical order arises from an interplay of nearest-neighbour and next-nearest-neighbour interaction and is typical for the class of the rare-earth metals [177, p. 99]. Heating above the Néel temperature finally disturbs the long-range magnetic order and dysprosium becomes paramagnetic (PM).

These magnetic phase transitions are accompanied by a change of the thermal expansion of dysprosium. At low temperatures, dysprosium is orthorhombic with three independent lattice constants $a_{1,\mathrm{o}} = 3.592\,\mathrm{Å}$, $a_{2,\mathrm{o}} = 6.188\,\mathrm{Å}$ and $a_{3,\mathrm{o}} = 5.686\,\mathrm{Å}$ at 90 K [178] (see figure 6.3(b)) under the condition of $a_{2,\mathrm{o}} < \sqrt{3}a_{1,\mathrm{o}}$ [179]. At the Curie temperature $T_\mathrm{C}^\mathrm{bulk} \approx 90\,\mathrm{K}$, dysprosium undergoes a first order structural phase transition, which results in a hexagonal closed-packed crystal structure ($a_{2,\mathrm{hcp}} = \sqrt{3}a_{1,\mathrm{hcp}}$) with the lattice constants $a_{1,\mathrm{hcp}} = 3.5903\,\mathrm{Å}$ and $c_{3,\mathrm{hcp}} = 5.6475\,\mathrm{Å}$ [180]. The structural phase transition corresponds to a step-like decrease of the lattice constant $a_{1,\mathrm{o}}$ and a step-like increase of the lattice constant $a_{2,\mathrm{o}}$ as depicted in figure 6.3(a). In the antiferromagnetic phase dysprosium shows a pronounced negative thermal expansion along the a_3-axis of the hexagonal unit cell, whereas the lattice constants within the basal plane $a_{1,\mathrm{hcp}}$ and $a_{2,\mathrm{hcp}}$ show an identical positive expansion. In contrast, dysprosium expands along all crystal directions in the paramagnetic phase. The negative thermal expansion along the a_3-axis indicates an anisotropic and contractive magnetic stress in the antiferromagnetic phase, which dominates over the tensile stress caused by phonons. The temperature-dependent lattice strain along the $a_{1,\mathrm{hcp}}$-axis and $a_{2,\mathrm{hcp}}$-axis exhibits a discontinuous slope at the Néel temperature, which is related to the changing sign of the Poisson stress arising from the changing thermal expansion along the a_3-axis.

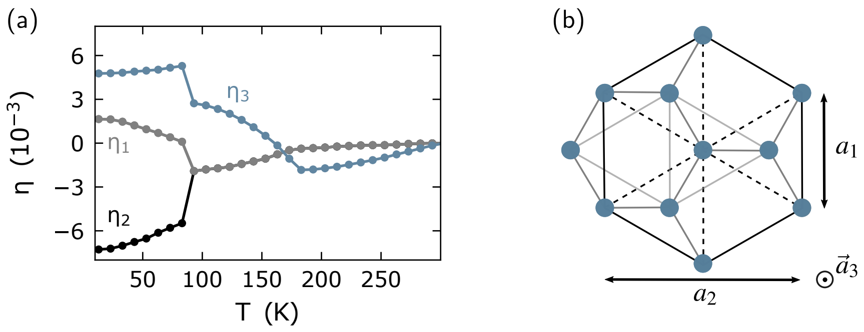

Figure 6.3: Temperature-dependent thermal expansion of bulk dysprosium. The temperature-dependent strain (a) displays a negative thermal expansion along the a_3-axis up to $T_\mathrm{N} = 180\,\mathrm{K}$. At the Curie temperature $T_\mathrm{C} = 90\,\mathrm{K}$ dysprosium undergoes a first order phase transition from a hexagonal ($a_{2,\mathrm{hcp}} = \sqrt{3}a_{1,\mathrm{hcp}}$) to an orthorhombic ($a_{2,\mathrm{o}} < \sqrt{3}a_{1,\mathrm{o}}$) unit cell (b). The structural phase transition corresponds to a step-like change of the lattice constants of the unit cell.

The dominant, contractive magnetic stress in dysprosium along the a_3-axis in the antiferromagnetic phase indicates a large magnetostriction and a strong interaction between lattice and magnetism. This giant magnetostriction is typical for the class of the heavy rare-earth metals from gadolinium to erbium as shown in figure 6.4. The temperature-dependent lattice strain of all materials exhibits a pronounced negative thermal expansion below the magnetic order temperature of the AFM (Dy, Ho, Er) and FM (Gd, Tb) phase [172, 181]. The spontaneous magnetostriction in the heavy rare-earth metals is described by *E. Callen* and *H. B. Callen* [21, 22]. Their formalism includes both spin-orbit interaction and exchange-striction as single-ion and two-ion interactions, respectively. The lattice deformation with changing magnetisation via spin-orbit interaction originates from the strongly anisotropic 4f orbitals in the crystal field [23, 182]. The demagnetisation with increasing temperature leads to a reorientation of the magnetic moments with diminishing magnetic order. In a simplified picture, the orientation of the magnetic moments determines the orientation of the 4f orbitals via spin-orbit interaction, which influences the lattice spacing via the overlap of the orbitals of neighbouring lattice sites.

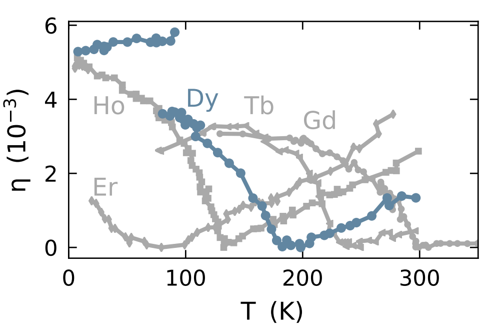

Figure 6.4: Comparison of the thermal expansion of the heavy rare-earth metals along the a_3-axis. Without exception all heavy rare-earth metals exhibit a negative thermal expansion below the magnetic order temperature of the AFM (Dy, Ho, Er) and FM (Gd, Tb) phase [172, 181]. This indicates a giant $(> 10^{-3})$ spontaneous magnetostriction in this class of materials.

In the case of gadolinium the half filled 4f shell causes a vanishing orbital momentum. The nonetheless occurring magnetostriction indicates the importance of the exchange-striction for the coupling of magnetism and lattice. The exchange-striction describes the dependence of the exchange parameter $J_{i,j}^{\mathrm{RKKY}}$ on the interatomic distance. In case of the indirect RKKY exchange interaction in the heavy rare-earth metals the exchange parameter even shows an oscillating dependence on the interatomic distance with changing sign [174, p. 207]. Therefore the exchange energy affects the equilibrium spacing of the magnetic ions by their alignment and leads to the giant magnetostriction in the heavy rare-earth metals in general and in particular in dysprosium.

6.1.2 Determination of Grüneisen constants

The negative thermal expansion of dysprosium relates to a contractive magnetic stress that arises from the excitation of the additional magnetic degrees of freedom and dominates over the tensile phonon stress. In the Grüneisen model (3.17) this stress relates linearly to an energy density stored in the magnetic system by a Grüneisen parameter Γ_{mag}. In this section I determine the out-of-plane Grüneisen constants of dysprosium as thin film. The Grüneisen constants of the phonons and the magnetic excitations in the thin film are used in the next section to analyse the spatio-temporal stress driving the picosecond strain response.

The determination of the Grüneisen constants of the phonons and the magnetic excitations in dysprosium require the separation of the temperature-dependent heat capacity to relate the temperature-dependent lattice stress to an energy density. The total heat capacity of bulk dysprosium [183] separated into the subsystem contributions is depicted in figure 6.5. The separation is adopted from the master thesis of my colleague *Alexander von Reppert* [133]. The electron contribution is approximated by the Sommerfeld model with the Sommerfeld constant of $\gamma_{\mathrm{S}} = 4.9\,\frac{\mathrm{mJ}}{\mathrm{mol\,K^2}}$ [184]. In the following determination of the Grüneisen constants I neglect the electron contribution due to the small fraction of energy density stored in the electrons in thermal equilibrium. The contribution of the phonons is determined by the heat capacity of the non-magnetic rare-earth Lutetium [185, 186], whose temperature dependence is scaled to match the Debye temperature $\Theta_\mathrm{D} = 183\,\mathrm{K}$ of dysprosium [187]. The difference to the total heat capacity determines the magnetic heat capacity that vanishes above the Néel temperature at which it exhibits a distinct peak. This separation routine of the total heat capacity assigns the latent heat of the structural first order phase transition at $90\,\mathrm{K}$ to the magnetic system as a simplification.

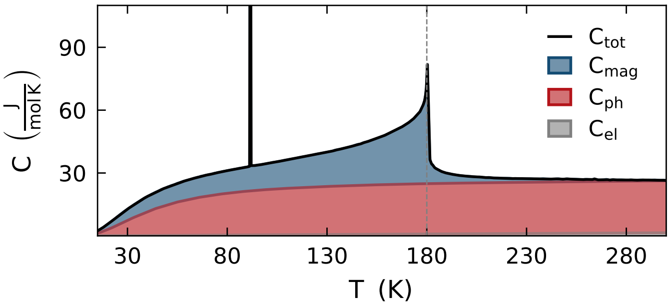

Figure 6.5: Temperature-dependent subsystem-separated heat capacity of bulk dysprosium. The contributions of the electrons and the phonons are determined by the Sommerfeld constant $\gamma_\mathrm{S} = 4.9\,\frac{\mathrm{mJ}}{\mathrm{mol\,K^2}}$ [184] and the heat capacity of the non-magnetic rare-earth Lutetium [185, 186] scaled by the Debye temperature $\Theta_\mathrm{D} = 183\,\mathrm{K}$ of dysprosium [187], respectively. The difference to the total heat capacity describes the magnetic heat capacity that vanishes above $T_\mathrm{N} = 180\,\mathrm{K}$.

In the next step I determine the temperature-dependent out-of-plane external stress σ_3^ext. In the Grüneisen model it relates to the temperature-dependent energy density stored in the subsystems given by the heat capacity contributions. In equilibrium the anisotropic thermal expansion η_λ is the elastic response to a total stress consisting of the uni-axial external stress $\sigma_\lambda^\mathrm{ext}$ and the additional Poisson stress $\sigma_\lambda^\mathrm{poi}$. In consideration of the general definition of thermal expansion (2.13), the elastic tensor of a hexagonal crystal (2.17) determines the out-of-plane Poisson stress to $\sigma_3^\mathrm{poi} = c_{13}\,(\eta_1 + \eta_2)$. The Poisson stress enables the determination of the external stress σ_3^ext using the equilibrium out-of-plane stress $\sigma_3 = c_{33}\eta_3$:

$$\sigma_3^\mathrm{ext} = c_{33}\eta_3 + \sigma_3^\mathrm{poi} \tag{6.1}$$

where η_3 denotes the strain in thermal equilibrium. Equation (6.1) determines the external stress along the a_3-axis of bulk dysprosium that denotes the out-of-plane direction of the thin film. To determine the Poisson stress in the thin film sample I assume the same external in-plane stress as the bulk material that I determine from the thermal expansion of bulk dysprosium shown in figure 6.3(a). Under this assumption, figure 6.6(a) displays the separation of the total equilibrium out-of-plane stress σ_3 into the Poisson stress σ_3^poi (gray dots) and the external stress σ_3^ext (black dots) using the elastic constants $c_{13} = 22.5\,\mathrm{GPa}$ and $c_{33} = 78.3\,\mathrm{GPa}$ [188].

Figure 6.6(b) shows the external stress as function of the temperature-dependent energy density stored in the phononic subsystem according to the respective heat capacity contribution in figure 6.5. The external stress exhibits a linear dependence on the energy density stored in the phonons well above the Néel temperature. The linear dependence determines the out-of-plane phononic Grüneisen constant along the a_3-axis of the hexagonal unit cell to $\Gamma_\mathrm{3,ph} = 1.1^\dagger$. The phononic Grüneisen constant determines the phononic stress contribution $\sigma_\mathrm{3,ph}^\mathrm{ext}$ over the full temperature range denoted by the red solid line in (a). The difference to the total out-of-plane stress defines the temperature-dependent magnetic stress contribution $\sigma_\mathrm{3,mag}^\mathrm{ext}$. Panel (c) depicts the magnetic stress mapped to the energy density stored in the magnetic subsystem by its heat capacity contribution.

[†] There are different measurements on the sample, which observe different expansion coefficients in the paramagnetic phase. Here, I choose the measurement used in the recent publication [29].

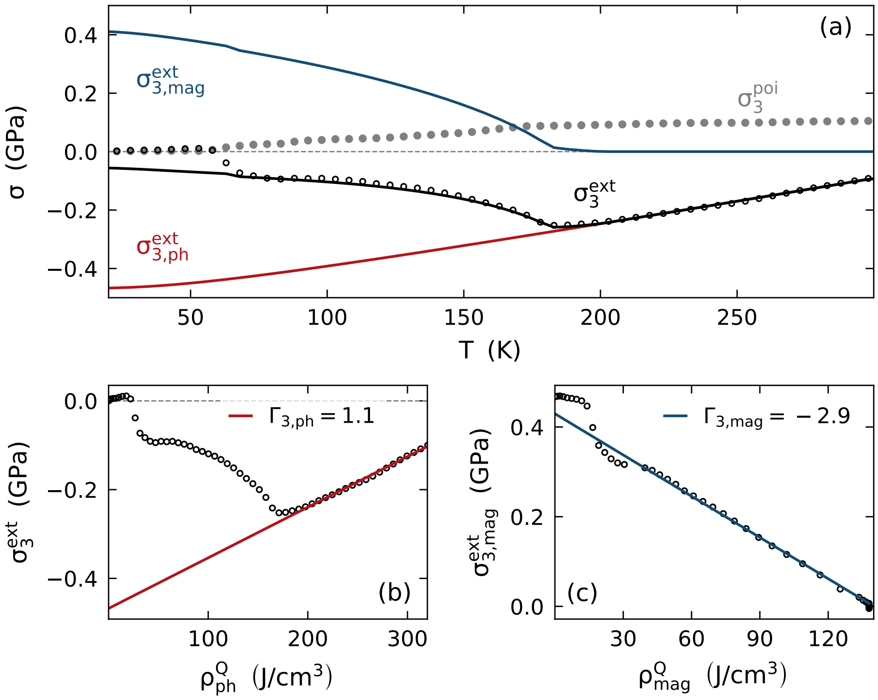

Figure 6.6: Determination of the phononic and magnetic Grüneisen constant of dysprosium. (a) The temperature-dependent external stress (black dots) results from the equilibrium expansion considering the additional Poisson stress (gray dots) according to equation (6.1). The phononic heat capacity contribution in figure 6.5 maps the stress to the energy density stored in the phonons ρ^{Q}_{ph} in (b). The linear dependence above T_{N} determines the phononic Grüneisen constant to $\Gamma_{3,\mathrm{ph}} = 1.1$, which defines the phononic stress contribution (red line). The difference to the total stress corresponds to the magnetic stress in (c). The linear dependence on the energy density stored in the subsystem ρ^{Q}_{mag} in the AFM phase determines the magnetic Grüneisen constant to $\Gamma_{3,\mathrm{mag}} = -2.9$. The Grüneisen model of the external stress as superposition of the subsystem contributions is denoted by the black line in (a).

Well above the first order phase transition the magnetic stress contribution depends linearly on the deposited energy density and determines the magnetic Grüneisen constants to $\Gamma_{3,\mathrm{mag}} = -2.9$. However, the Grüneisen model does not capture the step-like stress contribution arising from the first order phase transition, which indicates the limitations of the usage of a single temperature-independent Grüneisen constant for each sub-system. The phononic and magnetic Grüneisen constants determine the respective temperature-dependent stress contribution. Its superposition corresponds to the total out-of-plane external stress (black solid line), which describes well the stress calculated from the equilibrium expansion (black dots) in figure 6.6(a).

6.2 The Grüneisen model of the spatio-temporal stress

In this section I describe the application of the Grüneisen approach to determine the spatio-temporal stress of electrons, phonons and magnetic excitations in the inhomogeneously excited dysprosium transducer. The model captures the electron-phonon coupling as well as the excitation of the magnetic subsystem on two timescales via coupling to the electrons and the phonons. The transferred energy density translates via the subsystem-specific Grüneisen constants to stress contributions that drive the strain response. In addition to the finite subsystem coupling timescales, the spatial redistribution of energy by heat diffusion on a timescale of hundreds of picoseconds results in a time-dependent total stress in the different layers of the heterostructure.

In the first part of the section I present the modelling of the strain response in the dysprosium transducer and the niobium detection layer in the absence of a magnetic stress contribution at 250 K in the paramagnetic phase. The modelling of the strain wave and the transient thermal expansion governed by the heat diffusion determine a spatio-temporal electron-phonon stress. The calibration of the non-magnetic properties of the heterostructure prepares the implementation of the magnetic subsystem at initial sample temperatures below T_N. The second part provides the transient strain of the dysprosium transducer and the niobium detection layer, which provides first insights into the temperature- and fluence-dependent magnetic stress. In the last section I describe the implementation of the magnetic stress into the model by transferring locally energy density from the electron-phonon system to the saturable magnetic subsystem under energy conservation.

6.2.1 The spatio-temporal electron-phonon stress

In this section I model the spatio-temporal stress of the electrons and the phonons in the paramagnetic phase, which drives the strain response of the dysprosium transducer and the niobium detection layer. The strain response consists of propagating picosecond strain pulses and the quasi-static expansion as elastic response to the out-of-plane stress. The different propagation times of sound and heat result in the separation of these two contributions in time when detected in the buried detection layer. The optical penetration depth and the electron-phonon coupling determine the temporal shape of the strain wave. Its propagation through the heterostructure is determined by the layer thickness. In contrast, the temporal shape of the delayed expansion of the niobium layer depends on the heat conductivities of the materials. In total the modelling provides the spatio-temporal electron-phonon stress using Fourier's heat law.

In figures 6.7(a) and (b) the open symbols denote the time-resolved mean strain of dysprosium and niobium measured by ultrafast X-ray diffraction using reciprocal space slicing with an area detector (see chapter 4). The dysprosium transducer rapidly expands within the first picoseconds after the laser excitation and recovers to the initial mean lattice constant on nanosecond timescale via heat diffusion. The rapid expansion originates from an expansive stress in dysprosium, which exceeds the expansive stress in the yttrium capping layer and drives a bipolar strain wave at the interface. The maximum expansion of dysprosium at 29 ps corresponds to the propagation of the expansive part of the bipolar strain wave through the layer to the dysprosium-yttrium interface. Subsequently, the expansive part propagates into the niobium layer and leads to a maximum expansion at 52 ps. This expansion of niobium is preceded by a compression indicating the bipolar shape of the driven strain wave. The absence of a strain response of niobium for the first 15 ps indicates the negligible optical excitation of the buried detection layer. The partial reflection of the driven strain pulses at the interfaces with non-perfect impedance match leads to a damped oscillation of the strain of dysprosium and a second bipolar feature in the niobium layer between 80 and 125 ps. In addition to these signatures of the strain waves, the average strain of the niobium layer slowly increases due to the deposition of energy via heat diffusion on the nanosecond timescale. The strain response of niobium demonstrates the separation of the picosecond strain pulses and the thermal expansion in the time domain due to the different propagation velocities of sound and heat. This enables the background-free detection of the driven strain wave in the niobium layer that facilitates the modelling and interpretation of the results.

In the following paragraphs I describe the modelling of the strain dynamics of dysprosium and niobium using the modular MATLAB library UDKM1DSIM [124]. The homogeneous lateral excitation of the probed volume in the thin film geometry limits the strain response to the out-of-plane direction (see section 2.2.2). The one-dimensional linear-chain model of masses and springs of UDKM1DSIM simulates the strain response of the heterostructure on the basis of a spatio-temporal stress. The spatial dependence of the stress originates from the inhomogeneous excitation of the hundreds of nanometres thick heterostructure. The subsequent heat diffusion and the electron-phonon coupling add a temporal dependence to the stress. Table 6.1 summarises the static

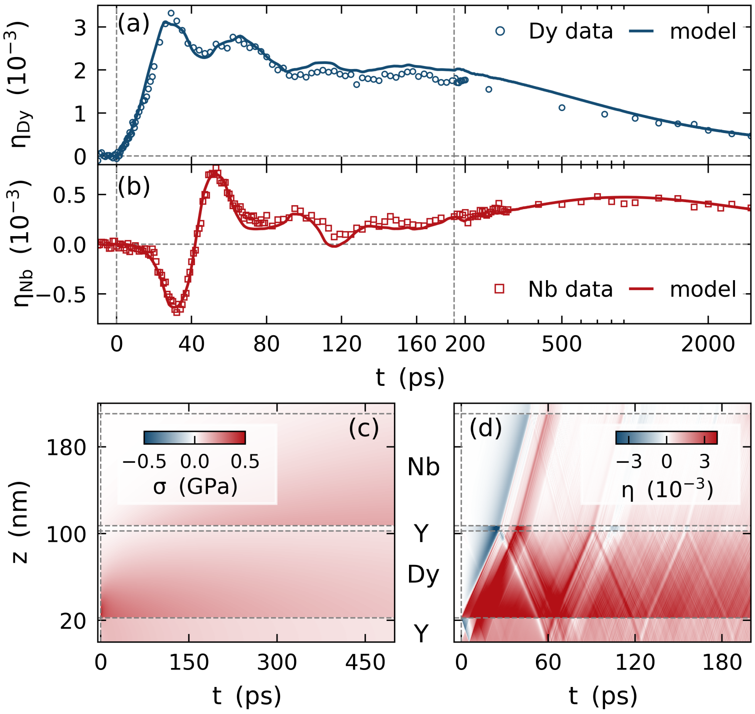

Figure 6.7: Modelled strain response to a spatio-temporal laser-induced stress in the paramagnetic phase. The strain response of the laser-excited dysprosium transducer (a) and the niobium detection layer (b) at $250\,\mathrm{K}$ and $7.2\,\frac{\mathrm{mJ}}{\mathrm{cm}^2}$ (open symbols) are modelled using the Matlab library udkm1Dsim [124] (solid lines). The modelling provides the spatio-temporal electron-phonon stress in the absence of magnetic excitations (c). A linear-chain model of masses and springs calculates the corresponding spatio-temporal strain (d) including strain waves. The modelling calibrates the layer thickness, the optical penetration depth, the electron-phonon coupling time and the heat transport, which are fixed in the further modelling including magnetic stress.

properties of the different layers and materials. To match the measured strain response I need to adjust certain parameters with respect to the literature values[‡]. In the table these adjustments are marked by stars and the corresponding literature values are given additionally in brackets. The parameters which are changed in respect to our recent publication [29] are underlined and are limited to the heat conductivities. To account for the dimensionality of the dynamics I use the thermal expansion coefficients $\alpha_{\perp}^{\mathrm{c}}$ under clamped in-plane lattice dimensions. These expansion coefficients depend linearly to the phononic out-of-plane Grüneisen constant $\Gamma_{3,\mathrm{ph}}$. I determine the phononic Grüneisen constants of yttrium, niobium and sapphire in consideration of equation (3.15) using the bulk equilibrium thermal expansion.

The following paragraphs describe the influence of various parameters on the strain response of dysprosium and niobium. In the first step I model the temporal shape of the driven strain wave depending on the electron-phonon coupling, the phononic Grüneisen constant and the optical penetration depth. The strain wave and therefore these parameters determine the temporal shape of the rapid expansion of dysprosium and the compression of niobium. First, I increase the optical penetration depth of the yttrium capping layer to $\lambda_{\mathrm{Y}}^{\mathrm{film}} = 72\,\mathrm{nm}$ and reduce the phononic Grüneisen constant by $65\,\%$ to $\Gamma_{3,\mathrm{ph}}^{\mathrm{Y}} = 0.45$. As already mentioned, the immediate expansion of dysprosium within the first picoseconds requires a larger tensile stress in dysprosium than in the yttrium capping layer at the yttrium-dysprosium interface. The adjustments reduce the expansive stress in yttrium by reducing both the deposited energy density and the stress generation efficiency. These

---

[‡] For example, the adjusted out-of-plane lattice constant of yttrium accounts for the separation of the Bragg peaks of Y and Dy in the RSM in figure 6.2, which may be due to a growth induced epitaxial strain.

assumptions may be rationalised by an oxidation of the capping layer that leads to a partially transparent layer that reduces the laser-induced tensile stress[§]. The dominating tensile stress in dysprosium at the yttrium-dysprosium interface drives a bipolar strain wave. I use the expansion of dysprosium within the first picoseconds to determine the stress rise time. The compression of the niobium detection layer determines the spatial shape of the strain wave that translates by the sound velocity to a temporal shape. Assuming a finite electron-phonon coupling and an electronic Grüneisen constant smaller than the phononic one provide an effective stress rise time that delays the expansion of the dysprosium transducer. To match the measurements I choose an electron-phonon coupling time constant of $\tau_{\text{el-ph}} = 2\,\text{ps}$ and an electronic Grüneisen constant of $\Gamma_{3,\text{el}} = 0.5 \cdot \Gamma_{3,\text{ph}}$ for both yttrium and dysprosium. Under the condition of the transducer thickness exceeding the optical penetration depth, the spatial shape of the strain wave depends on both the the optical penetration depth of dysprosium and the modelled electron-phonon coupling (see section 2.2.2). I adjust the optical penetration depth of dysprosium to $\lambda_{\text{Dy}}^{\text{film}} = 22\,\text{nm}$.

In the second step I model the propagation of the strain wave whose partial reflection at interfaces with non-perfect impedance match results in the oscillatoric behaviour of the mean strain of dysprosium. The propagating strain wave influences the mean strain of a layer by the propagation into and out of the layer. The propagation of the expansive or the compressive part of the bipolar strain wave into a layer increases or decreases the mean strain of the layer, respectively. The propagation of the bipolar strain pulse out of the probed layer then has the inverse effect. Thus the local maxima and minima in the mean strain denote the propagating strain waves and their pump-probe delay determines the layer thickness. In analogy to the simple film-substrate system in figure 2.3, the maximum expansion of dysprosium corresponds to the left compressive part of the bipolar strain wave and thus to the thickness of the dysprosium layer with respect to its sound velocity. The maximum compression of niobium relates to the entering of the expansive part of the strain wave. Therefore, the delay to the maximum expansion of dysprosium determines the thickness of the bottom yttrium layer. The subsequent propagation of the compressive part of the bipolar strain wave into the substrate causes the maximum expansion of niobium and the delay with respect to the maximum compression defines the thickness of the niobium layer. The thickness of the capping yttrium layer is determined by the temporal delay of the strain wave echo at $90\,\text{ps}$. This bipolar feature relates to the bipolar strain wave reflected at the non-perfect impedance matched yttrium-niobium interface and the surface. The inverted sign in the mean strain of niobium indicates the phase jump during the reflection of the strain wave at the surface. This analysis is summarised by the strain map in figure 6.7(d) provided by the modelling.

In the last step the quasi-static expansion of the niobium detection layer in the absence of coherently excited strain pulses is modelled. The quasi-static expansion as elastic response to the laser-induced stress is given by the time-dependent energy density in the layers, which depends on the heat diffusion. To match the energy transport from dysprosium to the substrate that transiently deposits energy to the intermediate niobium layer, I adjust the thermal conductivity of the layers except dysprosium. The reduced thermal conductivity in yttrium, niobium and sapphire slows down the heat transport and mimics interface resistances in the real sample. The reduced thermal conductivities are summarised in table 6.1 and to some extend deviate from the values given in our recent publication [29]. The corrections become necessary to correct an error in the modelling of the time-dependent heat transport that mainly affects the modelled strain at times larger than $200\,\text{ps}$. This timescale is not relevant for the picosecond strain pulses but for the remagnetisation process that is discussed in the remainder of this thesis. The modelling of the strain response up to $3\,\text{ns}$ provides the spatio-temporal electron-phonon stress in the absence of a magnetic order depicted in figure 6.7(c).

[§] Note, the shape of the expansion of dysprosium within the first picoseconds indicates a bipolar strain pulse propagating from yttrium into the dysprosium layer. Thus the assumption of a complete oxidation contradicts the diffraction data.

Property	**Y**	**Dy**	**Nb**	**Al_2O_3**
layer thickness (nm)	22 (37) 5 (8)	80 (142)	103 (220)	900 (1890)
lattice constant (Å)				
a_3-axis out-of-plane	$6.03^\star$ (5.73)	5.65	4.67	4.76
a_1-axis in-plane	3.65	3.59	4.67	12.80
a_2-axis in-plane	3.65	3.59	3.30	8.24
elastic constants (GPa)	from [189]	from [188]	from [190]	from [191]
c_{33}	77.8	78.3	246.7	498.1
c_{13}	20.0	22.5	133.7	110.9
c_{11}	79.0	74.2	246.7	496.8
c_{12}	28.7	25.5	133.7	163.6
density ρ ($\mathrm{g\,cm^{-3}}$)	4.47	8.6	8.57	4.05
sound velocity v_s (nm/ps)	4.15	3.10	5.08	11.14
lin. therm. expansion ($10^{-6}\,\mathrm{K^{-1}}$)	from [180]	from [180]	from [192]	from [193]
clamped: out-of-plane $\alpha_\perp^\mathrm{c}$	$8.1^\star$ (22.9)	20.7	18.2	9.1
bulk: out-of-plane $\alpha_\perp$	19.7	20.3	7.6	6.2
bulk: in-plane $\alpha_\parallel$	6.2	4.7	7.6	6.2 / 7.1
specific heat C_V ($\mathrm{J\,kg^{-1}K^{-1}}$)	291.49 [186]	167.3 [183]	270.88 [184]	657.22 [194]
Grüneisen constant $\Gamma_{3,\mathrm{ph}}$	$0.45^\star$ (1.3)	1.1	1.5	1.7
thermal conductivity κ ($\mathrm{W\,m^{-1}K^{-1}}$)	$17.4^\star$ 24.8 [195]	11.1 [195]	$26.5^\star$ 53.0 [195]	$23.3^\star$ 58.3 [196]
optical penetration depth (nm)	$72^\star$ (24)	$22^\star$ (24)	25	∞

Table 6.1: Thermo-elastic properties of the materials in the heterostructure determined by the modelling of the transient strain by the MATLAB library UDKM1DSIM [124]. The thickness of the different layers is determined by the modelling of the strain response and corresponds to a number of unit cells in the simulation given in the brackets. The quantities marked by a star are adjusted in the model and deviate from the literature value given in the brackets. The underlined values of the heat conductivity differ from our recent publication [29].

6.2.2 Temperature- and fluence-dependent strain pulses

The excitation of the magnetic subsystem below the Néel temperature results in a temperature-dependent contractive magnetic stress, which reduces the total laser-induced stress. This section summarises the temperature and fluence dependence of the strain response of the dysprosium transducer and the niobium detection layer to investigate the spatio-temporal magnetic stress. The strain response of dysprosium encodes the excitation timescale of the magnetic subsystem. In contrast, the strain response of niobium encodes the spatial profile of the magnetic stress by the detected strain pulses. Figures 6.8(a) and (b) display the time-resolved strain at different initial sample temperatures with a constant excitation fluence of $7.2\,\frac{\mathrm{mJ}}{\mathrm{cm^2}}$. Panels (c) and (d) display the strain response to different excitation fluences at an initial sample temperature of 130 K. In the previous chapter I already demonstrated that both the initial sample temperature and the excitation fluence determine the saturation of the magnetic stress due to the finite integral of the magnetic heat capacity. While the initial sample temperature determines the maximum amount of energy storable in the magnetic system, the excitation fluence determines the energy that is potentially transferable to the magnetic system. The saturation of the magnetic stress enhances the fraction of energy density stored in the phonons and thus the total stress driving the strain response. In the following paragraphs I describe the analysis of the strain response that indicates the role of the saturation of the magnetic stress.

In the first step I analyse the strain response of dysprosium and niobium as function of the initial sample temperature. Cooling the sample below the magnetic order temperature $T_N = 180\,\mathrm{K}$ leads to a reduced expansion of dysprosium that indicates the additional contractive stress arising from the magnetic excitations. Below $100\,\mathrm{K}$, the rapid expansion of dysprosium that is observed in the paramagnetic phase changes to a slow contraction. In the intermediate temperature range dysprosium expands within the first picoseconds and contracts subsequently. Since the zero-strain crossing at $35\,\mathrm{ps}$ for $130\,\mathrm{K}$ exceeds the strain propagation time through the dysprosium layer, the changing sign of the average strain must relate to a changing sign of the mean total stress and is not fully explained by propagating strain pulses. In consideration of the slow contraction at $31\,\mathrm{K}$ this indicates an excitation of the magnetic system on a timescale that exceeds the electron-phonon coupling time and delays the rise of the contractive stress. However, the vanishing expansion of dysprosium within the first picoseconds indicates a compensation of the rapidly rising tensile electron-phonon stress by a quasi-instantaneous magnetic stress contribution. This observation is rationalised by an excitation of the magnetic subsystem on two timescales. In conclusion, the transient mean strain of dysprosium indicates a mean total stress in the layer that changes its sign at intermediate temperatures. This occurs because the magnetic subsystem is excited on both a quasi-instantaneous and a timescale exceeding the rise of the tensile phonon stress.

The strain pulses driven by the total stress in dysprosium are detected as an average strain of the buried niobium layer. The strain pulses extend the analysis by an insight into the spatial dependence of the total stress. The signature of the driven strain pulses changes from a bipolar shape to a uni-polar shape at low temperatures. At intermediate initial sample temperatures,

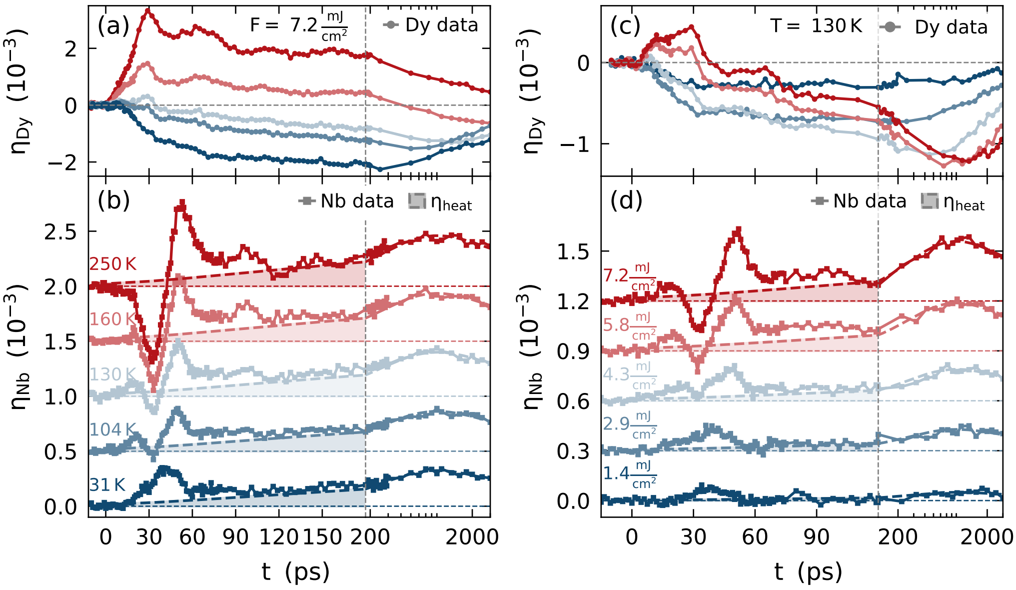

Figure 6.8: Strain response of the dysprosium transducer and the niobium detection layer at different initial sample temperatures (a,b) and for different excitation fluences (c,d). The rapid expansion of dysprosium in the paramagnetic phase changes to a slow contraction at low temperatures. The changing response of dysprosium is accompanied with a change of the driven strain pulse from bipolar to uni-polar. In the intermediate temperature range, dysprosium expands within the first picoseconds but contracts afterwards. This changes the strain pulses detected in niobium to an asymmetric bipolar strain wave preceded by a fast expansion. The decrease of the excitation fluence changes the response to a pure contraction of dysprosium and a uni-polar expansion of niobium. The shaded areas approximate the thermal expansion of niobium due to heat transport. It decreases with the excitation of the magnetic system in dysprosium while the temporal shape stays temperature- and fluence-independent.

niobium shows an expansion within the first picoseconds followed by a bipolar strain pulse that becomes asymmetric with decreasing temperature. The expansion within the first picoseconds is related to a contractive total stress at the bottom of the dysprosium layer driving an expansion, which propagates into the adjacent niobium layer. In contrast, the following bipolar strain pulse with identical timing as in the paramagnetic phase indicates an expansive total stress at the front side of the dysprosium layer. Thus the strain response of niobium hints at a total stress that changes its sign within the dysprosium layer at intermediate temperatures. In consideration of the inhomogeneous excitation of the dysprosium layer which is thicker than the optical penetration depth, this conclusion is rationalised by a spatially-dependent saturation of the magnetic stress. The associated maximum contractive stress leads to a to a dominating electron-phonon stress in the front part of the layer. At the backside of the dysprosium layer the unsaturated magnetic stress dominates and induces an contraction. With increasing temperature the part where the electron-phonon stress dominates extends further into the layer and the bipolar feature of the strain wave becomes dominant in the strain response of the niobium layer.

In addition to the initial sample temperature, the excitation fluence determines the saturation of the magnetic stress. The strain response to different excitation fluences at $130\,\mathrm{K}$ is depicted in figures 6.11(c) and (d). With decreasing fluence, the response of dysprosium changes from expansive within the first tens of picoseconds to purely contractive and the expansion of niobium changes to uni-polar. This fluence dependence is similar to the temperature dependence because both originate from the saturation of the magnetic stress. For fluences above $2.9\,\frac{\mathrm{mJ}}{\mathrm{cm}^2}$ the mean strain of niobium exhibits a bipolar shape indicating the saturation of the magnetic stress and the domination of the electron-phonon stress at the front side of the layer. This also increases the total average stress in the dysprosium layer, which reduces the contraction at $60\,\mathrm{ps}$ with increasing fluence. Furthermore, the time dependence of the mean strain of dysprosium between 30 and $120\,\mathrm{ps}$ changes. At low fluences the mean strain stays rather constant, while for higher fluences the contraction of dysprosium increases with time. This indicates a delayed cooling of the spins with respect to the phonons by heat diffusion under the condition of a saturated magnetic stress. The long-lasting excitation of the magnetic subsystem provides a remaining contractive stress. The remaining contractive stress results in an increasing contraction of dysprosium and a delayed maximum contraction after about $500\,\mathrm{ps}$. Under the condition of temperatures near the Néel temperature and high fluences, the fraction of the fully demagnetised layer increases and shifts the delayed maximum contraction to larger delays. In general, the temperature- and fluence-independent shape of the thermal expansion of niobium depicted by the shaded areas corresponds to a similar heat diffusion in the presence of an excitable magnetic subsystem. However, the amplitude of the thermal expansion is temperature-dependent and decreases with decreasing temperature. Since the decreasing initial sample temperature corresponds to an increasing maximum amount of energy storable in the magnetic subsystem of dysprosium, the reduced thermal expansion of niobium indicates the magnetic system to act as a saturable heat sink.

6.2.3 The spatio-temporal excitation of the magnetic system

This section presents the implementation of the magnetic subsystem to the total laser-induced stress in dysprosium using the Grüneisen approach. The presented model results in a spatio-temporal subsystem-specific stress that extends the discussion of the simple case of homogeneous excitation and ultrafast subsystem equilibration for SRO in the previous chapter. The laser-induced non-equilibrium between the electrons, phonons and spins requires the explicit modelling of the energy transfer between the subsystems under the constraint of energy conservation. I model the excitation of the spins on a quasi-instantaneous ($< 1\,\mathrm{ps}$) and a $15\,\mathrm{ps}$ timescale. In addition, the inhomogeneous excitation and the subsequent heat transport provide a time-dependent spatial distribution of the energy, which I assume to be identical for phonons and magnetic excitations.

Under the assumption of temperature-independent Grüneisen constants, the excitation of the magnetic order below the Néel temperature $T_\mathrm{N} = 180\,\mathrm{K}$ extends the electron-phonon stress in the paramagnetic phase by an additional stress contribution. Therefore the total stress is given by the superposition of the electron-phonon stress and the spatio-temporal magnetic stress that depends on the time-dependent energy density stored in the magnetic system and its time-dependent spatial distribution. The conceptual steps of the modelling routine are summarised in figure 6.10 at $104\,\mathrm{K}$. The figure provides an overview about the time-dependent energy density stored in each layer (a-d), the time-dependent energy distribution between the phonons and the magnetic subsystem in dysprosium (e-h) and the subsystem separated spatial stress profile that illustrates the spatial distribution of the energy density (i-l).

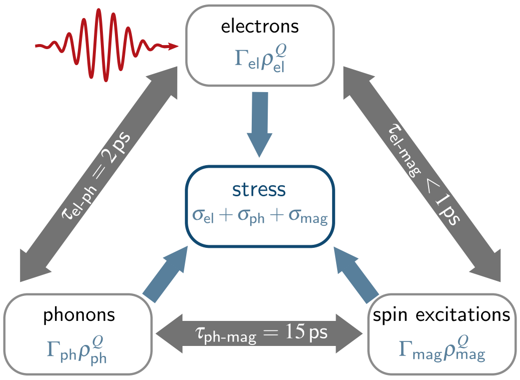

Figure 6.9: Schematic sketch of the subsystem coupling in dysprosium. The laser-excited electrons distribute the deposited energy to the phonons $\tau_\text{el-ph} = 2\,\mathrm{ps}$ and the magnetic excitations $\tau_\text{el-mag} < 1\,\mathrm{ps}$. Additionally, the spins are excited by phonon-spin coupling with $\tau_\text{ph-mag} = 15\,\mathrm{ps}$. The energy density stored in each subsystem relates finally to a stress contribution by the subsystem-specific Grüneisen constant Γ_r.

The basis of the model is the spatio-temporal energy distribution in the paramagnetic phase in the absence of a magnetic order determined in section 6.2.1. In the first step a fraction of the energy density stored in the electron-phonon subsystem (e) is transferred to the magnetic subsystem under energy conservation (f). The underlying coupling of the subsystems is sketched in figure 6.9 and displays the excitation of the spins by electron-spin and phonon-spin coupling. Thus, the excitation of the magnetic system is described by four parameters: the two timescales and the transferred amount of energy density. In agreement with the recent investigation of the demagnetisation of dysprosium by *Thielemann-Kühn and co-workers* [197] I choose an instantaneous electron-spin energy transfer time $\tau_\text{el-mag} < 1\,\mathrm{ps}$ that captures the sub-picosecond demagnetisation and a phonon-spin energy transfer time of $\tau_\text{ph-mag} = 15\,\mathrm{ps}$ that captures the delayed demagnetisation. The excitation on two timescales accounts for the vanishing strain in the first picoseconds and the subsequent slow contraction of dysprosium at $31\,\mathrm{K}$ in figure 6.8(a). Although the demagnetisation of the rare-earth metals has been shown in multiple experiments [197–201], the microscopic interpretation is still under debate[¶]. In my model I transfer on each of these two timescales 24% of the energy density stored in dysprosium to the spins. The two excitation timescales in combination with the transferred amount of energy density determine the time-dependent energy density in the magnetic subsystem (f). I assume the spatial distribution of the magnetic energy density to follow the phonon energy distribution determined in the paramagnetic phase as depicted in (j). This assumption is supported by the observation of a temperature-independent heat diffusion in a comparable heterostructure of dysprosium [35]. The energy transfer to the magnetic system reduces the energy density stored in the phonons and thus also the expansive phonon stress contribution (j). However, the layer-specific energy density is up to here not affected by the excitation of the magnetic order in dysprosium (comparison of (a) and (b)).

[¶] *Thielemann-Kühn and co-workers* attribute the quasi-instantaneous demagnetisation to the optical excitation of the itinerant 5d6s electrons and the second timescale to the demagnetisation of the 4f magnetic moments by the coupling to the phonons. This is supported by the observed different demagnetisation behaviour of the itinerant conduction band electrons and the 4f electrons reported by *Frietsch and co-workers* [198]. However, *Rettig and co-workers* [199] observe a simultaneous demagnetisation of the 5d6s and 4f electrons by resonant X-ray diffraction in holmium.

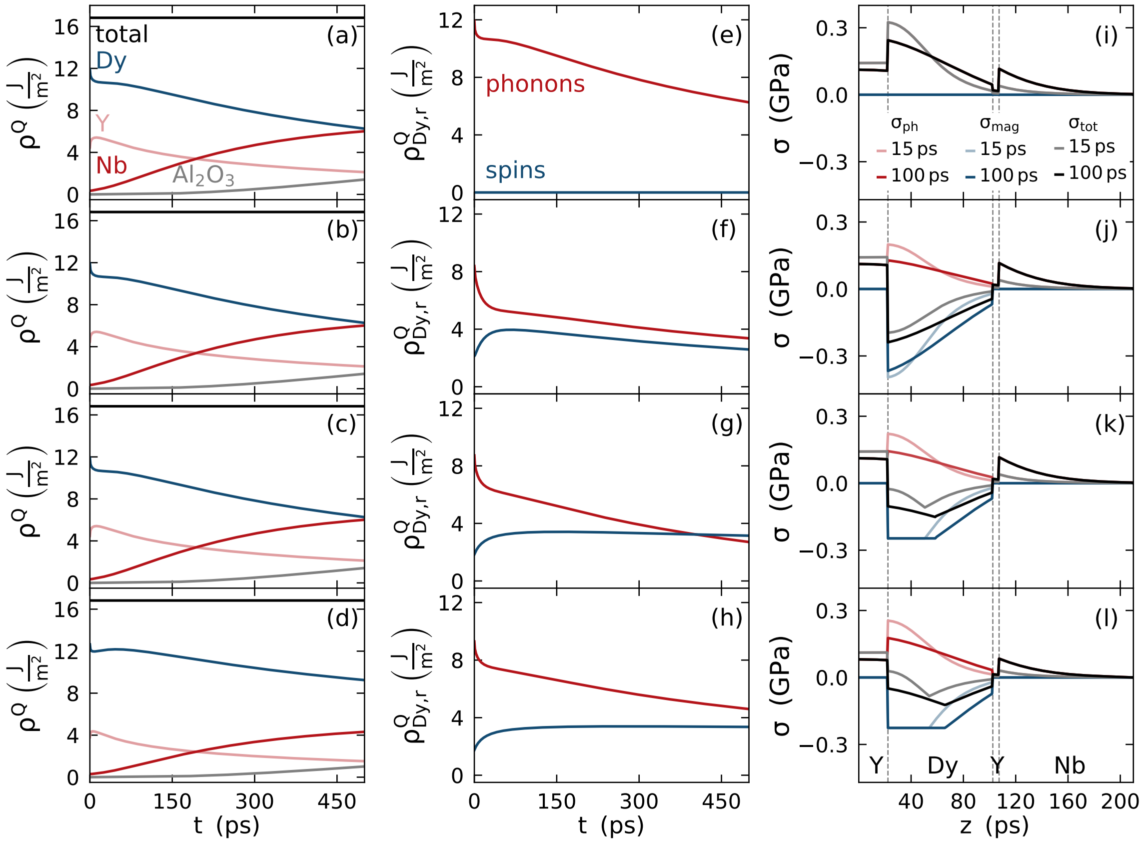

Figure 6.10: Modelling of the spatio-temporal magnetic stress at 104 K and $7.2\,\frac{mJ}{cm^2}$ separated into the four conceptual steps. The figures (a-d) display the time-dependent energy density stored in the layers of the heterostructure. The energy density in dysprosium is divided between the phonons and the magnetic system (e-h), which results in a total lattice stress as superposition of the subsystem contributions (i-l). The starting point of the routine is the spatio-temporal energy density distribution in the heterostructure at 250 K (a) in the absence of a magnetic excitation (e). In the first step energy is transferred from the electron-phonon system to the magnetic subsystem (f) under energy conservation (b). Subsequently I introduce the saturation of the magnetic stress according to the start temperature (k) and assume no recovery of the saturated unit cells. In the last step I reconstruct the phonon diffusion in the heterostructure by transfer energy from the adjacent layers to the phonons in dysprosium, which reduces the energy density stored in these layers (d).

In the next step I include the saturation of the magnetic stress by a maximum amount of energy storable to the magnetic system. The storable energy density is defined by the magnetic heat capacity. Since this maximum amount depends on the initial sample temperature, the saturation of the magnetic stress provides the temperature dependence of the magnetic and total lattice stress. The modelling of the temperature-dependent strain response determines the maximum amount of energy density storable in the magnetic system in dysprosium to $\rho^{sat}_{mag}(T) = 0.72\int_T^{\infty} C_{mag}(T')\,dT'$[‖], which is reduced with respect to the equilibrium bulk heat capacity in figure 6.5. The inhomogeneous excitation of the dysprosium layer results in an inhomogeneous saturation of the magnetic stress as depicted in (k). I assume the saturated unit cells of dysprosium to stay fully demagnetised. This accounts for the delayed cooling of the magnetic subsystem in comparison to the phonons under the condition of a saturated magnetic stress as observed in figure 6.8.

[‖] Note, this saturation level is slightly lower than in our recent publication [29] due to the changed ratio of the phononic and magnetic Grüneisen constant by including the Poisson stress correctly.

The underlying assumption of a long lasting non-equilibrium is in agreement with the previous investigation by my colleague *Alexander von Reppert* [27], which observed a non-equilibrium between the phonons and the magnetic system even on the nanosecond timescale. The saturation of the magnetic stress reduces the energy density stored in the magnetic system (g). The maximum in the contractive stress changes the total stress (k). At the same time, the neglected remagnetisation of the fully demagnetised unit cells suppresses the cooling of the magnetic system on the nanosecond timescale. The additionally required energy density is taken from the phonons to fulfil energy conservation (c) and reduces the phononic energy density as depicted in (g).

In general, the excitation of the magnetic system reduces the energy density stored in the phonons and thus leads to discontinuities in the phonon temperature profile resulting from heat diffusion. In the last step I reconstruct the phonon temperature profile. Therefore, I transfer time-dependent energy from the adjacent layers to the phonons in dysprosium to compensate the energy density transferred to the spins. Since this procedure increases the total energy density stored in the dysprosium layer it also affects the excitation of the magnetic system. Repetition of the three last steps of the routine leads to a continuous phonon temperature profile in the heterostructure reduced by the energy density stored in the magnetic subsystem of dysprosium. This reduces the energy density stored in the adjacent layers of the heterostructure and the lattice stress as depicted in (d) and (l). At the same time the energy density in the phonons and the magnetic excitations in dysprosium increase (h), which leads to an additional, expansive stress in the dysprosium layer.

6.3 Saturated magnetic stress causes unconventional strain waves

This section analyses the transient strain in a linear-chain model that results from the Grüneisen model of the ultrafast stress presented in the previous section. The agreement of the modelled strain with the temperature- and fluence-dependent strain using a single set of parameters quantitatively verifies the model of the spatio-temporal magnetic excitations. Furthermore, it reveals the role of the space- and time-dependent saturation of the magnetic stress for both the delayed contraction of dysprosium and the unconventional strain pulses detected in niobium. The saturation of the magnetic stress in the front part of the layer leads to a dominant tensile electron-phonon stress driving a bipolar strain wave. The bipolar strain wave superimposes with the expansive strain pulse driven at the bottom dysprosium-yttrium interface by the dominating contractive magnetic stress. The presented results extend our recent publication [29] by the calculation of the heat diffusion. The model predicts the thermal expansion due to heat diffusion in dysprosium and niobium for non-saturated magnetic stress at low fluences. The reduced thermal expansion of niobium at temperatures below the magnetic order temperature directly relates to the energy density stored in the magnetic subsystem, which acts as a saturable heat sink. However, the deviation on the nanosecond timescale for high fluences indicates that the remagnetisation of the fully demagnetised unit cells in dysprosium is not captured by the model.

Figure 6.11 depicts the strain response to the modelled stress by the Grüneisen approach (solid lines) in comparison to the measured strain by ultrafast X-ray diffraction (open symbols) at different initial sample temperatures (a,b) and for different excitation fluences (c,d). The Grüneisen model captures the temperature- and fluence-dependent strain response of dysprosium and niobium. The model contains only five parameters that describe the excitation of the magnetic subsystem and the assumption of a shared spatial distribution of the energy density for phonons and magnetic excitations. The agreement with both the time-dependent expansion of dysprosium and the driven strain pulses detected in niobium indicates a well modelled spatio-temporal magnetic stress. Here, the expansion of dysprosium depends on the average total stress and its spatial profile determines the driven strain pulses. In this thesis I extend our previous publication [29] by the calculation of the thermal expansion of niobium up to 3 ns. The model captures the temperature-dependent amplitude of the thermal expansion of niobium that decreases below the magnetic order temperature. However, the model underestimates the expansion of niobium at initial sample

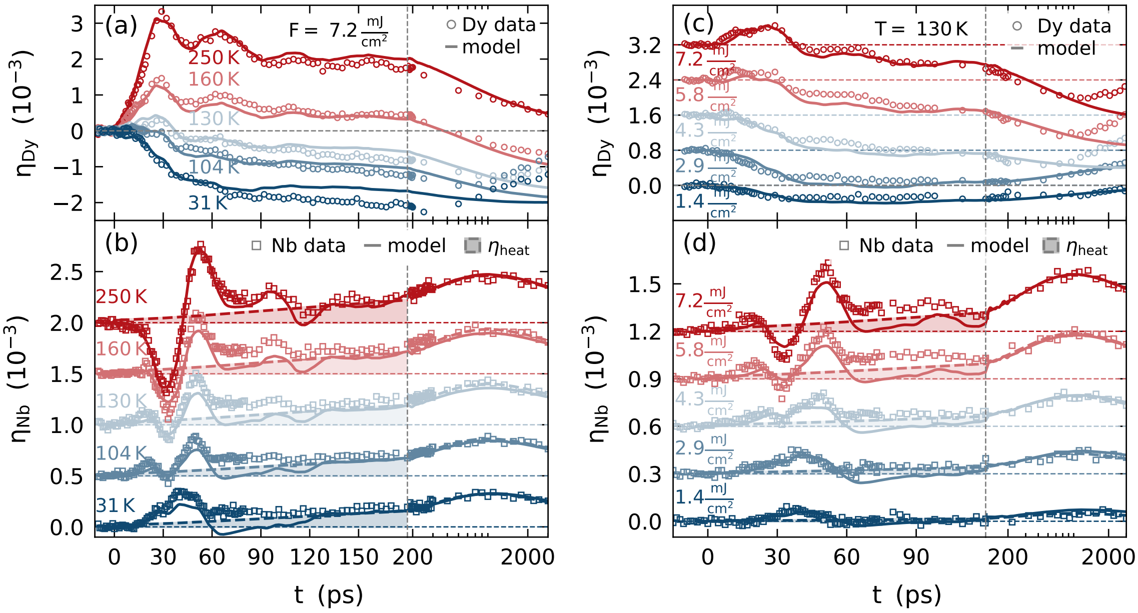

Figure 6.11: Modelled strain response of dysprosium (a,c) and niobium (b,d) at different initial sample temperatures (a,b) and to different excitation fluences (c,d). The modelling now extends up to 3 ns, which goes beyond the simulation that is presented in our recent publication [29]. The transient strain response predicted by the model (solid lines) captures the systematic variation of the measured results (open symbols) using a single set of parameters. The reduced phonon heat transport into niobium due to the excitation of the magnetic system matches the observed reduced thermal expansion of niobium. (Adopted from [29])

temperatures slightly below the Néel temperature and for high fluences. The underestimation of the expansion originates from on overestimation of the energy stored in the magnetic subsystem due to the neglected remagnetisation of the fully demagnetised unit cells. The resulting overestimation of the contraction of dysprosium on nanosecond timescale demonstrates that it is necessary to incorporate a remagnetisation mechanism of the fully demagnetised dysprosium unit cells into the modelling. In contrast, the modelled remagnetisation under the condition of non-saturated magnetic stress describes well the measurements for fluences below $2.9\,\frac{\mathrm{mJ}}{\mathrm{cm}^2}$.

Under the condition of non-saturated magnetic stress, the time-dependent energy density stored in the unit cell determines both the energy density in the phonons and the magnetic excitations. This assumption leads to a simultaneous cooling of the phonons and magnetic excitations via heat diffusion. The identical cooling behaviour results in a time-independent fraction of energy density stored in the subsystems after the phonon-spin coupling. The constant energy distribution describes to first order an equilibrium between the subsystems on the nanosecond timescale. This situation changes with the occurrence of fully demagnetised unit cells for high fluences. The measurements in figure 6.8 display an increasing contraction of dysprosium with time under the condition of saturated magnetic stress indicated by the bipolar shape of the niobium strain. This additional contraction arising on the timescale dominated by heat diffusion is captured by the model (see figure 6.11) and increases for high fluences and initial sample temperatures near T_N. The model captures the increasing contraction of dysprosium by neglecting the remagnetisation of the fully demagnetised unit cells exhibiting saturated magnetic stress. Therefore, my analysis relates the additional contraction to a remaining magnetic stress provided by the fully demagnetised unit cells while the expansive phonon stress decreases due to heat diffusion. In conclusion, the delayed remagnetisation of the fully demagnetised unit cells causes a local non-equilibrium between phonons and spins on the nanosecond timescale as observed by *von Reppert et al.* [27].

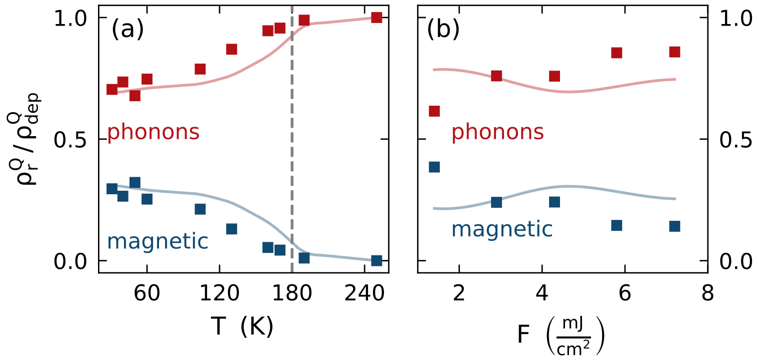

Figure 6.12: Distribution of energy density between the phonons and the magnetic excitations in the heterostructure for (a) different initial sample temperatures for a fluence of $7.2\,\frac{\mathrm{mJ}}{\mathrm{cm}^2}$ and for (b) different fluences at an initial sample temperature of $130\,\mathrm{K}$. The red squares denote the thermal expansion of niobium normalised to the expansion at $250\,\mathrm{K}$ with $7.2\,\frac{\mathrm{mJ}}{\mathrm{cm}^2}$. The blue squares denote the fraction of the energy density stored in the magnetic subsystem as difference to unity. The solid lines denote the interpolated normalised maximum expansion of niobium provided by the model that matches the temperature- and fluence dependence. Under the condition of saturated magnetic stress, the model underestimates the expansion of niobium due to the neglected remagnetisation of the fully demagnetised unit cells.

In the following I analyse the temperature- and fluence-dependent phononic heat transport in more detail by extracting the temperature- and fluence-dependent expansion of niobium. Figure 6.12 summarises the findings and highlights the role of the magnetic subsystem as a saturable heat sink that reduces the amount of energy transported by the phonons into niobium. The red squares denote the measured thermal expansion of niobium that I determine by fitting the temporal shape from the paramagnetic phase to the transient strain between 300 and $3000\,\mathrm{ps}$. The resulting temperature- and fluence-dependent amplitude is normalised to the expansion at $250\,\mathrm{K}$ and a fluence of $F = 7.2\,\frac{\mathrm{mJ}}{\mathrm{cm}^2}$. The difference to unity determines the fraction of the total deposited energy stored in the magnetic subsystem on nanosecond timescale (blue squares). Figure 6.12(a) displays a decreased thermal expansion below the Néel temperature $T_\mathrm{N} = 180\,\mathrm{K}$ with a maximum amount of energy stored in the magnetic system at $31\,\mathrm{K}$. This dependence is in agreement with the thermal expansion described by the model (solid lines). However, the neglected remagnetisation of the fully demagnetised unit cells overestimates the energy stored in the magnetic system in the model. This overestimation becomes pronounced at temperatures slightly below the magnetic order temperature where most of the layer exhibits saturated magnetic stress.

Figure 6.12(b) displays the thermal expansion normalised to the fluence as function of the excitation fluence at $130\,\mathrm{K}$. The explicit fluence dependence of the thermal expansion normalised to the fluence indicates the saturation of the magnetic stress that enhances the fraction of energy in the phononic heat transport. With decreasing fluence the fully demagnetised fraction of the layer decreases and the overestimation of the energy stored in the magnetic subsystem by the model vanishes. The Grüneisen model of the spatio-temporal stress predicts a minimum in the fluence-normalised thermal expansion of niobium between 4 and $6\,\frac{\mathrm{mJ}}{\mathrm{cm}^2}$ where the magnetic system is just saturated. For higher fluences the saturation of the magnetic stress enhances the fraction of energy stored in the phonons, while for lower fluences the magnetic subsystem transfers energy back to the phonons during remagnetisation. For low fluences the small absolute fluence uncertainty becomes large in this representation due to the normalisation to the fluence. The deviation to the measurements for $1.4\,\frac{\mathrm{mJ}}{\mathrm{cm}^2}$ may be related to this effect.

In the following paragraphs I present the modelled subsystem-separated spatio-temporal stress at the different initial sample temperatures and for the different excitation fluences depicted in figures 6.13 and 6.15, respectively. The one-dimensional linear-chain model of masses and springs

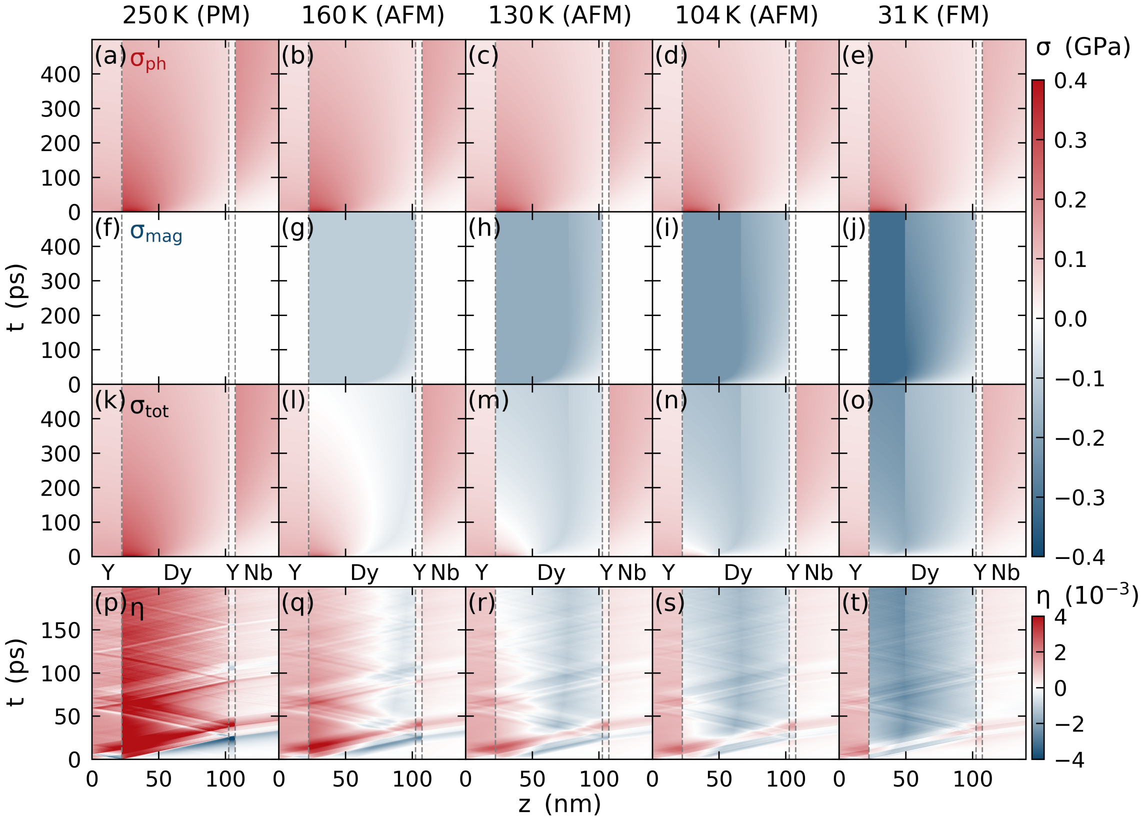

Figure 6.13: Modelled spatio-temporal stress and strain in the heterostructure at different initial sample temperatures and a fluence of $7.2\,\frac{\mathrm{mJ}}{\mathrm{cm}^2}$. The superposition of the phononic stress (a-e) and the magnetic stress (f-j) determines the total lattice stress (k-o). The Matlab library udkm1Dsim calculates the spatio-temporal expansion and propagating strain pulses (p-t) from the spatio-temporal total stress. Decreasing the temperature below $T_\mathrm{N} = 180\,\mathrm{K}$ enables magnetic excitations that contribute a finite contractive stress. At high temperatures almost the complete dysprosium layer is fully demagnetised and the tensile electron-phonon stress dominates. With decreasing temperature the fraction of the fully demagnetised dysprosium decreases and the contractive magnetic stress dominates. The change of the total stress is accompanied with an enhanced contraction of dysprosium and a reduced bipolar strain wave. (Adopted from [29])

of the modular Matlab library udkm1Dsim [124] calculates the spatio-temporal strain of the heterostructure including the coherently excited strain pulses from the total spatio-temporal stress as superposition of the contributions of phonons and spins. This is analogous to the inhomogeneous wave equation (2.26) with external driving stress discussed in section 2.2.2. The separation of the total stress into the contributions from the phonons and the magnetic excitations exemplifies the influence of the temperature- and fluence-dependent magnetic stress on the strain response.

Figure 6.13 displays the temperature-dependent magnetic excitations and the change of the total spatio-temporal stress under the systematic variation of the initial sample temperature. This temperature-dependent stress rationalises the temperature dependence of the transient mean strain of dysprosium and the driven strain pulses that are detected in the buried detection layer. The temperature dependence of the total stress mainly originates from the temperature-dependent saturation of the magnetic stress. In contrast, the stress contribution of the phonons exhibit a nearly temperature-independent spatio-temporal shape that scales by the energy density transferred locally to the magnetic excitations. At 160 K the dysprosium layer is fully demagnetised after 200 ps and the total stress is mostly dominated by the tensile electron-phonon stress up to 400 ps. With decreasing temperature the fraction of the layer exhibiting a saturated magnetic stress decreases and the contractive magnetic stress becomes dominant down to $31\,\mathrm{K}$ where the total stress is exclusively negative. Additionally, decreasing the initial sample temperature leads to a faster domination of the contractive magnetic stress at the front side of the layer, which corresponds to the changing sign of the mean strain after $35\,\mathrm{ps}$ at $130\,\mathrm{K}$. The subsequent increasing contraction of dysprosium results from the heat diffusion that induces both an additional excitation of not fully demagnetised unit cells and a cooling of the phonons. The transport of energy density to the backside of the layer provides the additional excitation of the non-saturated magnetic subsystem indicated by the growing fraction of the layer showing saturated magnetic stress (g-j). The cooling of the phonons in dysprosium to the subsequent layers is indicated by the reduced phononic stress (a-e). The domination of the magnetic stress at the front side of the layer clearly demonstrates the neglected remagnetisation of the fully demagnetised unit cells. Especially the excitation of the spins by phonon-spin coupling on the $15\,\mathrm{ps}$ timescale is clearly observable in the magnetic stress contribution and leads to a time-dependent decrease of the total stress. The reduced total tensile stress at the front side of the layer at low temperatures corresponds to a reduced amplitude of the driven bipolar strain wave at the yttrium-dysprosium interface as displayed by the strain maps (p-t). In contrast, the increased contraction of dysprosium at the backside of the layer due to the increased amount of energy storable to the magnetic system at low temperatures drives an expansion propagating into the niobium layer. In the intermediate temperature-range the unconventional strain pulses are a superposition of the uni-polar expansion of niobium driven by the contraction at the backside of dysprosium and the bipolar strain wave driven by the total tensile stress at the front side of the layer.

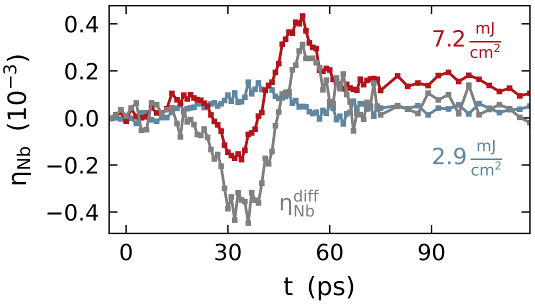

Figure 6.14: Difference in the fluence-normalised mean strain of niobium for 2.9 and $7.2\,\frac{\mathrm{mJ}}{\mathrm{cm}^2}$ at $130\,\mathrm{K}$. The difference $\eta_{\mathrm{Nb}}^{\mathrm{diff}}$ exhibits a bipolar shape. This difference essentially confirms that the high fluence mostly leads to the excitation of expansive stress by phonons. Furthermore, it separates the unconventional strain pulses into the contribution from the contractive total stress at the bottom and the expansive total stress at the top side of the dysprosium layer.

This superposition is exemplified in figure 6.14 that displays the mean strain of niobium for a fluence of 2.9 and $7.2\,\frac{\mathrm{mJ}}{\mathrm{cm}^2}$ at $130\,\mathrm{K}$. The stress and strain maps for the systematic variation of the excitation fluence in figure 6.15 display the vanishing saturation of the magnetic stress for $2.9\,\frac{\mathrm{mJ}}{\mathrm{cm}^2}$. in contrast, the magnetic stress saturates for $7.2\,\frac{\mathrm{mJ}}{\mathrm{cm}^2}$ and the tensile phonon stress dominates at the front side of the layer. The qualitative difference in the total stress in dysprosium induces a uni-polar expansion of niobium for the low fluence and a bipolar strain pulse preceded by an expansion for the high fluence. The difference in the transient fluence-normalised strain of niobium η_3^{diff} relates to the saturation of the magnetic stress for $7.2\,\frac{\mathrm{mJ}}{\mathrm{cm}^2}$. This difference is depicted in figure 6.14 by the gray line and exhibits a bipolar shape. This essentially confirms that the high fluence mostly leads to the excitation of expansive stress by phonons, which drives a bipolar strain wave. The superposition with the contraction-driven fast expansion results in the unconventional strain pulse consisting of an asymmetric bipolar strain wave preceded by an expansion.

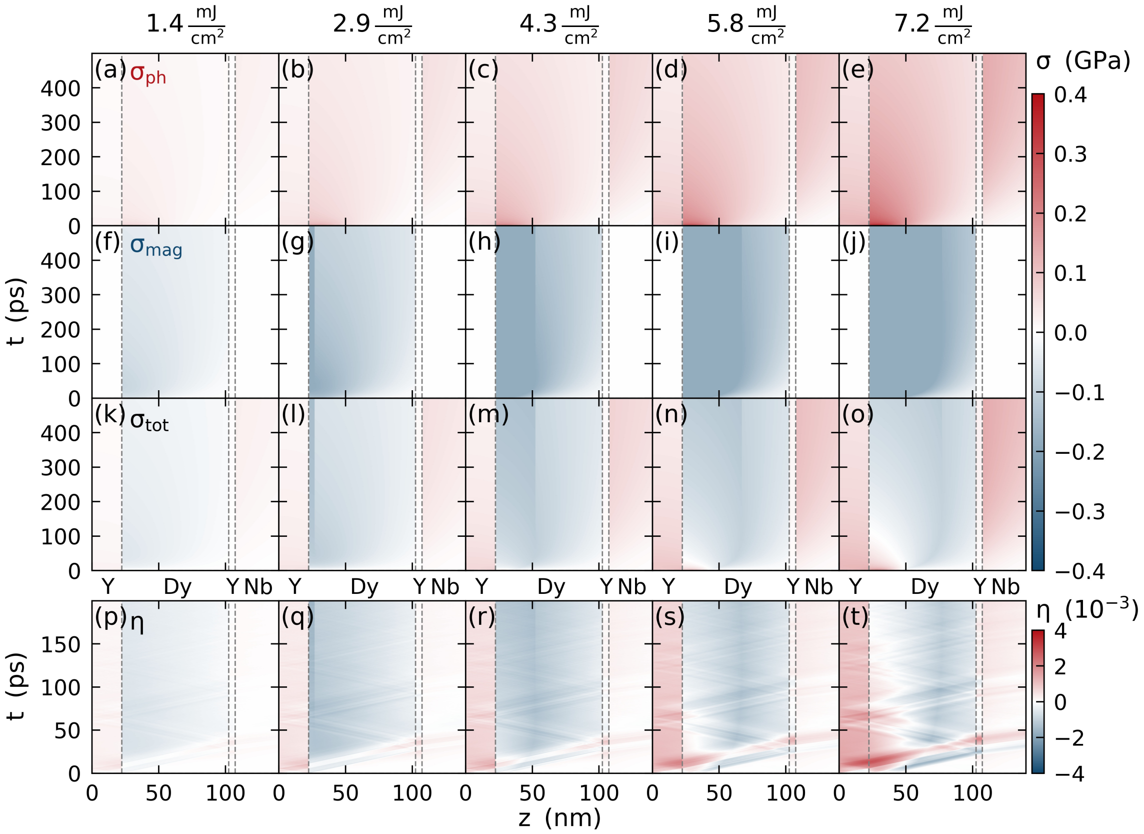

Figure 6.15: Modelled spatio-temporal stress and strain in the heterostructure induced by different fluences at 130 K. The superposition of the phononic stress (a-e) and the magnetic stress (f-j) determine the total lattice stress (k-o). The MATLAB library UDKM1DSIM calculates the spatio-temporal expansion and propagating strain pulses (p-t) from the spatio-temporal total stress. High fluences saturate the magnetic energy reservoir almost everywhere in the dysprosium layer and most of the energy density is stored in the phonons leading to an expansive total stress at the front side of the layer. With decreasing fluence the energy density exceeding the saturation level of the magnetic stress decreases and the contractive magnetic stress becomes dominant. The increasingly dominant magnetic stress suppresses the bipolar strain wave. (Adopted from [29])

The subsystem-separated spatio-temporal stress for the different excitation fluences in figure 6.15 at an initial sample temperature of 130 K displays a similar dependence of the total stress with increasing fluence as with increasing initial sample temperature (see figure 6.13). For higher fluences the laser-deposited energy density exceeds the energy density storable to the magnetic subsystem and the dysprosium layer at the front side exhibits saturated magnetic stress. This saturation vanishes with decreasing fluences and the magnetic stress becomes dominant in the complete dysprosium layer. The domination of the magnetic stress also in the front side of the layer changes the strain response of niobium from bipolar to uni-polar. Furthermore, the magnetic subsystem of the not fully demagnetised unit cells cools on the same timescale as the phonons due to heat diffusion. In contrast, the model neglects the remagnetisation of the fully demagnetised unit cells as displayed for $4.3\,\frac{\mathrm{mJ}}{\mathrm{cm}^2}$ in figure 6.15(h). The saturated magnetic stress in the front part of the layer remains up to 500 ps, while in the neighbouring region of the layer the magnetic stress decreases due to heat diffusion. The remaining excitation of the fully demagnetised unit cells provides a remaining contractive stress that causes an increasing contraction of dysprosium during the cooling of the phonons to the subsequent layers.

6.4 Demagnetisation probed by double-pulse excitation

In a double-pulse excitation scheme the strain response to the second laser pulse reveals the excitation of the magnetic subsystem by the first pulse due to the saturability of the magnetic energy reservoir. In this section I present the strain response of dysprosium to a double-pulse excitation with a systematic variation of the fluence of the first pulse. The modelling of the strain response by the model presented in section 6.2 provides the spatio-temporal magnetic stress induced by the second excitation. With increasing fluence the first pulse fully demagnetises the transducer. Therefore, the contractive stress induced by the second pulse vanishes in the fully demagnetised part of the layer resulting in a dominant tensile stress by the phonons.

Figure 6.16 briefly provides an overview of the pump-probe experiment using a double-pulse excitation scheme. The experiment is conducted at $35\,\mathrm{K}$ and an in-plane magnetic field of $600\,\mathrm{mT}$ that shifts the first order phase transition to $90\,\mathrm{K}$. The strain response to the two excitations with a pump-pump delay of $100\,\mathrm{ps}$ of dysprosium (a) and niobium (b) shows a pronounced fluence dependence. In panel (a) the filled dots denote the strain response to the first excitation at the pump-probe delay $t = 0\,\mathrm{ps}$. For the fluence of $8\,\frac{\mathrm{mJ}}{\mathrm{cm}^2}$ the delayed maximum contraction indicates a saturated magnetic stress as discussed in the context of figure 6.11. The saturated magnetic stress limits the contraction of dysprosium that increases with the fluence for lower fluences. The open squares denote the strain response to both excitations. The difference to the strain response to only the first excitation yields the strain response to the second delayed pump pulse. The strain response of dysprosium to the second pulse changes from purely expansive for a high fluence of the first pulse to purely contractive for a low fluence of the first pulse. This change for dysprosium is accompanied with a change of the driven strain pulse detected in niobium from a bipolar to a uni-polar shape. In consideration of the findings in the last section the strain response to the

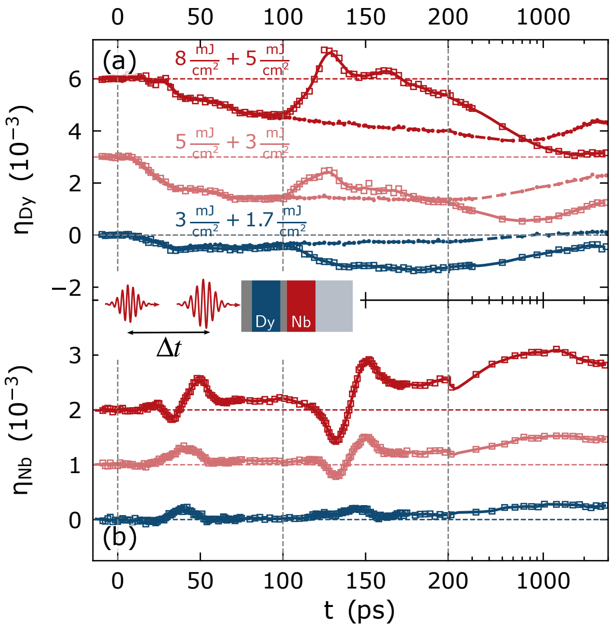

Figure 6.16: Strain response to a double-pulse excitation with the pump-pump delay of $\Delta t = 100\,\mathrm{ps}$ and an in-plane magnetic field of $600\,\mathrm{mT}$ at $35\,\mathrm{K}$. The double-pulse excitation scheme in a pump-probe experiment using ultrafast X-ray diffraction is sketched in the inset. The transient strain of dysprosium (a) and niobium (b) exhibits a clear signature of the second laser excitation after $100\,\mathrm{ps}$ that changes with the fluence of the double-pulse excitation. The filled dots denote the strain response of dysprosium in the absence of a second pulse, while the open squares denote the strain response to both delayed excitations.

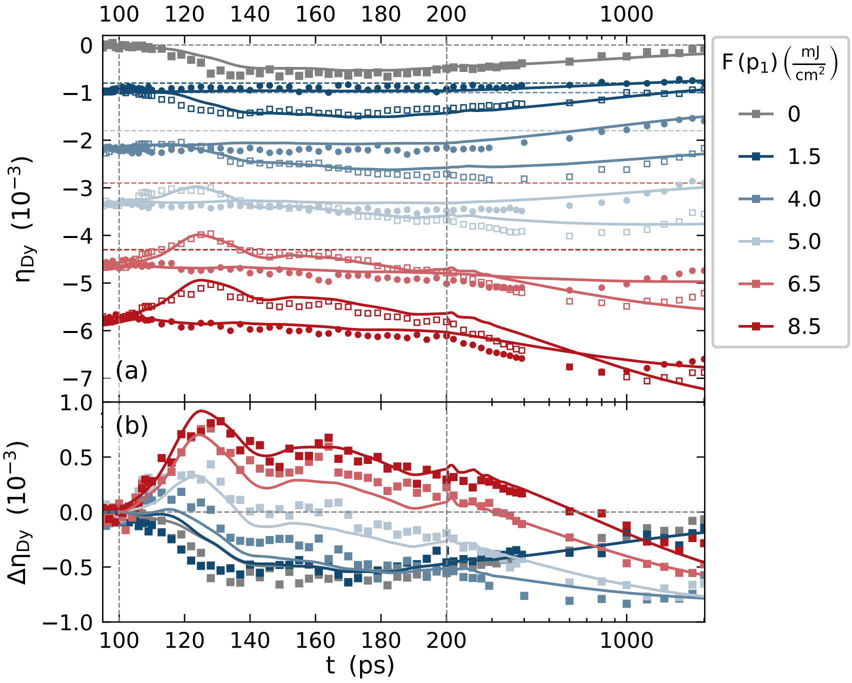

Figure 6.17: Strain response to a double-pulse excitation with varying fluence of the first pulse. The difference between the strain response to the first pulse (dots) and to both pulses (squares) in (a) defines the transient strain induced by the second excitation (b). The gray squares correspond to the strain response to only the second pulse with a fluence of $1.8\,\frac{mJ}{cm^2}$. The solid lines denote the modelled strain response to both the first pulse with different fluences and the double-pulse excitation under constant fluence of the second pulse. With increasing fluence of the first pulse the transient strain induced by the second pulse becomes expansive.

second excitation reveals a full demagnetisation of the transducer for the highest fluence and a non-saturated magnetic stress in the case of the lowest fluence combination.

The changing strain response to the second excitation in figure 6.16 originates from both the increasing fluence of the first and the second pulse. To investigate the saturation of the magnetic stress by the first pulse the fluence of the second pulse has to be kept constant. Under this condition, the changing strain response exclusively depends on the saturation of the magnetic stress by the first pulse due to the constant energy density deposited by the second pulse. Figure 6.17(a) displays the strain response to the first pulse (dots) and to both pulses (squares) with a pump-pump delay of $100\,$ps. The gray squares denote the strain response to the second pump-pulse in the absence of a preceded excitation. While the fluence of the first pulse is systematically varied from 1.5 to $8.5\,\frac{mJ}{cm^2}$, the fluence of the second pump pulse is kept constant $1.8\,\frac{mJ}{cm^2}$. The horizontal dashed lines denote the zero-strain of the corresponding measurement that are shifted for clarity. The measurements are conducted at $60\,$K with an applied external magnetic field of $600\,$mT along the in-plane direction that shifts the first order ferromagnetic phase transition to $90\,$K. The solid lines denote the modelled strain response that describes well the strain response to both the first excitation and the double-pulse excitation. The model underestimates the contraction of dysprosium originating from the first order phase transition, because the model is based on temperature-independent Grüneisen constants. This underestimation is already observable for the measurement at $31\,$K in figure 6.11(a). Thus, I shift the modelled strain to the measurement results at $100\,$ps by a fluence-dependent offset. However, since the first pulse transiently heats above the Curie temperature, the first order phase transition barely influences the strain response to the second pulse that is well predicted by the model.

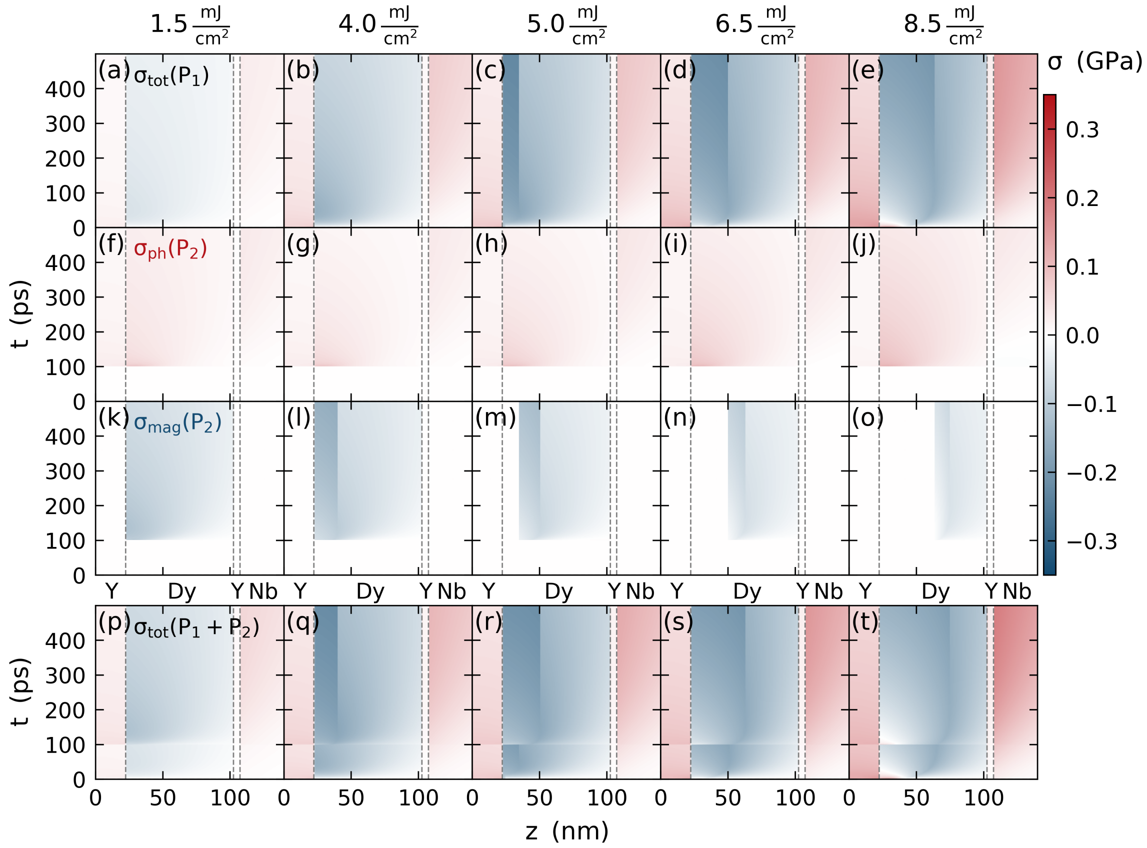

Figure 6.18: Spatio-temporal stress induced by the first and the second excitation in a double-pulse excitation scheme. The total stress induced by the first pulse (P_1) (a-e) determines in combination with the total stress induced by the double-pulse excitation (p-t) the total stress induced by the second excitation. This total stress is separated by the Grüneisen model into the contribution from phonons (f-j) and magnetic excitations (k-o). The fully demagnetised part of the dysprosium layer by the first pulse for high fluences is not further excitable by the second pulse, so that the additional magnetic stress vanishes in this part of the layer. The reduced energy density transferred to the magnetic subsystem enhances the phonon stress. The total stress induced by the second pulse becomes tensile at the front side of the layer as indicated by the increasing total stress after the second excitation in (q-t).

The difference between the strain response to the first pulse and to the double-pulse excitation defines the induced strain by the second excitation due to the linear dependence of the strain on the energy density. Figure 6.17(b) displays the strain response to the second excitation with a constant fluence. With increasing fluence of the first pulse the strain induced by the second excitation changes from purely contractive to purely expansive within the first 500 ps. The expansion of dysprosium indicates the saturation of the magnetic stress by the double-pulse excitation. The deviation of the modelled strain response of the first pulse on the nanosecond timescale for fluences above $5\,\frac{\mathrm{mJ}}{\mathrm{cm}^2}$ is related to the neglected remagnetisation of the fully demagnetised dysprosium unit cells. This observation indicates the saturation of the magnetic stress by the first excitation. The saturation of the magnetic stress by the first pulse inhibits a further excitation of the magnetic system in fully demagnetised unit cells. Furthermore, the second excitation saturates the magnetic stress in the bottom part of the layer that was previously not fully demagnetised. In total, the saturation of the magnetic stress by both excitations reduces the contractive stress induced by the second pulse. This enhances the fraction of energy density stored in the phonons. Therefore, the total laser-induced stress becomes expansive and results in an expansion of dysprosium.

Further insight is provided by the subsystem-separated spatio-temporal stress that can be obtained from the Grüneisen model. The analysis of the measured results identifies the saturation of the magnetic stress by both the first and the second pulse to be responsible for the changing response to the second pulse with increasing fluence of the first excitation. The spatio-temporal stress induced by the first pulse in figure 6.18(a-e) and the phononic (f-j) and magnetic (k-o) stress induced by the second pulse separate the two contributions. The subsystem-separated stress induced by the second excitation is determined by the difference between the total stress induced by the double-pulse excitation (p-t) and the first pulse (a-e). For fluences above $4\,\frac{\mathrm{mJ}}{\mathrm{cm}^2}$ the first pulse saturates the magnetic stress and with increasing fluence the fraction of the dysprosium transducer exhibiting saturated magnetic stress increases. This part of the dysprosium layer is fully demagnetised and no more energy is storable to the magnetic system. Thus, the magnetic stress induced by the second pulse vanishes in the fully demagnetised part of the layer as depicted in (m-o). In this case the full demagnetisation by the first pulse mainly reduces the contractive stress induced by the second pulse. The reduced energy density transferred to the magnetic system also increases the phonon stress in comparison to the low fluence limit (f) as observable in (h-j). In contrast, for lower fluences the saturation of the magnetic stress by the second pulse determines the reduced contractive stress in dysprosium. However, in both cases, the reduced excitation of the magnetic system results in an enhanced total expansive stress after the second excitation at the front side of the dysprosium transducer (p-t). This total expansive stress causes the expansion of dysprosium induced by the second pulse observed in the ultrafast X-ray diffraction experiment.

Chapter Seven

Summary and Outlook

In this thesis I analysed the strain response of the laser-excited strontium ruthenate and dysprosium thin films measured by ultrafast X-ray diffraction. The ultrafast expansion and the driven picosecond strain pulses in both metals change due to the additional contractive stress provided by the magnetic excitations that occur below the magnetic order temperature. The modelling of the picosecond strain response reveals the spatio-temporal laser-induced stress that is the superposition of the contributions from phonons and magnetic excitations. I used the thermodynamic Grüneisen concept to separate the total spatio-temporal stress into the subsystem contributions. This approach linearly relates the deposited energy density in the subsystems to a stress contribution via subsystem-specific Grüneisen constants.

I determined the anisotropic Grüneisen constants using the equilibrium thermal expansion of the bulk materials. In both metals the arising magnetic order provides a contractive stress that counteracts the expansion due to anharmonic phonon-phonon interactions. In thermal equilibrium the expansion is driven by an external stress and a Poisson stress that originates from the thermal expansion along the other crystal directions. The vanishing magnetic stress contribution in the paramagnetic phase enables the separation of the external stress into the contributions of phonons and magnetic excitations. The subsystem-separated heat capacity relates the temperature-dependent external stress contributions to the energy density stored in each subsystem. The resulting linear dependence determines the Grüneisen constants. On ultrafast timescales the thin film geometry restricts the lattice response to the out-of-plane direction. The underlying out-of-plane stress is determined by the Grüneisen constants along the corresponding crystal direction.

The application of the Grüneisen model to the strain response of strontium ruthenate and dysprosium exemplifies the possibility to describe the spatio-temporal stress in magnetic transducers under different complementary conditions. In strontium ruthenate the homogeneous excitation and the ultrafast equilibration of the subsystems facilitate the analysis. In contrast, the inhomogeneous excitation of dysprosium and the long-lasting non-equilibrium of phonons and spins require the explicit modelling of the subsystem coupling. The transient full demagnetisation of the magnetic transducer is equivalent to a maximum amount of energy density storable to the magnetic excitations. This saturation of the magnetic stress is responsible for the temperature and fluence dependence of the strain response upon laser excitation.

In strontium ruthenate I studied the temperature-dependent total stress for the low and the high fluence regime. The homogeneous excitation of the thin film in combination with the ultrafast equilibration of the subsystems results in a time-independent total stress also below the magnetic order temperature. The quasi-instantaneous expansive total stress results in a temperature-independent shape of the driven strain pulses. In the high fluence regime the laser excitation saturates the magnetic stress at all initial sample temperatures. This is verified by a temperature-independent stress induced by a second delayed excitation. Under this condition the total stress depends on the temperature-dependent squared magnetisation, which is proportional to the temperature-dependent integral of the magnetic heat capacity. In contrast, in the low fluence limit the total stress follows

the temperature-dependent magnetic heat capacity. The vanishing saturation at low temperatures and the arising contractive magnetic stress slightly below the magnetic order temperature lead to a step-like change of the total laser-induced stress at the Curie temperature.
In the inhomogeneously excited dysprosium transducer the saturation of the magnetic stress results in a depth-dependent sign of the total stress. At the front side of the layer the full demagnetisation limits the energy density transferred to the magnetic subsystem and the tensile electron-phonon stress dominates. At the backside of the layer the non-saturated magnetic stress dominates the expansive phonon stress and the total stress becomes contractive. The resulting total stress drives strain pulses with unconventional shape that are detected in a buried niobium detection layer. The mean strain of the niobium layer shows an asymmetric bipolar strain wave preceded by a fast expansion within the first picoseconds. The analysis of the spatio-temporal stress relates the fast expansion to the contraction of dysprosium at the backside and the superimposed bipolar strain wave to the tensile total stress at the front side of dysprosium. A double-pulse excitation scheme was used to further investigate the fluence-dependent saturation of the magnetic stress. In that scheme the fluence of the second pump pulse is kept constant whereas the fluence of the first pulse is varied systematically. My analysis showed the spatial extension of the fully demagnetised region in the dysprosium layer. For the fully demagnetised unit cells the further excitation of the magnetic subsystem is inhibited and all additional absorbed energy excites the phonon system. The resulting expansion of dysprosium driven by the second excitation is well captured by the Grüneisen model.

In further experiments the remagnetisation of the fully demagnetised unit cells could be studied using a double-pulse excitation with a variation of the pump-pump delay. The remagnetisation of the fully demagnetised unit cells will enable the excitation of the magnetic subsystem by the second pulse. Therefore, the variation of the pump-pump delay would probe the time-dependent saturation of the magnetic stress induced by the first excitation. Furthermore, the presented double-pulse experiments could be extended by additionally measuring the strain of niobium. Since the expansion of niobium within the first picoseconds relates to the contraction of dysprosium at the backside, the reduced expansion of niobium with increasing fluence reveals the spatial extension of the not fully demagnetised part of dysprosium. These experiments demonstrate the possibility to study the spatio-temporal excitation of the magnetic subsystem independently of the type of the magnetic order using ultrafast X-ray diffraction with double-pulse excitation. A further investigation of strontium ruthenate could answer the more fundamental question which magnetic states are excitable on ultrafast timescales. In the low fluence regime the temperature-dependent total stress will reveal the magnetic heat capacity on ultrafast timescales. However, the used plasma X-ray source with a pronounced instrument function and a low X-ray flux cannot perform this experiment with the required resolution in strain. It could be conducted at a synchrotron with a minimum time resolution of around $20\,\mathrm{ps}$ or at the free electron laser.
In conclusion, I presented the analysis of the temperature- and fluence-dependent strain response of two different magnetic metals using the thermodynamic Grüneisen concept to describe the stress contributions of both phonons and magnetic excitations. This thesis provides a detailed analysis of the magnetic stress contribution that relates to the spatio-temporal excitation of the magnetic subsystem and therefore provides insights into the subsystem-coupling and energy transfer timescales. Next to the temperature- and fluence-dependent mean stress in the optically excited transducer, I studied the strain pulses driven by the saturable magnetic stress.

Bibliography

[1] C. Thomsen, H. T. Grahn, H. J. Maris and J. Tauc: "Surface generation and detection of phonons by picosecond light pulses", *Physical Review B* 34, 4129 (1986)

[2] O. Matsuda, M. C. Larciprete, R. L. Voti and O. B. Wright: "Fundamentals of picosecond laser ultrasonics", *Ultrasonics* 56, 3 (2015)

[3] P. Ruello and V. E. Gusev: "Physical mechanisms of coherent acoustic phonons generation by ultrafast laser action", *Ultrasonics* 56, 21 (2015)

[4] O. B. Wright: "Ultrafast nonequilibrium stress generation in gold and silver", *Physical Review B* 49, 9985 (1994)

[5] T. Saito, O. Matsuda and O. Wright: "Picosecond acoustic phonon pulse generation in nickel and chromium", *Physical Review B* 67, 205421 (2003)

[6] M. Nicoul, U. Shymanovich, A. Tarasevitch, D. von der Linde and K. Sokolowski-Tinten: "Picosecond acoustic response of a laser-heated gold-film studied with time-resolved x-ray diffraction", *Applied Physics Letters* 98, 191902 (2011)

[7] G. Tas and H. J. Maris: "Electron diffusion in metals studied by picosecond ultrasonics", *Physical Review B* 49, 15046 (1994)

[8] M. Lejman, V. Shalagatskyi, O. Kovalenko, T. Pezeril, V. V. Temnov and P. Ruello: "Ultrafast optical detection of coherent acoustic phonons emission driven by superdiffusive hot electrons", *JOSA B* 31, 282 (2014)

[9] S. Nie, X. Wang, H. Park, R. Clinite and J. Cao: "Measurement of the electronic Grüneisen constant using femtosecond electron diffraction", *Physical review letters* 96, 025901 (2006)

[10] X. Wang, S. Nie, J. Li, R. Clinite, M. Wartenbe, M. Martin, W. Liang and J. Cao: "Electronic Grüneisen parameter and thermal expansion in ferromagnetic transition metal", *Applied Physics Letters* 92, 121918 (2008)

[11] A. Von Reppert et al.: "Watching the vibration and cooling of ultrathin gold nanotriangles by ultrafast x-ray diffraction", *The Journal of Physical Chemistry C* 120, 28894 (2016)

[12] J. Pudell, A. Maznev, M. Herzog, M. Kronseder, C. Back, G. Malinowski, A. von Reppert and M. Bargheer: "Layer specific observation of slow thermal equilibration in ultrathin metallic nanostructures by femtosecond X-ray diffraction", *Nature communications* 9, 1 (2018)

[13] J.-E. Pudell, M. Mattern, M. Hehn, G. Malinowski, M. Herzog and M. Bargheer: "Heat Transport without Heating?—An Ultrafast X-Ray Perspective into a Metal Heterostructure", *Advanced Functional Materials* 2004555 (2020)

[14] J. Pudell: "Lattice Dynamics observed with x-ray diffraction" Phd thesis, University of Potsdam (2020)

[15] G. D. Barrera, J. A. O. Bruno, T. Barron and N. Allan: "Negative thermal expansion", *Journal of Physics: Condensed Matter* 17, R217 (2005)

[16] T. Barron and G. K. White: *Heat capacity and thermal expansion at low temperatures* (Springer Science & Business Media, 1999)

[17] E. Grüneisen: "Theorie des festen Zustandes einatomiger Elemente", *Annalen der Physik* 344, 257 (1912)

[18] G. White: "Thermal expansion of magnetic metals at low temperatures", *Proceedings of the Physical Society* 86, 159 (1965)

[19] T. Barron, J. Collins and G. White: "Thermal expansion of solids at low temperatures", *Advances in Physics* 29, 609 (1980)

[20] L. McKeehan and P. Cioffi: "Magnetostriction in permalloy", *Physical Review* 28, 146 (1926)

[21] E. R. Callen and H. B. Callen: "Static magnetoelastic coupling in cubic crystals", *Physical Review* 129, 578 (1963)

[22] E. Callen and H. B. Callen: "Magnetostriction, forced magnetostriction, and anomalous thermal expansion in ferromagnets", *Physical Review* 139, A455 (1965)

[23] M. Doerr, M. Rotter and A. Lindbaum: "Magnetostriction in rare-earth based antiferromagnets", *Advances in Physics* 54, 1 (2005)

[24] F. Darnell: "Temperature dependence of lattice parameters for Gd, Dy, and Ho", *Physical Review* 130, 1825 (1963)

[25] T. Kiyama, K. Yoshimura, K. Kosuge, Y. Ikeda and Y. Bando: "Invar effect of $SrRuO_3$: Itinerant electron magnetism of Ru 4d electrons", *Physical Review B* 54, R756 (1996)

[26] C. von Korff Schmising et al.: "Ultrafast magnetostriction and phonon-mediated stress in a photoexcited ferromagnet", *Physical Review B* 78, 060404 (2008)

[27] A. von Reppert, J. Pudell, A. Koc, M. Reinhardt, W. Leitenberger, K. Dumesnil, F. Zamponi and M. Bargheer: "Persistent nonequilibrium dynamics of the thermal energies in the spin and phonon systems of an antiferromagnet", *Structural Dynamics* 3, 054302 (2016)

[28] J. Pudell, A. von Reppert, D. Schick, F. Zamponi, M. Rössle, M. Herzog, H. Zabel and M. Bargheer: "Ultrafast negative thermal expansion driven by spin disorder", *Physical Review B* 99, 094304 (2019)

[29] A. von Reppert, M. Mattern, J.-E. Pudell, S. P. Zeuschner, K. Dumesnil and M. Bargheer: "Unconventional picosecond strain pulses resulting from the saturation of magnetic stress within a photoexcited rare earth layer", *Structural Dynamics* 7, 024303 (2020)

[30] S. O. Mariager et al.: "Structural and magnetic dynamics of a laser induced phase transition in FeRh", *Physical Review Letters* 108, 087201 (2012)

[31] A. Reid et al.: "Beyond a phenomenological description of magnetostriction", *Nature communications* 9, 1 (2018)

[32] A. von Reppert et al.: "Spin stress contribution to the lattice dynamics of FePt", *Science advances* 6, eaba1142 (2020)

[33] A. Lord Jr: "Thermal expansion due to spin waves at low temperatures", *Journal of Physics and Chemistry of Solids* 28, 517 (1967)

[34] E. Fawcett: "Magnetic Grüneisen parameters in 3d transition metals", *Physica B: Condensed Matter* 159, 12 (1989)

[35] A. Koc, M. Reinhardt, A. Von Reppert, M. Rössle, W. Leitenberger, K. Dumesnil, P. Gaal, F. Zamponi and M. Bargheer: "Ultrafast x-ray diffraction thermometry measures the influence of spin excitations on the heat transport through nanolayers", *Physical Review B* 96, 014306 (2017)

[36] A. Koc, M. Reinhardt, A. von Reppert, M. Rössle, W. Leitenberger, M. Gleich, M. Weinelt, F. Zamponi and M. Bargheer: "Grueneisen-approach for the experimental determination of transient spin and phonon energies from ultrafast x-ray diffraction data: Gadolinium", *Journal of Physics: Condensed Matter* 29, 264001 (2017)

[37] W. Li, B. Buford, A. Jander and P. Dhagat: "Acoustically assisted magnetic recording: a new paradigm in magnetic data storage", *IEEE transactions on magnetics* 50, 37 (2014)

[38] I. Camara, J.-Y. Duquesne, A. Lemaître, C. Gourdon and L. Thevenard: "Field-free magnetization switching by an acoustic wave", *Physical Review Applied* 11, 014045 (2019)

[39] W. Challener et al.: "Heat-assisted magnetic recording by a near-field transducer with efficient optical energy transfer", *Nature photonics* 3, 220 (2009)

[40] D. Weller, G. Parker, O. Mosendz, A. Lyberatos, D. Mitin, N. Y. Safonova and M. Albrecht: "FePt heat assisted magnetic recording media", *Journal of Vacuum Science & Technology B, Nanotechnology and Microelectronics: Materials, Processing, Measurement, and Phenomena* 34, 060801 (2016)

[41] S. Zeuschner et al.: "Tracking picosecond strain pulses in heterostructures that exhibit giant magnetostriction", *Structural Dynamics* 6, 024302 (2019)

[42] M. Deb, E. Popova, M. Hehn, N. Keller, S. Mangin and G. Malinowski: "Picosecond acoustic-excitation-driven ultrafast magnetization dynamics in dielectric Bi-substituted yttrium iron garnet", *Physical Review B* 98, 174407 (2018)

[43] O. Kovalenko, T. Pezeril and V. V. Temnov: "New concept for magnetization switching by ultrafast acoustic pulses", *Physical Review Letters* 110, 266602 (2013)

[44] L. Thevenard, I. Camara, S. Majrab, M. Bernard, P. Rovillain, A. Lemaître, C. Gourdon and J.-Y. Duquesne: "Precessional magnetization switching by a surface acoustic wave", *Physical Review B* 93, 134430 (2016)

[45] R. Gross and A. Marx: *Festkörperphysik* (Walter de Gruyter GmbH & Co KG, 2018)

[46] N. Ashcroft and D. Mermin: *Solid State Physics* (1976)

[47] D. Royer and E. Dieulesaint: *Elastic Waves in Solids I - Free and Guided Propagation* (2000)

[48] A. Bojahr: "Hypersound Interaction Studied by Time-Resolved Inelastic Light and X-Ray Scattering" Ph.D. thesis, University of Potsdam (2015)

[49] D. Schick, M. Herzog, A. Bojahr, W. Leitenberger, A. Hertwig, R. Shayduk and M. Bargheer: "Ultrafast lattice response of photoexcited thin films studied by X-ray diffraction", *Structural Dynamics* 1, 064501 (2014)

[50] T. Barron: "Vibrational effects in the thermal expansion of noncubic solids", *Journal of Applied Physics* 41, 5044 (1970)

[51] J. Chen, L. Hu, J. Deng and X. Xing: "Negative thermal expansion in functional materials: controllable thermal expansion by chemical modifications", *Chemical Society Reviews* 44, 3522 (2015)

[52] M. T. Dove and H. Fang: "Negative thermal expansion and associated anomalous physical properties: review of the lattice dynamics theoretical foundation", *Reports on Progress in Physics* 79, 066503 (2016)

[53] T. Fließbach: *Statistische Physik* (Spinger Spektrum, Berlin, 2018)

[54] T. Barron: "Grüneisen parameters for the equation of state of solids", *Annals of Physics* 1, 77 (1957)

[55] P. Sparks and C. Swenson: "Thermal expansions from 2 to 40K of Ge, Si, and four III-V compounds", *Physical Review* 163, 779 (1967)

[56] J. Collins, G. White, J. Birch and T. Smith: "Thermal expansion of ZnTe and HgTe and heat capacity of HgTe at low temperatures", *Journal of Physics C: Solid State Physics* 13, 1649 (1980)

[57] R. Grosse, P. Krause, M. Meissner and A. Tausend: "The coefficients of thermal expansion and the Gruneisen functions of trigonal and amorphous selenium in the temperature range between 10K and 300K", *Journal of Physics C: Solid State Physics* 11, 45 (1978)

[58] J.-U. Arnold and P. Grosse: "The Temperature Dependence of the Atom Coordinates in the Tellurium Lattice", *physica status solidi (b)* 28, K93 (1968)

[59] T. Mary, J. Evans, T. Vogt and A. Sleight: "Negative thermal expansion from 0.3 to 1050 Kelvin in ZrW_2O_8", *Science* 272, 90 (1996)

[60] R. Munn: "Role of the elastic constants in negative thermal expansion of axial solids", *Journal of Physics C: Solid State Physics* 5, 535 (1972)

[61] R. Munn: "The thermal expansion of axial metals", *Advances in Physics* 18, 515 (1969)

[62] X. Xing, J. Deng, J. Chen and G. Liu: "Novel thermal expansion of lead titanate", *Rare Metals* 22, 1 (2003)

[63] H. F. Kay and P. Vousden: "XCV. Symmetry changes in barium titanate at low temperatures and their relation to its ferroelectric properties", *The London, Edinburgh, and Dublin Philosophical Magazine and Journal of Science* 40, 1019 (1949)

[64] G. White: "Thermal expansion of Ca, Sr and Ba at low temperatures", *Journal of Physics F: Metal Physics* 2, 865 (1972)

[65] F. Nix and D. MacNair: "The thermal expansion of pure metals. II: molybdenum, palladium, silver, tantalum, tungsten, platinum, and lead", *Physical Review* 61, 74 (1942)

[66] W. Gauster: "Low-temperature Grüneisen parameters for silicon and aluminum", *Physical Review B* 4, 1288 (1971)

[67] P. Sharma and N. Singh: "Grüneisen Parameters of Cubic Metals", *Physical Review B* 1, 4635 (1970)

[68] G. White and J. Collins: "Thermal expansion of copper, silver, and gold at low temperatures", *Journal of Low Temperature Physics* 7, 43 (1972)

[69] G. White and O. Anderson: "Grüneisen parameter of magnesium oxide", *Journal of Applied Physics* 37, 430 (1966)

[70] J. Vetelino, S. Mitra and K. Namjoshi: "Lattice Dynamics, Mode Grüneisen Parameters, and Coefficient of Thermal Expansion of CsCl, CsBr, and CsI", *Physical Review B* 2, 2167 (1970)

[71] R. Roberts, G. White and E. Fawcett: "Thermal expansion of Cr and Cr-V alloys", *Physica B+ C* 119, 63 (1983)

[72] G. White: "Phase transitions and the thermal expansion of holmium", *Journal of Physics: Condensed Matter* 1, 6987 (1989)

[73] J. Varley: "The thermal expansion of pure metals and the possibility of negative coefficients of volume expansion", *Proceedings of the Royal Society of London. Series A. Mathematical and Physical Sciences* 237, 413 (1956)

[74] G. White: "Thermal expansion at low temperatures V. Dilute alloys of manganese in copper", *Journal of Physics and Chemistry of Solids* 23, 169 (1962)

[75] R. S. Krishnan, R. Srinivasan and S. Devanarayanan: *Thermal expansion of crystals: international series in the science of the solid state* (Elsevier, 2013)

[76] J. Fabian and P. B. Allen: "Thermal expansion and Grüneisen parameters of amorphous silicon: A realistic model calculation", *Physical review letters* 79, 1885 (1997)

[77] E. Cowley and R. A. Cowley: "Anharmonic interactions in alkali halides. I", *Proceedings of the Royal Society of London. Series A. Mathematical and Physical Sciences* 287, 259 (1965)

[78] G. Dolling and R. Cowley: "The thermodynamic and optical properties of germanium, silicon, diamond and gallium arsenide", *Proceedings of the Physical Society* 88, 463 (1966)

[79] G. White: "The thermal expansion of alkali halides at low temperatures", *Proceedings of the Royal Society of London. Series A. Mathematical and Physical Sciences* 286, 204 (1965)

[80] R. K. Kirby: "Thermal expansion of rutile from 100 to 700K", *Journal of Research of the National Bureau of Standards. Section A, Physics and Chemistry* 71, 363 (1967)

[81] X. Wang, J. Li and J. Cao: "Coherent phonon generation in laser-heated gold nanofilm", *The Journal of Chemical Physics* 152, 124704 (2020)

[82] J. Wang and C. Guo: "Non-equilibrium electronic Grüneisen parameter", *Applied Physics A* 111, 273 (2013)

[83] H. Park, X. Wang, S. Nie, R. Clinite and J. Cao: "Mechanism of coherent acoustic phonon generation under nonequilibrium conditions", *Physical Review B* 72, 100301 (2005)

[84] P.-T. Tai, P. Yu and J. Tang: "Laser-Fluence Dependence of Acoustic Phonon Excitation in Metallic Thin Films and Determination of the Gruneisen Parameter", *The Journal of Physical Chemistry C* 113, 15014 (2009)

[85] R. McCammon and G. White: "Thermal expansion at low temperatures of hexagonal metals: Mg, Zn and Cd", *The Philosophical Magazine: A Journal of Theoretical Experimental and Applied Physics* 11, 1125 (1965)

[86] M. Cardona and Y. Y. Peter: *Fundamentals of semiconductors* (Springer, 2005)

[87] G. White, T. Smith and R. Carr: "Thermal expansion of Cr, Mo and W at low temperatures", *Cryogenics* 18, 301 (1978)

[88] F. Nix and D. MacNair: "The thermal expansion of pure metals: copper, gold, aluminum, nickel, and iron", *Physical Review* 60, 597 (1941)

[89] A. Holden, V. Heine and J. Samson: "Magnetic contributions to thermal expansion of transition metals: implications for local moments above T_C", *Journal of Physics F: Metal Physics* 14, 1005 (1984)

[90] A. Kaiser and E. Haines: "Magnetovolume in chromium: collapse of moments above the Neel temperature", *Journal of Physics F: Metal Physics* 15, 1765 (1985)

[91] A. F. Guillermet: "Critical evaluation of the thermodynamic properties of cobalt", *International Journal of Thermophysics* 8, 481 (1987)

[92] B. Argyle and N. Miyata: "Magnetoelastic Behavior of Europium Oxide. II. Magnetostriction and the λ Anomaly", *Physical Review* 171, 555 (1968)

[93] M. Matsui, K. Adachi and S. Chikazumi: "Magnetic and thermal anomalies of Invar alloys", *Journal of Applied Physics* 51, 6319 (1980)

[94] P. Álvarez-Alonso et al.: "Magnetovolume and magnetocaloric effects in Er_2Fe_17", *Physical Review B* 86, 184411 (2012)

[95] M. Ibarra and P. Algarabel: "Giant volume magnetostriction in the FeRh alloy", *Physical Review B* 50, 4196 (1994)

[96] J. M. Coey: *Magnetism and magnetic materials* (Cambridge university press, 2010)

[97] E. Pytte: "Spin-phonon interactions in a Heisenberg ferromagnet", *Annals of Physics* 32, 377 (1965)

[98] A. Schult: "Effect of pressure on the Curie temperature of titanomagnetites $[(1-x)\cdot Fe_3O_4 - x \cdot TiFe_2O_4]$", *Earth and Planetary Science Letters* 10, 81 (1970)

[99] T. Henighan et al.: "Generation mechanism of terahertz coherent acoustic phonons in Fe", *Physical Review B* 93, 220301 (2016)

[100] R. Li, H. Elsayed-Ali, J. Chen, D. Dhankhar, A. Krishnamoorthi and P. M. Rentzepis: "Ultrafast time-resolved structural changes of thin-film ferromagnetic metal heated with femtosecond optical pulses", *The Journal of Chemical Physics* 151, 124702 (2019)

[101] A. Lindenberg et al.: "Time-resolved x-ray diffraction from coherent phonons during a laser-induced phase transition", *Physical review letters* 84, 111 (2000)

[102] J. Wang and C. Guo: "Effect of electron heating on femtosecond laser-induced coherent acoustic phonons in noble metals", *Physical Review B* 75, 184304 (2007)

[103] S. Anisimov, B. Kapeliovich, T. Perelman et al.: "Electron emission from metal surfaces exposed to ultrashort laser pulses", *Zh. Eksp. Teor. Fiz* 66, 375 (1974)

[104] X. Wang, S. Nie, J. Li, R. Clinite, J. E. Clark and J. Cao: "Temperature dependence of electron-phonon thermalization and its correlation to ultrafast magnetism", *Physical Review B* 81, 220301 (2010)

[105] E. Beaurepaire, J.-C. Merle, A. Daunois and J.-Y. Bigot: "Ultrafast spin dynamics in ferromagnetic nickel", *Physical review letters* 76, 4250 (1996)

[106] B. Koopmans, G. Malinowski, F. Dalla Longa, D. Steiauf, M. Fähnle, T. Roth, M. Cinchetti and M. Aeschlimann: "Explaining the paradoxical diversity of ultrafast laser-induced demagnetization", *Nature materials* 9, 259 (2010)

[107] J. Kimling, J. Kimling, R. Wilson, B. Hebler, M. Albrecht and D. G. Cahill: "Ultrafast demagnetization of FePt: Cu thin films and the role of magnetic heat capacity", *Physical Review B* 90, 224408 (2014)

[108] Z. Lin, L. V. Zhigilei and V. Celli: "Electron-phonon coupling and electron heat capacity of metals under conditions of strong electron-phonon nonequilibrium", *Physical Review B* 77, 075133 (2008)

[109] B. Mueller and B. Rethfeld: "Relaxation dynamics in laser-excited metals under nonequilibrium conditions", *Physical Review B* 87, 035139 (2013)

[110] M. Sentef, A. F. Kemper, B. Moritz, J. K. Freericks, Z.-X. Shen and T. P. Devereaux: "Examining electron-boson coupling using time-resolved spectroscopy", *Physical Review X* 3, 041033 (2013)

[111] L. Waldecker, R. Bertoni, R. Ernstorfer and J. Vorberger: "Electron-phonon coupling and energy flow in a simple metal beyond the two-temperature approximation", *Physical Review X* 6, 021003 (2016)

[112] P. Maldonado, K. Carva, M. Flammer and P. M. Oppeneer: "Theory of out-of-equilibrium ultrafast relaxation dynamics in metals", *Physical Review B* 96, 174439 (2017)

[113] U. Ritzmann, P. M. Oppeneer and P. Maldonado: "Theory of out-of-equilibrium electron and phonon dynamics in metals after ultrafast laser excitation", *arXiv preprint arXiv:1911.12414* (2019)

[114] S. T. Weber and B. Rethfeld: "Phonon-induced long-lasting nonequilibrium in the electron system of a laser-excited solid", *Physical Review B* 99, 174314 (2019)

[115] P. Maldonado et al.: "Tracking the ultrafast nonequilibrium energy flow between electronic and lattice degrees of freedom in crystalline nickel", *Physical Review B* 101, 100302 (2020)

[116] W. Fann, R. Storz, H. Tom and J. Bokor: "Electron thermalization in gold", *Physical Review B* 46, 13592 (1992)

[117] A. Krishnamoorthy et al.: "Optical control of non-equilibrium phonon dynamics", *Nano letters* 19, 4981 (2019)

[118] Q. Gan, R. Rao, C. Eom, J. Garrett and M. Lee: "Direct measurement of strain effects on magnetic and electrical properties of epitaxial $SrRuO_3$ thin films", *Applied Physics Letters* 72, 978 (1998)

[119] R. Boehler, I. C. Getting and G. C. Kennedy: "Grüneisen parameter of NaCl at high compressions", *Journal of Physics and Chemistry of Solids* 38, 233 (1977)

[120] M. Kumari and N. Dass: "On the pressure dependence of Grüneisen parameter in solids", *physica status solidi (b)* 133, 101 (1986)

[121] Z.-H. Fang: "Pressure dependence of Grüneisen parameter in solids", *physica status solidi (b)* 197, 39 (1996)

[122] J. Ramakrishnan and G. C. Kennedy: "Anomalous behavior of the Grüneisen parameter in cerium near the high-pressure phase transition", *Journal of Applied Physics* 51, 2586 (1980)

[123] M. Herzog, D. Schick, P. Gaal, R. Shayduk, C. v. K. Schmising and M. Bargheer: "Analysis of ultrafast X-ray diffraction data in a linear-chain model of the lattice dynamics", *Applied Physics A* 106, 489 (2012)

[124] D. Schick, A. Bojahr, M. Herzog, R. Shayduk, C. von Korff Schmising and M. Bargheer: "udkm1Dsim—A simulation toolkit for 1D ultrafast dynamics in condensed matter", *Computer Physics Communications* 185, 651 (2014)

[125] J. Als-Nielsen and D. McMorrow: *Elements of modern X-ray physics* (John Wiley & Sons, 2001)

[126] M. Bargheer, N. Zhavoronkov, M. Woerner and T. Elsaesser: "Recent progress in ultrafast X-ray diffraction", *Chemphyschem: a European journal of chemical physics and physical chemistry* 7, 783 (2006)

[127] K. Sokolowski-Tinten et al.: "Femtosecond X-ray measurement of coherent lattice vibrations near the Lindemann stability limit", *Nature* 422, 287 (2003)

[128] D. Schick, R. Shayduk, A. Bojahr, M. Herzog, C. v. Korff Schmising, P. Gaal and M. Bargheer: "Ultrafast reciprocal-space mapping with a convergent beam", *Journal of Applied Crystallography* 46, 1372 (2013)

[129] U. Pietsch, V. Holy and T. Baumbach: *High-resolution X-ray scattering: from thin films to lateral nanostructures* (Springer Science & Business Media, 2004)

[130] S. P. Zeuschner, M. Mattern, J.-E. Pudell, A. von Reppert, M. Rössle, W. Leitenberger, M. Herzog and M. Bargheer: "Time-efficient femtosecond X-ray Diffraction via reciprocal space slicing", *XXX* Unpublished (2020)

[131] F. Zamponi et al.: "Femtosecond hard X-ray plasma sources with a kilohertz repetition rate", *Applied Physics A* 96, 51 (2009)

[132] D. Schick, A. Bojahr, M. Herzog, C. v. K. Schmising, R. Shayduk, W. Leitenberger, P. Gaal and M. Bargheer: "Normalization schemes for ultrafast x-ray diffraction using a table-top laser-driven plasma source", *Review of Scientific Instruments* 83, 025104 (2012)

[133] A. von Reppert: "Ultrafast magnetostriction in dysprosium studied by femtosecond X-Ray diffraction" Msc thesis, University of Potsdam (2015)

[134] C. von Korff Schmising, M. Bargheer, M. Kiel, N. Zhavoronkov, M. Woerner, T. Elsaesser, I. Vrejoiu, D. Hesse and M. Alexe: "Accurate time delay determination for femtosecond X-ray diffraction experiments", *Applied Physics B* 88, 1 (2007)

[135] A. Bojahr, D. Schick, L. Maerten, M. Herzog, I. Vrejoiu, C. von Korff Schmising, C. Milne, S. L. Johnson and M. Bargheer: "Comparing the oscillation phase in optical pump-probe spectra to ultrafast x-ray diffraction in the metal-dielectric $SrRuO_3/SrTiO_3$ superlattice", *Physical Review B* 85, 224302 (2012)

[136] J. Pudell: "Ultraschnelle Magnetostriktion von antiferromagnetischem Holmium" Msc thesis, University of Potsdam (2015)

[137] J. Weisshaupt, V. Juvé, M. Holtz, S. Ku, M. Woerner, T. Elsaesser, S. Ališauskas, A. Pugžlys and A. Baltuška: "High-brightness table-top hard X-ray source driven by sub-100-femtosecond mid-infrared pulses", *Nature Photonics* 8, 927 (2014)

[138] J. Weisshaupt, V. Juvé, M. Holtz, M. Woerner and T. Elsaesser: "Theoretical analysis of hard x-ray generation by nonperturbative interaction of ultrashort light pulses with a metal", *Structural Dynamics* 2, 024102 (2015)

[139] M. Bargheer, N. Zhavoronkov, R. Bruch, H. Legall, H. Stiel, M. Wörner and T. Elsässer: "Comparison of focusing optics for femtosecond X-ray diffraction", *Applied Physics B* 80, 715 (2005)

[140] W. Tian et al.: "Epitaxial growth and magnetic properties of the first five members of the layered $Sr_{n+1}Ru_nO_{3n+1}$ oxide series", *Applied physics letters* 90, 022507 (2007)

[141] G. Laskin, H. Wang, H. Boschker, W. Braun, V. Srot, P. A. van Aken and J. Mannhart: "Magnetic Properties of Epitaxially Grown $SrRuO_3$ Nanodots", *Nano Letters* 19, 1131 (2019)

[142] F. W. Lytle: "X-ray diffractometry of low-temperature phase transformations in strontium titanate", *Journal of Applied Physics* 35, 2212 (1964)

[143] S. Yamanaka, T. Maekawa, H. Muta, T. Matsuda, S.-i. Kobayashi and K. Kurosaki: "Thermophysical properties of $SrHfO_3$ and $SrRuO_3$", *Journal of Solid State Chemistry* 177, 3484 (2004)

[144] B. Dabrowski, M. Avdeev, O. Chmaissem, S. Kolesnik, P. Klamut, M. Maxwell and J. Jorgensen: "Freezing of octahedral tilts below the Curie temperature in $SrRu_{1-v}O_3$ perovskites", *Physical Review B* 71, 104411 (2005)

[145] S. Bushmeleva, V. Y. Pomjakushin, E. Pomjakushina, D. Sheptyakov and A. Balagurov: "Evidence for the band ferromagnetism in SrRuO3 from neutron diffraction", *Journal of magnetism and magnetic materials* 305, 491 (2006)

[146] G. Koster, L. Klein, W. Siemons, G. Rijnders, J. S. Dodge, C.-B. Eom, D. H. Blank and M. R. Beasley: "Structure, physical properties, and applications of $SrRuO_3$ thin films", *Reviews of Modern Physics* 84, 253 (2012)

[147] Q. Gan, R. Rao and C. Eom: "Control of the growth and domain structure of epitaxial SrRuO 3 thin films by vicinal (001) $SrTiO_3$ substrates", *Applied physics letters* 70, 1962 (1997)

[148] C.-B. Eom, R. Cava, R. Fleming, J. M. Phillips, J. Marshall, J. Hsu, J. Krajewski, W. Peck et al.: "Single-crystal epitaxial thin films of the isotropic metallic oxides $Sr_{1-x}Ca_xRuO_3$ $(0 < x < 1)$", *Science* 258, 1766 (1992)

[149] J.-P. Maria, H. McKinstry and S. Trolier-McKinstry: "Origin of preferential orthorhombic twinning in $SrRuO_3$ epitaxial thin films", *Applied Physics Letters* 76, 3382 (2000)

[150] L. Maerten, A. Bojahr, M. Gohlke, M. Rössle and M. Bargheer: "Coupling of GHz Phonons to Ferroelastic Domain Walls in $SrTiO_3$", *Physical review letters* 114, 047401 (2015)

[151] G. Cao, S. McCall, M. Shepard, J. Crow and R. Guertin: "Thermal, magnetic, and transport properties of single-crystal $Sr_{1-x}Ca_xRuO_3$ $(0 < x < 1)$", *Physical Review B* 56, 321 (1997)

[152] I. Mazin and D. J. Singh: "Electronic structure and magnetism in Ru-based perovskites", *Physical Review B* 56, 2556 (1997)

[153] D. J. Singh: "Electronic and magnetic properties of the 4d itinerant ferromagnet $SrRuO_3$", *Journal of applied physics* 79, 4818 (1996)

[154] K. Fujioka et al.: "Electronic structure of $SrRuO_3$", *Physical Review B* 56, 6380 (1997)

[155] L. Klein, J. Dodge, C. Ahn, J. Reiner, L. Mieville, T. Geballe, M. Beasley and A. Kapitulnik: "Transport and magnetization in the badly metallic itinerant ferromagnet", *Journal of Physics: Condensed Matter* 8, 10111 (1996)

[156] Q. Gan, R. Rao, C. Eom, L. Wu and F. Tsui: "Lattice distortion and uniaxial magnetic anisotropy in single domain epitaxial (110) films of $SrRuO_3$", *Journal of applied physics* 85, 5297 (1999)

[157] M. Langner, C. Kantner, Y. Chu, L. Martin, P. Yu, J. Seidel, R. Ramesh and J. Orenstein: "Observation of ferromagnetic resonance in SrRuO 3 by the time-resolved magneto-optical Kerr effect", *Physical review letters* 102, 177601 (2009)

[158] T. Ogasawara, K. Ohgushi, Y. Tomioka, K. Takahashi, H. Okamoto, M. Kawasaki and Y. Tokura: "General features of photoinduced spin dynamics in ferromagnetic and ferrimagnetic compounds", *Physical review letters* 94, 087202 (2005)

[159] P. Allen, H. Berger, O. Chauvet, L. Forro, T. Jarlborg, A. Junod, B. Revaz and G. Santi: "Transport properties, thermodynamic properties, and electronic structure of $SrRuO_3$", *Physical Review B* 53, 4393 (1996)

[160] E. H. P. Cordfunke, R. Van Der Laan and J. Van Miltenburg: "Thermophysical and thermochemical properties of BaO and SrO from 5 to 1000 K", *Journal of Physics and Chemistry of Solids* 55, 77 (1994)

[161] E. Cordfunke, R. Konings, E. Westrum Jr and R. Shaviv: "The thermophysical and thermochemical properties of RuO_2 from 0 to 1000 K", *Journal of Physics and Chemistry of Solids* 50, 429 (1989)

[162] F. Castelpoggi, L. Morelli, H. Salva, S. Cuffini, R. Carbonio and R. Sanchez: "Specific heat measurement of the magnetoresistant perovskite $SrRuO_3$", *Solid state communications* 101, 597 (1997)

[163] F. Bern, M. Ziese, A. Setzer, E. Pippel, D. Hesse and I. Vrejoiu: "Structural, magnetic and electrical properties of $SrRuO_3$ films and $SrRuO_3/SrTiO_3$ superlattices", *Journal of Physics: Condensed Matter* 25, 496003 (2013)

[164] P. Kostic, Y. Okada, N. Collins, Z. Schlesinger, J. Reiner, L. Klein, A. Kapitulnik, T. Geballe and M. Beasley: "Non-Fermi-liquid behavior of $SrRuO_3$: evidence from infrared conductivity", *Physical Review Letters* 81, 2498 (1998)

[165] M. Highland, B. Gundrum, Y. K. Koh, R. S. Averback, D. G. Cahill, V. Elarde, J. Coleman, D. Walko and E. Landahl: "Ballistic-phonon heat conduction at the nanoscale as revealed by time-resolved x-ray diffraction and time-domain thermoreflectance", *Physical Review B* 76, 075337 (2007)

[166] T. Moriya and K. Usami: "Magneto-volume effect and invar phenomena in ferromagnetic metals", *Solid State Communications* 34, 95 (1980)

[167] W. C. Koehler: "Magnetic properties of rare-earth metals and alloys", *Journal of Applied Physics* 36, 1078 (1965)

[168] M. A. Ruderman and C. Kittel: "Indirect exchange coupling of nuclear magnetic moments by conduction electrons", *Physical Review* 96, 99 (1954)

[169] T. Kasuya: "A theory of metallic ferro-and antiferromagnetism on Zener's model", *Progress of theoretical physics* 16, 45 (1956)

[170] K. Yosida: "Magnetic properties of Cu-Mn alloys", *Physical Review* 106, 893 (1957)

[171] D. Behrendt, S. Legvold and F. Spedding: "Magnetic properties of dysprosium single crystals", *Physical Review* 109, 1544 (1958)

[172] B. Coqblin: "Electronic Structure of Rare-Earth Metals and Alloys–the Magnetic Heavy Rare-Earths", *Academic Press Inc., New York and London. 1977, 656 p* (1977)

[173] A. J. Freeman and R. Watson: "Theoretical investigation of some magnetic and spectroscopic properties of rare-earth ions", *Physical Review* 127, 2058 (1962)

[174] W. Nolting and A. Ramakanth: *Quantum theory of magnetism* (Springer Science & Business Media, 2009)

[175] F. Tsui and C. Flynn: "Magnetic phase diagram of epitaxial dysprosium", *Physical review letters* 71, 1462 (1993)

[176] M. Salamon, S. Sinha, J. Rhyne, J. Cunningham, R. W. Erwin, J. Borchers and C. Flynn: "Long-range incommensurate magnetic order in a Dy-Y multilayer", *Physical review letters* 56, 259 (1986)

[177] S. Blundell: "Magnetism in condensed matter" (2003)

[178] A. S. Bulatov, V. F. Dolzenko and A. V. Kornietz: "Temperature dependences of thermal expansion and exchange magnetostriction of holmium and dysprosium single crystals", *Czechoslovak Journal of Physics* 46, 2119 (1996)

[179] A. Chernyshov, Y. Mudryk, V. Pecharsky and K. Gschneidner Jr: "Temperature and magnetic field-dependent x-ray powder diffraction study of dysprosium", *Physical Review B* 77, 094132 (2008)

[180] F. Spedding, J. Hanak and A. Daane: "High temperature allotropy and thermal expansion of the rare-earth metals", *Journal of the Less Common Metals* 3, 110 (1961)

[181] I. Hughes et al.: "Lanthanide contraction and magnetism in the heavy rare earth elements", *Nature* 446, 650 (2007)

[182] L. Benito, J. Arnaudas, M. Ciria, C. de La Fuente and A. del Moral: "The magnetostriction of Tb, Dy and Ho revisited", *Journal of Physics: Condensed Matter* 16, 7151 (2004)

[183] V. Pecharsky, K. Gschneidner Jr and D. Fort: "Superheating and other unusual observations regarding the first order phase transition in Dy", *Scripta materialia* 35, 843 (1996)

[184] W. M. Haynes: *CRC handbook of chemistry and physics* (CRC press, 2014)

[185] B. Gerstein, W. Taylor, W. Shickell and F. Spedding: "Heat Capacity of Lutetium from 6 to 300°K", *The Journal of Chemical Physics* 51, 2924 (1969)

[186] L. Jennings, R. Miller and F. Spedding: "Lattice heat capacity of the rare earths. Heat capacities of yttrium and lutetium from 15-350K", *The Journal of Chemical Physics* 33, 1849 (1960)

[187] S. Palmer: "Debye temperatures of holmium and dysprosium from single crystal elastic constant measurements", *Journal of Physics and Chemistry of Solids* 31, 143 (1970)

[188] S. Palmer and E. Lee: "The elastic constants of dysprosium and holmium", *Proceedings of the Royal Society of London. A. Mathematical and Physical Sciences* 327, 519 (1972)

[189] J. Smith and J. Gjevre: "Elastic Constants of Yttrium Single Crystals in the Temperature Range 4.2-400 K", *Journal of Applied Physics* 31, 645 (1960)

[190] K. J. Carroll: "Elastic Constants of Niobium from 4.2 to 300 K", *Journal of Applied Physics* 36, 3689 (1965)

[191] J. Wachtman Jr, W. Tefft, D. Lam Jr and R. Stinchfield: "Elastic constants of synthetic single crystal corundum at room temperature", *Journal of Research of the National Bureau of Standards. Section A, Physics and Chemistry* 64, 213 (1960)

[192] R. Roberge et al.: "Lattice parameter of niobium between 4.2 and 300K", *Journal of the Less Common Metals* 40, 161 (1975)

[193] M. Lucht, M. Lerche, H.-C. Wille, Y. V. Shvyd'Ko, H. Rüter, E. Gerdau and P. Becker: "Precise measurement of the lattice parameters of α-Al2O3 in the temperature range 4.5-250K using the Mössbauer wavelength standard", *Journal of applied crystallography* 36, 1075 (2003)

[194] D. C. Ginnings and G. T. Furukawa: "Heat Capacity Standards for the Range 14 to 1200°K.", *Journal of the American Chemical Society* 75, 522 (1953)

[195] C. Y. Ho, R. W. Powell and P. E. Liley: "Thermal conductivity of the elements", *Journal of Physical and Chemical Reference Data* 1, 279 (1972)

[196] E. R. Dobrovinskaya, L. A. Lytvynov and V. Pishchik: *Sapphire: material, manufacturing, applications* (Springer Science & Business Media, 2009)

[197] N. Thielemann-Kühn, D. Schick, N. Pontius, C. Trabant, R. Mitzner, K. Holldack, H. Zabel, A. Föhlisch and C. Schüßler-Langeheine: "Ultrafast and energy-efficient quenching of spin order: antiferromagnetism beats ferromagnetism", *Physical Review Letters* 119, 197202 (2017)

[198] B. Frietsch et al.: "Disparate ultrafast dynamics of itinerant and localized magnetic moments in gadolinium metal", *Nature communications* 6, 1 (2015)

[199] L. Rettig et al.: "Itinerant and localized magnetization dynamics in antiferromagnetic Ho", *Physical review letters* 116, 257202 (2016)

[200] A. Eschenlohr, M. Sultan, A. Melnikov, N. Bergeard, J. Wieczorek, T. Kachel, C. Stamm and U. Bovensiepen: "Role of spin-lattice coupling in the ultrafast demagnetization of $\mathrm{Gd}_{1-x}\mathrm{Tb}_x$ alloys", *Physical Review B* 89, 214423 (2014)

[201] K. Bobowski, M. Gleich, N. Pontius, C. Schüßler-Langeheine, C. Trabant, M. Wietstruk, B. Frietsch and M. Weinelt: "Influence of the pump pulse wavelength on the ultrafast demagnetization of Gd (0001) thin films", *Journal of Physics: Condensed Matter* 29, 234003 (2017)

STATEMENT OF AUTHORSHIP

I hereby certify that this master thesis was written independently and without assistance from third parties. Other than the stated sources and aids were not used. Parts of the sources that have been used verbatim or in substance are identified as such. This master thesis has not been presented in the same or similar form to any audit authority and was not published.

Hiermit versichere ich, dass ich die vorliegende Masterarbeit selbstständig und ohne Hilfe Dritter verfasst habe. Andere als die angegebenen Quellen und Hilfsmittel wurden nicht verwendet. Die den benutzten Quellen wörtlich oder inhaltlich entnommenen Abschnitte sind als solche kenntlich gemacht. Diese Masterarbeit hat in gleicher oder ähnlicher Form noch keiner Prüfungsbehörde vorgelegen und wurde auch nicht veröffentlicht.

Potsdam, 5.11.2020 (Maximilian Mattern)